Evaluating the Functional Recovery Performance of Modern Residential Tall Reinforced Concrete Shear Wall Buildings in Metro Vancouver

by

Parsa Taghvaei

B.Sc., Sharif University of Technology, 2019

A THESIS SUBMITTED IN PARTIAL FULFILLMENT OF

THE REQUIREMENTS FOR THE DEGREE OF

MASTER OF APPLIED SCIENCE

in

THE FACULTY OF GRADUATE AND POSTDOCTORAL STUDIES

(Civil Engineering)

THE UNIVERSITY OF BRITISH COLUMBIA

(Vancouver)

March 2022

The following individuals certify that they have read, and recommend to the Faculty of Graduate and Postdoctoral Studies for acceptance, the thesis entitled:

Evaluating the Functional Recovery Performance of Modern Residential Tall Reinforced Concrete Shear Wall Buildings in Metro Vancouver

submitted by Parsa Taghvaei in partial fulfillment of the requirements for

the degree of Master of Applied Science

in Civil Engineering

Examining Committee:

Carlos Molina Hutt, Department of Civil Engineering, The University of British Columbia
Supervisor

Jose Centeno, Glotman Simpson Consulting Engineers
Additional Examiner

Abstract

Modern tall residential Reinforced Concrete Shear Wall (RCSW) buildings in Metro Vancouver are exposed to a considerable hazard due to the proximity of various seismic sources, such as the Cascadia Subduction Zone (CSZ), and the presence of Georgia sedimentary basin, which can amplify the intensity of ground motions at medium-to-long periods. Current building codes do not account for basin amplification effects, they intend to ensure life-safety in extreme earthquakes and do not explicitly minimize damage to building components that preserve building functionality. This study aims to provide insights into the expected loss and functional recovery time of tall RCSW buildings in Metro Vancouver under a variety of earthquake intensities. To this end, nonlinear models of archetype RCSW buildings are developed for eight different locations in Metro Vancouver. These models are subjected to ground motions representative of a range of hazard levels as per Canada's 2015 National Seismic Hazard Model, which neglects basin effects, as well as a suite of simulated ground motions of M9 CSZ earthquake scenarios, which explicitly accounts for basin amplification. The structural responses are employed to conduct a loss assessment using a well-established methodology and a downtime assessment using a recently developed framework. Loss estimates show that the mean loss ratios under the M9 motions vary between 1.4% and 32% across Metro Vancouver and range from 0.7% to 14% for the range of hazard levels considered in this study. Downtime estimates show that the functional recovery time of buildings subjected to the M9 motions can range from 175 to 543 days and vary between 164 to 491 days for the range of hazard levels considered. The archetype buildings do not meet the robustness criteria of ensuring that there is a probability of less than 10% of not achieving sheltering capacity under the functional level earthquake (~ 475 year return period). Similarly, the

archetype buildings do not meet the rapidity criteria of observing less than a 10% probability of not achieving functional recovery within four months after the functional level earthquake. Downtime deaggregation shows that the main contributor to functional recovery time is attributed to slab-column connection damage.

Lay Summary

This thesis provides insights into the time it will take modern residential tall Reinforced Concrete Shear Wall buildings in Metro Vancouver to achieve functional recovery when subjected to different earthquake ground motion shaking intensities. To this end, advanced analyses are performed on robust analytical models of such buildings under different earthquake types and intensities. Results of these analyses are used to estimate the earthquake-induced economic loss attributed to seismic damage throughout the building. Also, the time required for the buildings to regain functionality after being subjected to an earthquake is estimated. These predicted building downtimes are used to evaluate the building performance against different resilience-based performance metrics. In addition, important factors which contribute to economic loss and functional recovery time of the buildings are identified.

Preface

This thesis is the original, independent work of Parsa Taghvaei. The author was responsible for the literature review, model development, computational analysis, data processing, and presentation of results. The thesis has been drafted and revised by the author based on review comments by Dr. Carlos Molina Hutt and Dr. Jose Centeno.

Table of Contents

Abstract .... **iii**

Lay Summary .... **v**

Preface .... **vi**

Table of Contents .... **vii**

List of Tables .... **xi**

List of Figures .... **xii**

Acknowledgements .... **xx**

Dedication .... **xxii**

Chapter 1: Introduction **1**

1.1 Background, Aims and Objectives 1

1.2 Methodology 7

1.3 Thesis Structure 9

Chapter 2: Literature Review **12**

2.1 Reinforced Concrete Shear Wall Buildings 12

2.2 Archetype Description 15

2.3 Deep Sedimentary Basin Effects 20

2.4 Simulated M9 CSZ Earthquakes and Georgia Sedimentary Basin 22

2.5 Nonlinear Modeling of Reinforced Concrete Shear Wall Buildings 27

2.6 Damage and Loss Assessment 34

2.6.1 Performance-based Earthquake Engineering 35

2.6.1.1 Assembling Building Performance Model 36

2.6.1.2 Define Earthquake Hazards 37

2.6.1.3 Analyze Building Response 38

2.6.1.4 Develop Collapse Fragility 38

2.6.1.5 Calculate Performance 38

2.6.2 Loss Assessment of Tall RCSW Buildings 40

2.7 Downtime Assessment 42

2.7.1 Background on Downtime Assessment 42

2.7.2 Downtime Assessment Framework 46

2.7.2.1 Recovery States and Post-Earthquake Usability 47

2.7.2.2 Impeding Factor Delays 49

2.7.2.3 Building Repair Time 51

2.7.2.4 Robustness and Rapidity 53

Chapter 3: Structural Analysis Model Development and Validation 56

3.1 OpenSeesPy 56

3.2 Building Model 57

3.2.1 Reinforced Concrete Shear Wall Model 60

3.2.1.1 Constitutive Material Models 64

3.2.1.1.1 Concrete Model 64

3.2.1.1.2 Steel Model 66

3.2.1.2 Material Regularization 68

3.2.1.3 Shear Response 69

3.2.1.4 Nonlinear Model Validation 70

3.2.2 P-Delta Effects 72

3.2.3 Basement Model ... 73

3.2.4 Damping Assumptions ... 75

3.2.5 Analysis Settings ... 76

3.2.6 Solving Convergence Issues ... 77

Chapter 4: Seismic Hazard and Ground Motion Selection ... 79

4.1 Scenario and Intensity-Based Seismic Performance Assessments ... 79

4.2 NBC 2015 Ground Motions ... 80

4.3 Simulated M9 CSZ Earthquake Ground Motions ... 83

Chapter 5: Nonlinear Simulation of Structural Response ... 85

5.1 Story Drift Ratio ... 86

5.1.1 Transient Drift Ratio ... 86

5.1.2 Residual Drift Ratio ... 89

5.1.3 Racking and Damageable Wall Drifts ... 92

5.1.3.1 Racking Drift Ratio ... 94

5.1.3.2 Damageable Wall Drift Ratio ... 98

5.2 Peak Floor Acceleration ... 100

5.3 Wall Strains ... 103

5.3.1 Concrete Compression ... 103

5.3.2 Steel Tension ... 106

5.4 Wall Shear Force ... 109

5.5 Summary of Structural Responses ... 112

Chapter 6: Damage and Loss Assessment ... 114

6.1 Building Performance Model ... 114

6.2 Loss Assessment Results 122

Chapter 7: Downtime Assessment 132

7.1 Downtime to Different Recovery States 133

7.2 Downtime Trajectory 136

7.3 Robustness and Rapidity 145

7.4 Downtime Deaggregation 148

7.5 Summary and Recommendations 155

Chapter 8: Conclusions 157

8.1 Summary of Findings 157

8.1.1 Summary of Nonlinear Analysis Results 157

8.1.2 Summary of Loss Assessment Results 158

8.1.3 Summary of Downtime Assessment Results 160

8.2 Future Studies 162

References 165

List of Tables

Table 2.1. Dynamic properties of the archetype RCSW (Eksir Monfared et al., 2021). 17

Table 2.2. Summary design of the coupling beams (Eksir Monfared et al., 2021)...................... 18

Table 2.3. Summary design of the walls (Eksir Monfared et al., 2021). 19

Table 2.4. Locations of study within Metro Vancouver including coordinates, Vs30, Z2.5, and SA(T=3s) corresponding to the NBC 2015 2475-year return period spectrum and the average of the simulated ground motions of M9 CSZ earthquakes (Eksir Monfared et al., 2021). 24

Table 2.5. Recovery states, building condition, and associated repair class for downtime estimation (Molina Hutt et al., 2022). 48

Table 3.1. Modal analysis results. 58

Table 4.1. Ground motion records database. 80

Table 4.2. Scenario-specific period range. 81

Table 5.1. Summary of peak of the means of structural responses for all locations and hazard levels. 112

Table 6.1. Components considered in the building performance model of the RCSW building archetype. 116

Table 6.2. Collapse probabilities at different sites in the scenario-based assessment. 119

Table 7.1. Median downtime realization to different recovery states (shelter-in-place, reoccupancy, and functional recovery) under the scenario and intensity-based assessments. ... 136

List of Figures

Figure 1.1. Population density of British Columbia in 2017 (Environmental Reporting BC, 2018): (a) Population of different Regional Districts across British Columbia; (b) Population density map (population per km2) of British Columbia.. 3

Figure 1.2. Research Methodology. 7

Figure 2.1. Examples of reinforced concrete shear wall cross sections (Moehle et al., 2011). ... 13

Figure 2.2. Schematic of a core reinforced concrete shear wall system (Moehle et al., 2011). .. 14

Figure 2.3. Target yield mechanism of coupled reinforced concrete shear wall systems (Moehle et al., 2011). 14

Figure 2.4. Archetype RCSW building: (a) isometric view; (b) superstructure plan view (Eksir Monfared et al., 2021).. 16

Figure 2.5. Reinforcement layout of the walls (Eksir Monfared et al., 2021). 19

Figure 2.6. Variation of $Z_{2.5}$ across southwest British Columbia, selected locations of study throughout Metro Vancouver as well as geographical distribution of reinforced concrete shear wall (RCSW) buildings (> 8 stories) constructed since 2000 (Eksir Monfared et al., 2021). 23

Figure 2.7. Variation of the simulated ground motions of M9 CSZ earthquakes response spectra in Vancouver against the design response spectrum (i.e. 2475-year hazard) (adopted from Eksir Monfared et al., 2021).. 25

Figure 2.8. Variation of the simulated ground motions of M9 CSZ earthquakes response spectra against the design response spectra (i.e. 2475-year hazard) in different locations (adopted from Eksir Monfared et al., 2021). 26

Figure 2.9. Different approaches to simulate the nonlinear response of RCSW: (a) zero-length hinge model; (b) fiber-type beam column element; (c) beam-column element with flexure-shear interaction; (d) fiber-shell element; (e) layered-shell element; (f) 3D continuum elements (NIST, 2017b). Note that BE means boundary element. 28

Figure 2.10. Modeling of RCSWs using fiber-type beam column element model: (a) sample shear wall; (b) Fiber-type beam column element model. 31

Figure 2.11. Regularized material response (Pugh, 2012). 34

Figure 2.12. First generation performance-based earthquake engineering methodology (after Holmes)(Moehle & Deierlein, 2004). 35

Figure 2.13. Flowchart of FEMA P-58 performance assessment methodology (FEMA, 2018). 36

Figure 2.14. Flowchart for performance calculation in each realization (FEMA, 2018). 39

Figure 2.15. Sequencing of impeding factor delays for downtime estimation (Molina Hutt et al., 2022). 49

Figure 3.1. Schematic of the (a) building plan and tributary area of the walls and columns; (b) OpenSeesPy analytical model. 59

Figure 3.2. Variation in the axial force in different integration points along the height of the shear wall with different number of elements. 61

Figure 3.3. Possible configurations of the fiber-discretized wall sections of each cantilevered pier in the building model: (a) C-shaped configuration; (b) I-shaped configuration. The steel bars are not shown for clarity and the red zones are the boundary regions. 62

Figure 3.4. Sensitivity of moment-curvature response of the wall to the number of fibers. Default number of fibers refers to the case where 12 and 30 divisions are considered in each flange and web of the wall, respectively. 63

Figure 3.5. Stress-strain relation of the Concrete02 material in OpenSees (Mohd Yassin, 1994). 65

Figure 3.6. Steel material model stress-strain relation (Menegotto & Pinto, 1973). 68

Figure 3.7. Sectional analysis results of each cantilevered pier at the grade level of the building: (a) Moment-curvature response; (b) extreme tension steel fiber. 69

Figure 3.8. Section aggregator command in OpenSees (OpenSeesWiki, 2016).......................... 70

Figure 3.9. Shear wall calibration results... 71

Figure 3.10. Equilibrium force for Yura derivation (Geschwindner, 2002). 72

Figure 3.11. Story shear for different values of (a) basement diaphragm stiffness; and (b) basement wall stiffness under a simulated ground motion of M9 CSZ earthquake in Delta. Note that the default basement stiffness is used in this study for nonlinear time-history analysis. 74

Figure 3.12. Percent of critical damping at different periods for mass, stiffness, and Rayleigh proportional damping.. 75

Figure 4.1. 10% in 50-year target spectra, individual ground motions spectra, and average spectra for seismic sources: (a) Crustal, (b) Intraslab, (c) Interface. 82

Figure 4.2. Design target spectrum, individual ground motions spectra, and average spectra for M9 motions in the locations of interest across Metro Vancouver area: (a) Delta; (b) Richmond; (c) Burnaby; (d) Surrey; (e) New Westminster; (f) Vancouver; (g) North Vancouver; (h) West Vancouver. 84

Figure 5.1. Comparison of the transient drift ratios associated with the scenario-based assessments and average response of each hazard level considered in the intensity-based assessments. Sites flagged with an * indicate locations where some time-history analyses resulted in collapse. Refer

to Table 6.2 for exact collapse probabilities. Results shown are the average of non-collapse time-history analyses. 87

Figure 5.2. Transient drift ratios associated with each seismic source for different hazard levels in the intensity-based assessments: (a) 2475-year motions; (b) 975-year motions; (c) 475-year motions; (d) 100-year motions. 88

Figure 5.3. Comparison of the residual drift ratios associated with the scenario-based assessments and average response of each hazard level considered in the intensity-based assessments. Sites flagged with an * indicate locations where some time-history analyses resulted in collapse. Refer to Table 6.2 for exact collapse probabilities. Results shown are the average of non-collapse time-history analyses. 90

Figure 5.4. Residual drift ratios associated with each seismic source for different hazard levels in the intensity-based assessments: (a) 2475-year motions; (b) 975-year motions; (c) 475-year motions; (d) 100-year motions. 91

Figure 5.5. Idealized schematic of the building deformation to illustrate damageable drift calculations (Molina Hutt et al., 2022). 93

Figure 5.6. Comparison of the racking drift ratios associated with the scenario-based assessments and average response of each hazard level considered in the intensity-based assessments. Sites flagged with an * indicate locations where some time-history analyses resulted in collapse. Refer to Table 6.2 for exact collapse probabilities. Results shown are the average of non-collapse time-history analyses. 96

Figure 5.7. Racking drift ratios associated with each seismic source for different hazard levels in the intensity-based assessments: (a) 2475-year motions; (b) 975-year motions; (c) 475-year motions; (d) 100-year motions. 97

Figure 5.8. Comparison of the damageable wall drift ratios associated with the scenario-based assessments and average response of each hazard level considered in the intensity-based assessments. Sites flagged with an * indicate locations where some time-history analyses resulted in collapse. Refer to Table 6.2 for exact collapse probabilities. Results shown are the average of non-collapse time-history analyses. 98

Figure 5.9. Damageable wall drift ratios associated with each seismic source for different hazard levels in the intensity-based assessments: (a) 2475-year motions; (b) 975-year motions; (c) 475-year motions; (d) 100-year motions. 99

Figure 5.10. Comparison of the peak floor accelerations associated with the scenario-based assessments and average response of each hazard level considered in the intensity-based assessments. Sites flagged with an * indicate locations where some time-history analyses resulted in collapse. Refer to Table 6.2 for exact collapse probabilities. Results shown are the average of non-collapse time-history analyses. 101

Figure 5.11. Peak floor accelerations associated with each seismic source for different hazard levels in the intensity-based assessments: (a) 2475-year motions; (b) 975-year motions; (c) 475-year motions; (d) 100-year motions. 102

Figure 5.12. Comparison of the peak concrete compressive strain associated with the scenario-based assessments and average response of each hazard level considered in the intensity-based assessments. Sites flagged with an * indicate locations where some time-history analyses resulted in collapse. Refer to Table 6.2 for exact collapse probabilities. Results shown are the average of non-collapse time-history analyses. 104

Figure 5.13. Peak concrete compressive strain associated with each seismic source for different hazard levels in the intensity-based assessments: (a) 2475-year motions; (b) 975-year motions; (c) 475-year motions; (d) 100-year motions. 105

Figure 5.14. Comparison of the peak steel tensile strain associated with the scenario-based assessments and average response of each hazard level considered in the intensity-based assessments. Sites flagged with an * indicate locations where some time-history analyses resulted in collapse. Refer to Table 6.2 for exact collapse probabilities. Results shown are the average of non-collapse time-history analyses. 107

Figure 5.15. Peak steel tensile strain associated with each seismic source for different hazard levels in the intensity-based assessments: (a) 2475-year motions; (b) 975-year motions; (c) 475-year motions; (d) 100-year motions. 108

Figure 5.16. Comparison of RC pier shear demand associated with the scenario-based assessments and average response of each hazard level considered in the intensity-based assessments. Sites flagged with an * indicate locations where some time-history analyses resulted in collapse. Refer to Table 6.2 for exact collapse probabilities. Results shown are the average of non-collapse time-history analyses. 109

Figure 5.17. RC pier shear demand associated with each seismic source for different hazard levels in the intensity-based assessments: (a) 2475-year motions; (b) 975-year motions; (c) 475-year motions; (d) 100-year motions. 111

Figure 6.1. Comparison of the EDPs obtained from Monte Carlo simulation and time-history analysis for 2475-year motions: (a) transient drift ratio; (b) racking drift ratio; (c) damageable wall drift ratio; (d) peak floor acceleration. 120

Figure 6.2. Residual drift ratio histograms for 2475-year motions obtained from: (a) time-history analysis; (b) Monte Carlo simulation. 122

Figure 6.3. Mean loss ratio for the intensity- and scenario-based assessments. 123

Figure 6.4. Variation of loss ratio for intensity-based assessments with (a) 2475-year; (b) 975-year; (c) 475-year; (d) 100-year return periods and scenario-based assessments at (e) Delta; (f) Richmond; (g) Burnaby; (h) Surrey; (i) New Westminster; (j) Vancouver; (k) North Vancouver; (l) West Vancouver. 124

Figure 6.5. Percentage of collapse, irreparable, and repairable realizations for the intensity- and scenario-based assessments. 125

Figure 6.6. Loss deaggregation for the intensity- and scenario-based assessments. 126

Figure 6.7. Loss vulnerability function for the intensity- and scenario-based assessments. 127

Figure 6.8. Repairable loss deaggregation for the intensity- and scenario-based assessments. 129

Figure 7.1. Downtime to different recovery states for the median realization of the intensity- and scenario-based assessments. 133

Figure 7.2. Recovery trajectories for each repair path to functional recovery of the median realization of the scenario-based assessment in New Westminster. Numbers in round brackets, ( ), indicate the duration of the impeding factor. The letter in square brackets, [ ], indicate the repair paths affected by each impeding factor delay. 138

Figure 7.3. Recovery trajectories to (a) functional recovery; and (b) shelter-in-place recovery states for the median realization of the intensity- and scenario-based assessments. 140

Figure 7.4. Recovery trajectories to functional recovery state for all realizations of the intensity-based assessments with (a) 100-year; (b) 475-year; (c) 975-year; (d) 2475-year return periods and

scenario-based assessments in (e) Delta; (f) Richmond; (g) Burnaby; (h) Surrey; (i) New Westminster; (j) Vancouver; (k) North Vancouver; (l) West Vancouver.................................. 142

Figure 7.5. Variation of downtime to achieve the functional recovery state for the intensity-based assessments with (a) 2475-year; (b) 975-year; (c) 475-year; (d) 100-year hazard levels and the scenario-based assessments at (e) Delta; (f) Richmond; (g) Burnaby; (h) Surrey; (i) New Westminster; (j) Vancouver; (k) North Vancouver; (l) West Vancouver.................................. 144

Figure 7.6. Percentage of realizations for where the criticality of the immediate post-earthquake recovery state is greater than that of target recovery state of: (a) shelter-in-place, (b) reoccupancy, and (c) functional recovery for the intensity and scenario-based assessments. 146

Figure 7.7. Downtime to achieve Functional Recovery (FR), Reoccupancy (RO), and Shelter-in-Place (SiP) recovery states for the intensity- and scenario-based assessments. 147

Figure 7.8. Mean downtime to achieve functional recovery state for the intensity- and scenario-based assessments including contributions from collapse, irreparable damage, and repairable damage. 149

Figure 7.9. Percentage of repairable realizations in which a component incurs damage that hinders either of recovery states for the scenario-based assessments in (a) Delta; (b) Richmond; (c) Burnaby; and for the intensity-based assessments with (d) 2475-year; and (e) 475-year hazard levels. 152

Figure 7.10. Deaggregation of mean downtime to functional recovery for repairable realizations for the scenario-based assessments in (a) Delta; (b) Richmond; (c) Burnaby; and for the intensity-based assessments with (d) 2475-year; (e) 975-year and (f) 475-year hazard levels. 154

Acknowledgements

First and foremost, I would like to praise and thank God almighty for bestowing upon me the countless blessings and opportunities that have enabled me to bring my thesis to fruition.

I would like to express my sincere gratitude to my esteemed supervisor, Dr. Carlos Molina Hutt, for the opportunity to pursue my research passions. I would also like to thank him for his invaluable supervision, support and mentorship throughout the course of my M.A.Sc. studies. Working as part of his amazing research group, the *Engineering for Seismic Resilience Laboratory*, has been a great honour and an enthusing experience for me, such that I eagerly look forward to our future collaborations. My gratitude extends also to Dr. Jose Centeno for his incisive comments and tremendous support which have helped me improve my thesis.

I would also like to thank my best friends, Shahab Mousavi and Farbod Tavakkoli, for their sincere friendship, all-around support, and uplifting encouragement despite the long distance that currently separate us. I also owe a tremendous amount of gratitude to my cousins, Mehdi and Maryam Khajehpour, who have kindly and generously been there for me as my second family in Vancouver. I am also appreciative of my research colleagues for helping me at various stages of my program, and all my friends in the UBC Civil Engineering department for the wonderful memories.

Last, but certainly not least, I would like to express my deepest gratitude and affection to my parents for their continuous and unparalleled love, sacrifices, patience, and sage advice, without

whom I would never have been able to embark upon this adventurous journey. I am also very thankful to my lovely brother, Sepehr, who has always stood by my side. Words defy me in detailing my family's immeasurable kindness, for which I am eternally indebted.

The funding for this research came from Canada's Natural Sciences and Engineering Research Council under Discovery Grant No. RGPIN-2019-04599, as well as Canada's New Frontiers in Research Fund – Exploration under Grant No. NFRFE-6032018-01060.

To my beloved parents,

for their endless support and encouragement,

without which I would not have been able to realize my dreams.

Chapter 1: Introduction

1.1 Background, Aims and Objectives

Southwest British Columbia is recognized as the most earthquake-prone region of Canada (Earthquakes Canada, 2021). The presence of various active faults in this region can cause different types of tectonic plate movements and contributes to a significant seismic hazard (Earthquakes Canada, 2021). The Cascadia Subduction Zone (CSZ), which is located approximately 120 km from Metro Vancouver, is a significant contributor to the seismic hazard of the region. Megathrust earthquakes in the CSZ are produced as a result of the movement of the Juan de Fuca Plate toward and underneath the North American Plate (City of Vancouver, 2021). Geological records indicate the last large-magnitude (~M9) earthquake in the CSZ occurred in 1700, causing severe damage locally (Arima et al., 1991) and a tsunami that impacted the coastlines of Japan (Rogers et al., 2015). Shallow crustal earthquakes are another hazard contributor in this area. These earthquakes, which are more frequent than large-magnitude CSZ earthquakes, can also be highly damaging (e.g. the 1946 Vancouver Island earthquake) and pose a considerable risk due to their proximity to Vancouver (City of Vancouver, 2021). These motions happen within the continental North American plate to a depth of 35 km as a result of fault movement in crusts (Wang, 2020). The Deep intraslab earthquakes, which can produce less damaging ground motions due to their deep hypocenter (around 50 to 60 kilometers (Wagstaffe, 2016)), but with a similar frequency of occurrence to that of crustal earthquakes, are another contributor to the seismic hazard in the region. These intraslab events are caused by an extension of the subducting Juan De Fuca Plate that has already moved under the Strait of Georgia and the mainland coast (Wagstaffe, 2016). The 2001 Nisqually earthquake is an example of an intraslab earthquake (Wagstaffe, 2016).

Metro Vancouver Regional District is the most densely populated area in British Columbia (Environmental Reporting BC, 2018). Figure 1.1 illustrates the population densities in different Regional Districts of British Columbia in 2017 reported by the provincial government (Environmental Reporting BC, 2018). The high population density in Metro Vancouver has led to a high concentration of buildings and infrastructure in this region. This high exposure (people and assets), coupled with the regional seismicity, contribute to a considerable regional seismic risk. Among the multi-faceted earthquake risks facing Metro Vancouver, the large number of tall residential buildings are of special concern due to their size and high occupancy loads where significant damage to even a single building can cause disproportionately harmful impacts on the community (Molina Hutt et al., 2021). Most modern tall buildings in Metro Vancouver adopt a Seismic Force Resisting System (SFRS) composed of Reinforced Concrete Shear Wall (RCSW) in the form of a centralized core. According to Emporis (2020), more than 500 tall buildings (>8 stories) have been built in Metro Vancouver since 2000, out of which almost 90% are RCSWs. Studies on recent earthquakes (e.g. the 2010 Maule earthquake (Chile) and the 2011 Christchurch earthquake (New Zealand)) demonstrate the efficacy of RCSW buildings in ensuring the life-safety of building occupants (Ji et al., 2017). Nevertheless, the damage level observed in these buildings required considerable repair costs and times, leading to a long-lasting loss of occupancy and a slow recovery of the community (Goretti et al., 2017).

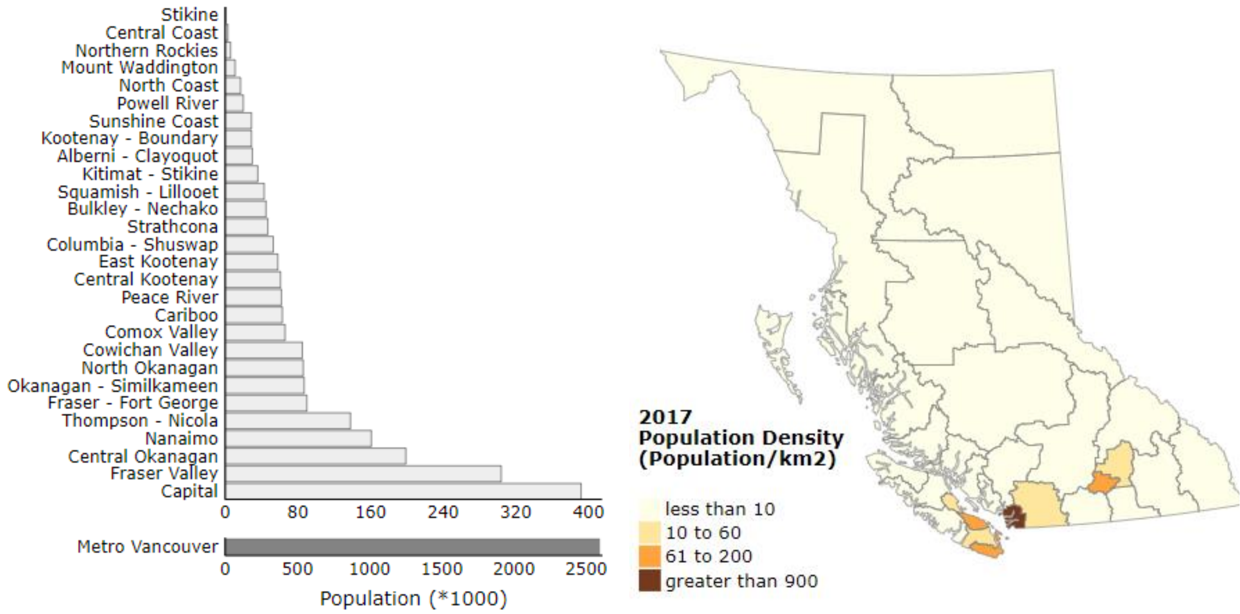

(a) (b)

Figure 1.1. Population density of British Columbia in 2017 (Environmental Reporting BC, 2018): (a) Population of different Regional Districts across British Columbia; (b) Population density map (population per km2) of British Columbia.

Tall buildings in Metro Vancouver are particularly vulnerable to long period ground motions caused by distant, large magnitude subduction earthquakes, such as those generated by the CSZ, due to the effects of the Georgia sedimentary basin, a large elongated northwest oriented forearc basin underlying the Strait of Georgia (Dash et al., 2007) containing deposits distributed over an area of approximately 25,000 km^2 (England & Bustin, 1998). Previous studies, such as Choi et al. (2005); Marafi et al. (2017); and Morikawa & Fujiwara (2013), highlight that long-period spectral accelerations of recorded motions in deep sedimentary basin sites (such as the Georgia sedimentary basin) are higher than those in outside of basin sites. Because tall buildings are characterized by long periods of vibration, the vulnerability of these structures to ground motion shaking is compounded by the presence of deep sedimentary basins. Despite evidence of past large-magnitude CSZ earthquakes, through native oral histories and paleo-seismic records (Atwater et al., 1995), no quantitative observations of ground motion shaking during these events is available (Eksir Monfared et al., 2021). As a first step in addressing this limitation, Frankel et al. (2018) produced 30 sets of broadband synthetic seismograms for M9 CSZ earthquakes. The approach followed in their study accurately reproduced ground motions from the 2003 M8.3 Tokachi-Oki (Wirth et al., 2017) and 2010 M8.8 Maule, Chile (Frankel, 2017) earthquakes. These M9 CSZ earthquake simulations used a 3D velocity model (Stephenson et al., 2017), which characterizes the geological profile of the region, and thereby explicitly accounts for deep sedimentary basin amplification. Despite the amplification effects of deep sedimentary basins on ground motion shaking, current seismic design provisions in Canada, i.e., NBC 2015 (NRC, 2015) do not explicitly account for this phenomenon (Eksir Monfared et al., 2021).

Current building code seismic design provisions intend to ensure life-safety in extreme earthquakes. This is the case even in non-prescriptive designs such as those carried out following performance-based design guidelines such as PEER TBI 2017 (PEER TBI, 2017) where advanced nonlinear structural analysis is required to provide greater assurance of the performance of buildings under strong ground motion shaking (Molina Hutt et al., 2021). Because of this focus on life-safety, current design provisions do not explicitly minimize damage to structural and non-structural elements and preserve the building functionality. EERI (2019) defines the functional recovery as the time required to restore a significant measure of the building's pre-earthquake use. The consequence of neglecting these performance measures are highlighted in the literature. For example, a recent study by Tipler (2014) on modern residential tall RCSW buildings in San Francisco, estimate the repair costs at about 15% of building replacement cost under a design-level earthquake (DE). A similar study by Almufti et al. (2018) indicates a repair cost of 5% for the same building type under a magnitude-7 Hayward earthquake. The downtimes to functional recovery of these studies are about 84 weeks under the design earthquake and 33 weeks under the magnitude-7 Hayward earthquake. Despite the moderate economic losses in these cases, the downtimes are significant and can cause considerable indirect costs.

The National Institute of Standards and Technology (NIST) and the Federal Emergency Management Agency (FEMA) are developing objectives in terms of post-earthquake recovery times (42 U.S.C. § 7705(b), 2018; Senate Bill 1768, 2018). FEMA P-58 (FEMA, 2018) and the Resilience-based Earthquake Design initiative (REDi) (Almufti & Willford, 2013) are among the most common guidelines used to assess earthquake-induced loss and functional recovery time in buildings, respectively. While these guidelines improve our understanding of building recovery, there are limitations associated with their frameworks (Molina Hutt et al., 2022). Some of these limitations are addressed in a recently proposed framework developed by Molina Hutt et al. (2022), which incorporates resilience-based measures, such as robustness and rapidity into the performance assessment of building. Robustness indicates "the ability to withstand a given level of stress or demand without suffering degradation or loss of function" (Bruneau et al., 2003). Rapidity is defined as "the capacity to meet priorities and achieve goals in a timely manner in order to contain losses and avoid future disruption" (Bruneau et al., 2003).

In short, the high concentration of people and assets in Metro Vancouver, coupled with a considerable seismic hazard, results in a substantial seismic risk in the region. This risk is partly driven by tall residential RCSW buildings due to their predominance, as well as their size and high load of occupants. Furthermore, current design codes do not capture deep sedimentary basin amplification in the design of such buildings, nor do they provide an explicit understanding of the expected earthquake-induced economic losses and recovery time. The above mentioned limitations pose the following questions:

- How does the Georgia sedimentary basin influence the performance of modern tall RCSW buildings in Metro Vancouver?
- What are the expected earthquake-induced economic losses and functional recovery times of modern tall RCSW buildings in Metro Vancouver when subjected to different hazards levels?
- What are the main contributors to economic loss and functional recovery time of such buildings?
- How capable are these buildings of withstanding earthquakes without functionality loss?
- How rapidly can these buildings regain functionality?

This research aims to answer the abovementioned questions by evaluating the functional recovery time of modern residential tall RCSW buildings in Metro Vancouver when subjected to ground motions consistent with the code design-level shaking, i.e., NBC 2015, as well as simulated ground motions of M9 CSZ earthquakes, which explicitly account for basin effects.

The results of this study can help policy makers and stakeholders make appropriate decisions based on the expected recovery times to achieve different recovery states.

1.2 Methodology

The research methodology adopted in this thesis is graphically illustrated in Figure 1.2. The methodology consists of six key steps ranging from archetype buildings selection and nonlinear modeling to response simulation and downtime assessment.

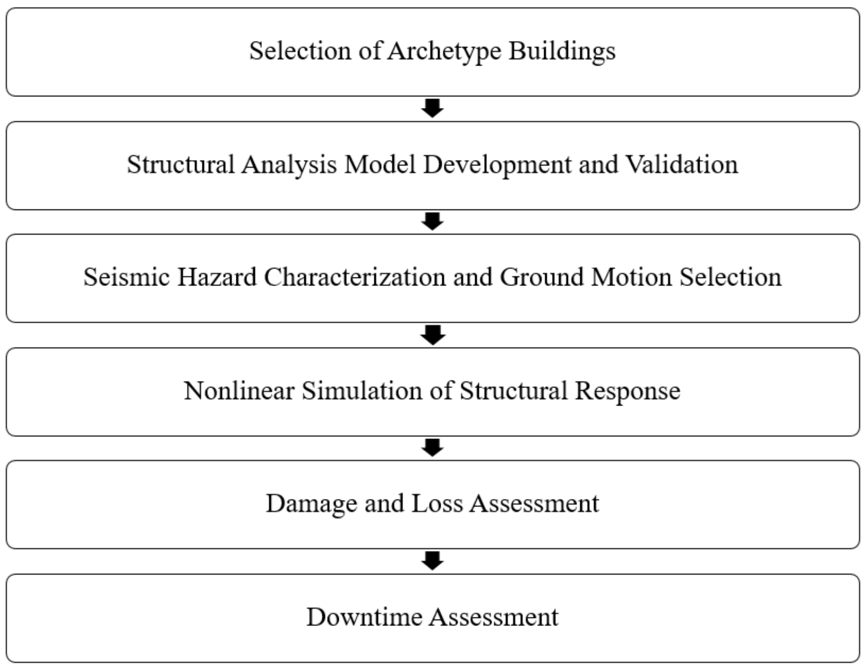

Figure 1.2. Research Methodology.

Step 1 - Selection of Archetype Buildings: Modern 30-story RCSW buildings designed by Eksir Monfared et al. (2021) are considered for the purpose of loss and downtime assessment. These buildings are representative of the current tall buildings construction practice in Metro Vancouver. The seismic force resisting system of these buildings consists of ductile cantilevered shear walls in one direction and fully-coupled shear wall systems in the orthogonal direction.

Step 2 – Structural Analysis Model Development and Validation: Nonlinear models of the selected archetype buildings are created to use in nonlinear time-history analysis. OpenSeesPy (Zhu et al., 2018), a python package adaptation of OpenSees (McKenna, 2011) is used to create the nonlinear finite element models of the building archetypes. The proposed model for shear walls is validated against experimental studies.

Step 3 - Seismic Hazard Characterization and Ground Motion Selection: Seismic hazard characterization is done as well as selection and scaling of ground motions for two types of assessments: intensity-based and scenario-based. Three seismic sources representative of the seismic hazard in Metro Vancouver are included in the intensity-based assessments. 11 ground motions are selected and scaled to a 5% damped NBC 2015 target spectra representative of four hazard levels with return periods of 100, 475, 975, and 2475 years. 30 pairs of simulated ground motions of M9 CSZ earthquakes are used to conduct scenario-based assessments at eight locations across Metro Vancouver with different basin depths.

Step 4 – Nonlinear Simulation of Structural Response: Structural response simulation includes performing nonlinear response-history analyses on the model developed in step 2 using ground motions selected in step 3. The resultant structural responses are transient story drift ratio, racking drift ratio, damageable wall drift ratio, residual drift and floor acceleration. In addition, collapse probabilities for all intensity- and scenario-based assessments are determined.

Step 5 – Damage and Loss Assessment: Damage and loss assessment is conducted on the archetype buildings following the FEMA P-58 methodology based on the structural responses obtained in step 4 and a building performance model constructed using Pelicun (Zsarnoczay & Kourehpaz, 2021), a python-based implementation of FEMA P-58. The expected earthquake-induced economic losses and a deaggregation of the loss results are the key outputs of this step.

Step 6 – Downtime Assessment: Downtime assessment is built upon the results of Step 5 using a framework developed by Molina Hutt et al. (2022). This step includes calculating the recovery time to different recovery states (such as shelter-in-place, re-occupancy, and functional recovery), evaluating recovery trajectories to highlight the post-earthquake usability of the archetype building over time, quantifying building rapidity and robustness, as well as providing a downtime deaggregation of results.

Using these six steps, the downtime to achieve functional recovery (or other recovery states of interest) are evaluated for modern tall RCSW buildings in Metro Vancouver under a range of hazard levels and basin depths through intensity- and scenario-based assessments, respectively. Additionally, the effects of Georgia Sedimentary basin on structural responses, loss, and downtime results, are investigated and main contributors to loss and downtime are determined.

1.3 Thesis Structure

This thesis evaluates the downtime of archetypical modern residential tall RCSW buildings in Metro Vancouver under intensity- and scenario-based earthquakes. To this end, the structure of the thesis is as follows:

Chapter 1 provides an introduction to the research motivation and describes the aims of the study. The overall thesis methodology is presented in this chapter, including the steps required to achieve the goals of this study. An overview of the thesis structure is also provided.

Chapter 2 provides a literature review on the seismic response of RCSW buildings and the design of archetype RCSW buildings in Metro Vancouver. It also includes discussions on deep sedimentary basin effects as well as physics-based ground motion simulations of M9 CSZ earthquakes that account for such effects. Nonlinear modeling recommendations of RCSWs are also discussed in this chapter. In addition, this chapter provides an overview of the damage and loss assessment framework employed in this study, as well as the downtime assessment framework used in this work.

In Chapter 3, the nonlinear model of the RCSWs is described and verified against experimental test data. All other nonlinear analysis modeling assumptions of the archetype building are also described in this chapter.

Chapter 4 introduces different assessments performed in this study (i.e. intensity-based assessment and scenario-based assessment), as well as the ground motion selection and scaling methods associated with these performance evaluations.

Chapter 5 summarizes the results of the nonlinear time-history analysis performed on the building for both intensity-based and scenario-based assessments. These results include different structural responses such as the inter-story drift, peak floor acceleration, and the residual drift. In addition, the concrete and steel strain and the wall shear demand are included. The results of the simulated M9 motions at different sites within the Metro Vancouver Region (with different basin depths) are compared with each other and with the intensity-based assessment results.

Chapter 6 focuses on the damage and loss assessment of the building. The building performance model assumptions are explained in this chapter and the repair costs of the building associated with intensity- and scenario-based assessments are summarized for different locations across Metro Vancouver.

Chapter 7 describes the downtime framework utilized in this study. In this chapter, the downtime of the archetype buildings to different recovery states (such as shelter-in-place, functional recovery, and full recovery) are estimated. Comparisons are made between the downtime evaluations at different locations across Metro Vancouver and between the intensity- and scenario-based assessments.

Chapter 8 summarizes the findings of the study and discusses the limitations of this thesis with recommendations for future research.

Chapter 2: Literature Review

This chapter provides a background of important materials leveraged in this study. In Section 2.1, a brief overview of reinforced concrete shear wall (RCSW) buildings is provided. Section 2.2 describes the archetypical RCSW building used in this study. Section 2.3 provides background on deep sedimentary basin effects. Section 2.4 discusses the physics-based ground motion simulations of M9 Cascadia Subduction Zone earthquakes leveraged in this study. In Section 2.5, common approaches of nonlinear modeling of RCSWs are discussed. Sections 2.6 and 2.7 summarize the frameworks used in this study for loss estimation and downtime assessment, respectively.

2.1 Reinforced Concrete Shear Wall Buildings

Reinforced Concrete Shear Walls (RCSW) are used typically to provide lateral resistance against earthquakes and wind. These systems are capable of providing high stiffness and strength under service loads, as well as ductile behavior under design earthquakes (NIST, 2017b). RCSWs can have numerous configurations depending on the building height and architectural considerations. Common examples of RCSW configurations are shown in Figure 2.1.

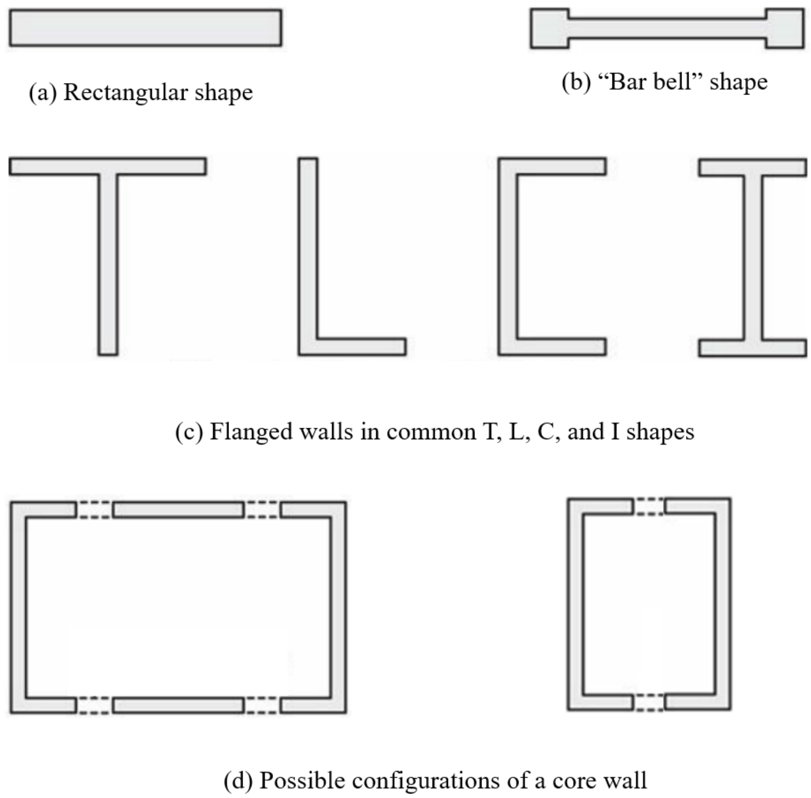

Figure 2.1. Examples of reinforced concrete shear wall cross sections (Moehle et al., 2011).

Core shear wall systems are very common in Metro Vancouver. This system is architecturally beneficial as it “encloses the elevators, stairs, and other vertically extruded elements with coupling beams connecting wall components over doorways” (Moehle, 2015). This system usually consists of cantilever wall piers in one direction and coupled wall piers connected with coupling beams in the other as shown in Figure 2.2. The energy dissipation of such systems entails yielding of the base of the shear walls and ends of the coupling beams as shown in Figure 2.3 (ATC, 2018). When the building is subjected to the lateral force in the coupled direction, a coupling action takes place by formation of axial forces in each pier. This coupling action provides most of the resistance against the base overturning moment. CSA A23.3-14 (CSA, 2014) uses the term Degree of Coupling (DOC) to define the ratio of the moment resisted by the coupling action of the wall piers in the coupled direction to the total base overturning moment and requires a DOC greater than 66% for the system to be considered fully coupled.

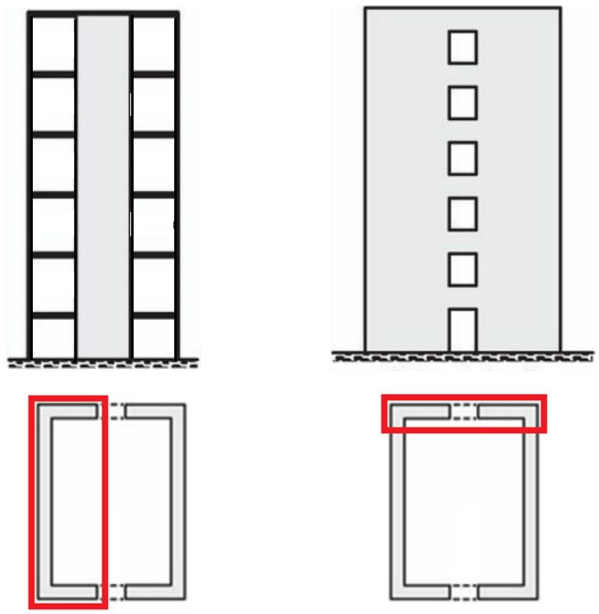

(a) Cantilever direction (b) Coupled direction

Figure 2.2. Schematic of a core reinforced concrete shear wall system (Moehle et al., 2011).

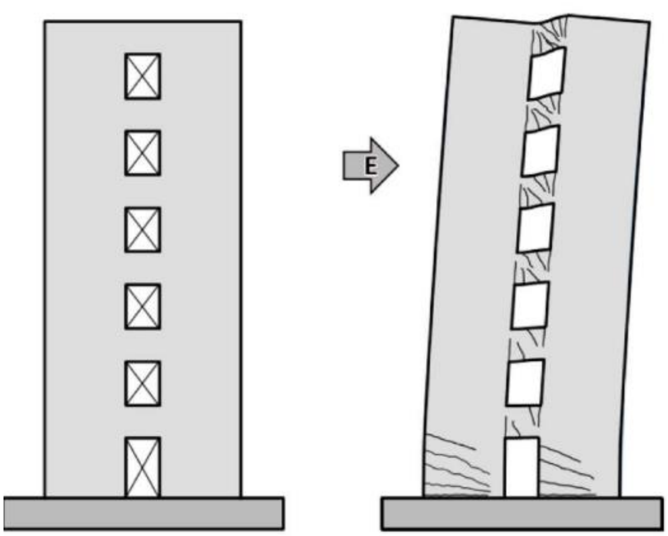

Figure 2.3. Target yield mechanism of coupled reinforced concrete shear wall systems (Moehle et al., 2011).

As per Eksir Monfared et al. (2021), the design of regular RCSW buildings follows a prescriptive approach provided in the National Building Code of Canada (NRC, 2015) where performance-based design is not considered and nonlinearity in the response of the building is not captured explicitly. Certain clauses in the Canadian concrete material standard, CSA A23.3-14 (CSA, 2014), however, are aimed to compensate for the lack of a detailed nonlinear response history analyses in the design of tall RCSW buildings (Eksir Monfared et al., 2021). In the United States, RCSW buildings with a height greater than 73.2 m (240 ft), typically follow a performance-based seismic design approach where nonlinear dynamic analyses are leveraged, providing greater assurance that the buildings meet the performance intended in current building codes to minimize life safety risks under extreme earthquakes (ATC, 2018).

2.2 Archetype Description

A modern tall residential RCSW building designed by Eksir Monfared et al. (2021) is selected in this study as a good representation of current tall buildings construction practice in Metro Vancouver. The building has 30 stories above grade and three basement levels. Each basement level is 3 m high resulting in a total depth of 9 m below the grade. The typical story height is 2.9 m, except the first story level with a height of 3.8 m. Additionally, the building has a bulkhead, 5 m high, which results in a total height of 92.9 m above grade. The isometric view of the building and the plan view of the floors above the grade are shown in Figure 2.4. The superstructure floor plate is 25 m long by 25.9 m wide, and the basement floors have plan dimensions of 30 m by 30.5 m. The Seismic Force Resisting System (SFRS) consists of a 7.3 m by 6.8 m RC core with 610 mm thick walls coupled with 750 mm deep coupling beams in the direction of the shorter dimension, x, and 460 mm thick walls in the other direction, y. The gravity system consists of RC flat slabs supported by RC columns. The RC slabs have a thickness of 200 mm and 350 mm above and below the grade, respectively. The corner columns have a dimension of 610 mm by 610 mm and the rest of the columns have a dimension of 360 mm by 1220 mm. The basement retaining walls are 400 mm thick.

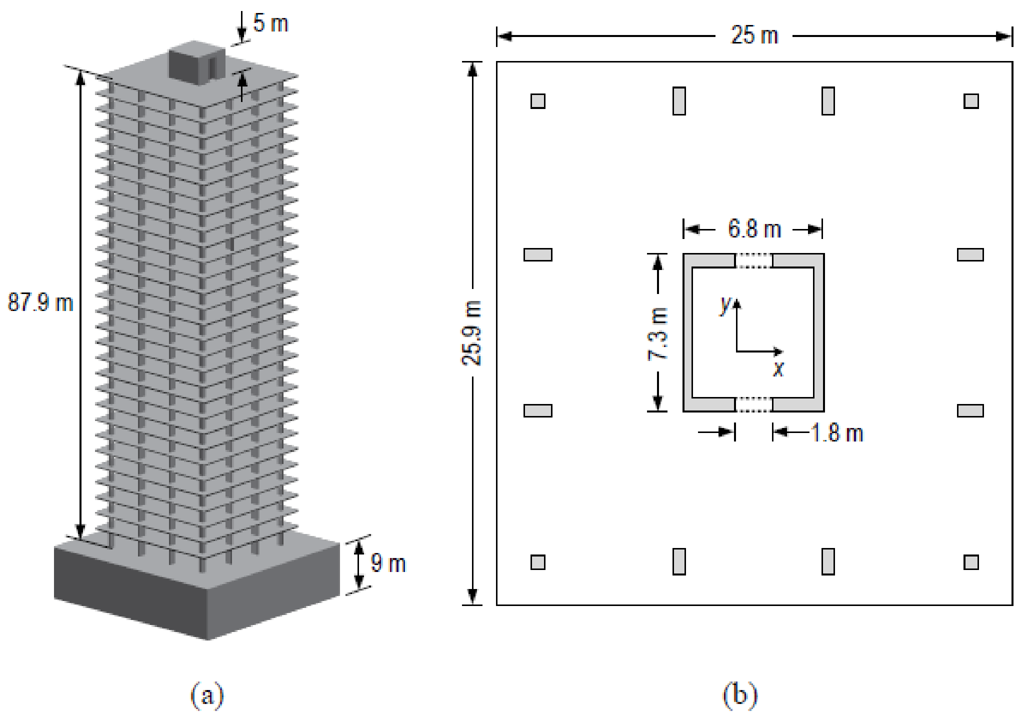

Figure 2.4. Archetype RCSW building: (a) isometric view; (b) superstructure plan view (Eksir Monfared et al., 2021).

The concrete compressive strength is equal to 45 MPA, 35 MPA, and 30 MPA below level 11, from level 11 to level 21, and above level 21, respectively. The concrete modulus of elasticity, E_c, is obtained using Eq. 2.1 per CSA A23.3-14 (CSA, 2014) assuming a concrete density of 2400 kg/m^3.

$$E_c = (3300\sqrt{f_c'} + 6900)\left(\frac{\gamma_c}{2300}\right)^{1.5} \tag{2.1}$$

where $f_c^{'}$ and γ_c are concrete compressive strength and density, respectively. Steel material with a nominal yield strength, f_y, of 400 MPa and modulus of elasticity, E_s, of 200000 MPa are used throughout the building.

The seismic weight consists of the self weight of the core walls and the gravity system, the superimposed dead load, and the façade load. The superimposed dead load is 0.72 kPa in all building levels. The façade load around the perimeter is 1.9 kN/m and 1.9 kPa, 4.8 kPa, and 2.4 kPa live loads are applied in the tower, at grade, and in basement levels, respectively. The resultant seismic mass corresponding to the total superstructure dead load, W, is 144 MN and the dynamic properties of the building are summarized in Table 2.1. Note that the effective bending stiffness factors of the walls used in the modal analysis and building design are 0.5 and 0.6 in the coupled and cantilevered directions, respectively. The bending and shear stiffness modifiers of the coupling beams used in the modal analysis and building design are 0.25 and 0.45, respectively.

Table 2.1. Dynamic properties of the archetype RCSW (Eksir Monfared et al., 2021).

Mode #	1	2	3	4	5	6
Description	Trans. *x*	Trans. *y*	Tors.	Trans. *x*	Trans. *y*	Tors.
Period (s)	5.57	5.41	2.85	1.15	0.92	0.92
Mass Participation	67%	65%	0	19.5%	19.8%	0

Trans.: Translational mode, Tors.: Torsional mode

The modal response spectrum analysis as specified in NBC 2015 (NRC, 2015) is utilized by Eksir Monfared et al. (2021) to obtain the seismic demands of the building archetypes. The archetypes are designed under the 2% in 50-year hazard level (2475-year return period) Site Class C spectrum. Coupling beams and core shear walls are designed per CSA A23.3-14. Summary design of the coupling beams is provided in Table 2.2 where α, A_s, and A_{td} are the angle of diagonal bars, the area of one group of diagonal bars, and the buckling prevention ties of the diagonal reinforcement, respectively. The detailing of the RCSW sections throughout the building height is summarized in Table 2.3 and Figure 2.5. The reader is encouraged to read Eksir Monfared et al. (2021) for more details regarding the analysis and design procedure.

Table 2.2. Summary design of the coupling beams (Eksir Monfared et al., 2021).

Level	Width (mm)	Depth (mm)	Length (mm)	α	A_s	A_{td}
-2 to 12	460	750	1800	16.2°	6-30M	10M@100
13 to 26	460	750	1800	16.2°	6-25M	10M@100
27 to 31	460	750	1800	16.2°	6-20M	10M@100

A_{td}: Buckling prevention ties on diagonal reinforcement
X-YM: X number of bars, Y bar size in mm
YM@Z: Y bar size in mm, Z spacing in mm

Table 2.3. Summary design of the walls (Eksir Monfared et al., 2021).

Level	Zone A		Zone B		Panel 1		Panel 2	
	Long.	**Tie**	**Long.**	**Tie**	**Long.**	**Shear reinf.**	**Long.**	**Shear reinf.**
-3 to 6	12-25M	10M@150	10-25M	10M@150	15M@250	2×20M@200	15M@350	2×20M@150
6 to 11	12-25M	10M@300	10-25M	10M@300	15M@250	2×15M@250	15M@350	2×15M@200
11 to 21	12-25M	10M@300	10-25M	10M@300	15M@250	2×15M@250	15M@350	2×15M@300
21 to 31	12-20M	10M@300	10-20M	10M@300	15M@250	2×15M@250	15M@350	2×15M@300

X-YM: X number of bars, Y bar size in mm
YM@Z: Y bar size in mm, Z spacing in mm

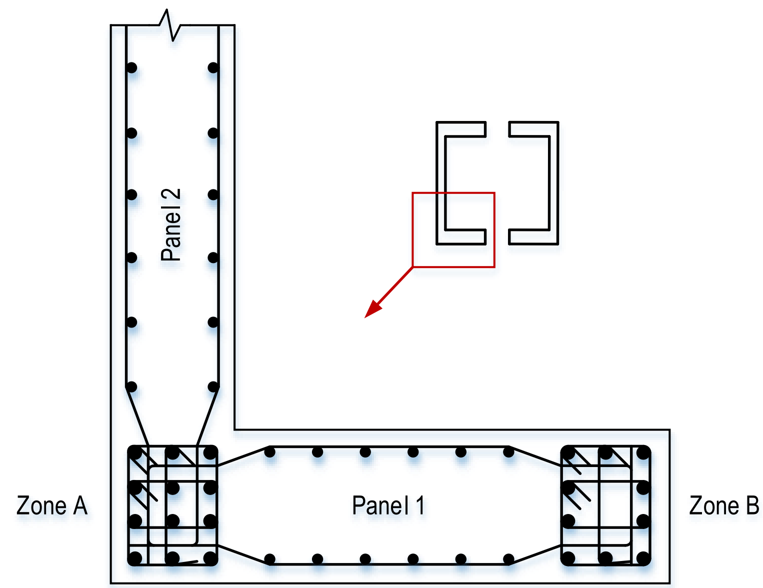

Figure 2.5. Reinforcement layout of the walls (Eksir Monfared et al., 2021).

2.3 Deep Sedimentary Basin Effects

Deep sedimentary basins tend to amplify ground motion shaking intensities at long periods, which are typical of tall buildings. Many research studies have highlighted the importance of basin effects on the response of tall buildings located on deep basin sites. Marafi et al. (2017) evaluated the effects of four Japanese basins during large magnitude subduction interface earthquakes in terms of spectral acceleration, significant duration, and spectral shape. Their study showed consistent increase of spectral accelerations with increasing basin depth. In three of the basins, basin amplification factors greater than 2.0 were reported at periods beyond 2 s. Marafi et al. (2020) evaluated the performance of tall RCSW archetype buildings in Seattle under simulated M9 Cascadia Subduction Zone interface earthquakes, which explicitly account for basin effects, and had median spectral accelerations 15% higher than the Maximum Considered Earthquake (MCE_R) motions at a period of 2 s. Additionally, the collapse probabilities for the M9 motions exceeded the 10% target collapse probability associated with the MCE_R motions. Kakoty et al. (2020) evaluated the impacts of the Georgia sedimentary basin on the response of RCSW buildings in Metro Vancouver by leveraging the same suite of simulated M9 CSZ earthquakes and benchmarked the results against the 2016 BC Hydro ground motions model (GMM) (Abrahamson et al., 2016), which neglects basin amplifications. While spectral accelerations were consistent under the simulated motions and GMM predictions outside the basin, for sites within the basin, GMMs significantly underestimated the hazard at medium-to-long periods. In another study, Eksir Monfared et al. (2021) compared the seismic performance of tall RCSW buildings in Metro Vancouver under simulated M9 CSZ motions as well as under hazard estimates consistent with Canada's 2015 National Seismic Hazard Model (NSHM) (Adams et al., 2015), which neglects the basin effects. The collapse probabilities, earthquake-induced repair cost and repair time under the simulated motions exceeded those under the 2015 NSHM motions at deep basins highlighting the significance of basin amplifications.

Frankel et al. (2018) lists factors contributing to basin amplification of seismic waves as follows: "(1) amplification and resonance of near-vertically propagating S waves, (2) conversion of incident S waves into basin surface waves at the edge of the basin, (3) focusing of S waves by the edge of the basin, and (4) amplification of incoming surface waves" (Frankel et al., 2018). Also, the earthquake location and depth can significantly affect basin amplification as it impacts the azimuth and incidence angle of incoming seismic energy as it enters the basin (Kakoty et al., 2020). Wirth et al. (2019) demonstrated the source dependence of basin amplification by performing 3D simulations of point source earthquakes distributed around Seattle and Tacoma basins in Washington State, which is further supported by the observations of Thompson et al. (2020). In addition, Wirth et al. (2018) have observed that basin amplification is largely independent of the earthquake magnitude and distance from the basin.

Effects of the Georgia sedimentary basin on different seismic sources in southwest British Columbia have been evaluated in previous studies. Molnar et al. (2014a) investigated the effects of the Georgia sedimentary basin on ground shaking by leveraging scenario earthquakes which include deep subducting Juan de Fuca plate earthquakes, i.e., subduction intraslab earthquakes. Molnar et al. (2014b) conducted a similar study on shallow blind-thrust scenario earthquakes, i.e., crustal earthquakes. However, Eksir Monfared et al. (2021) considered scenario earthquakes that include subduction oceanic Juan de Fuca plate over-riding continental North American plate, i.e., subduction interface earthquakes. These simulated motions were generated by United States

Geological Survey (USGS) and the University of Washington (UW) as part of the M9 project (Frankel et al., 2018). This study utilizes the same simulated M9 CSZ earthquakes used by Eksir Monfared et al. (2021).

2.4 Simulated M9 CSZ Earthquakes and Georgia Sedimentary Basin

Frankel et al. (2018) characterized the effects of a megathrust earthquake in the Cascadia corridor by developing a suite of 30 simulated ground motions of M9 CSZ earthquakes. Variation in hypocenter location, extent of the rupture plane and rupture direction are accounted for in this simulation. Frankel et al. (2018) leveraged the 3D P- and S-wave velocity model proposed by Stephenson et al. (2017) to simulate the ground motions using a finite-difference method for periods greater than 1s. The geological profile of the Georgia sedimentary basin developed by Molnar et al. (2014a; b) was integrated into this velocity model. As a result, the suite of simulated ground motions of M9 CSZ earthquakes can explicitly account for the basin amplification effects due to the Georgia basin which underlies the Metro Vancouver region. Nevertheless, the impacts of the basin effects are not explicitly considered for periods less than 1 s due to the implementation of a stochastic procedure to generate the ground motions assuming a constant geological profile for periods below 1s (Marafi et al., 2020).

While many studies in the literature characterize deep sedimentary basin depth as the depth from the surface to soils with a shear wave velocity of 1.0, 1.5, and 2.5 km/s, denoted as $Z_{1.0}$, $Z_{1.5}$, and $Z_{2.5}$ (Day et al., 2008), respectively, recent studies recommend the use of $Z_{2.5}$ for computing basin amplification in the Pacific Northwest where sites with a shallow $Z_{1.0}$ value can still have a deep $Z_{2.5}$ value Wirth et al. (2018). Therefore, as supported by other studies (e.g. Kakoty et al., 2020;

Marafi et al., 2019a; Campbell & Bozorgnia, 2014), $Z_{2.5}$ is a good proxy for deep sedimentary basin depth. Variation of $Z_{2.5}$ over southwest British Columbia is shown in Figure 2.6 along with eight critical locations selected for this study. These locations are the same as those used by Eksir Monfared et al. (2021) and are selected based on their high concentration of tall buildings. As Figure 2.6 suggests, Delta and Richmond are the deepest basin sites with $Z_{2.5}$ values between 3 and 4 km. Surrey and New Westminster have $Z_{2.5}$ values ranging from 2 to 3 km, and Burnaby, Vancouver, and North Vancouver have $Z_{2.5}$ values between 1 and 2 km. West Vancouver falls outside the Georgia sedimentary basin and has a $Z_{2.5}$ value less than 1 km. More information regarding the site characteristics of each location used in this study is summarized in Table 2.4.

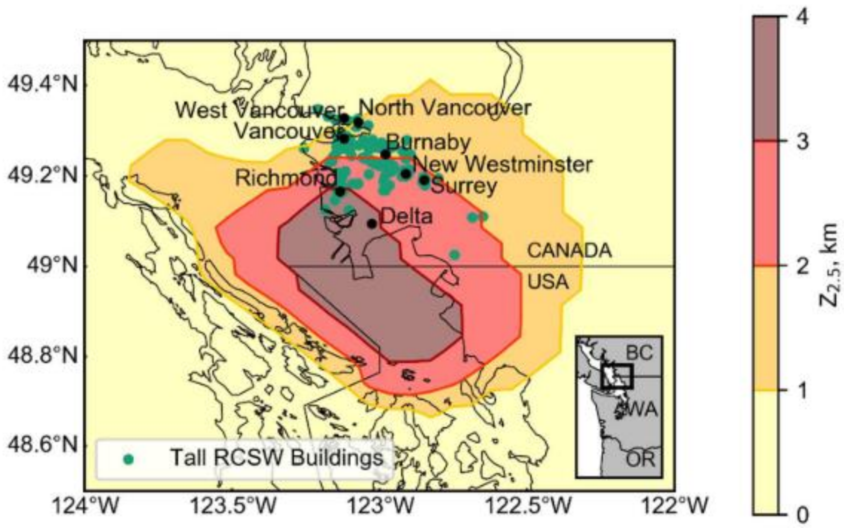

Figure 2.6. Variation of $Z_{2.5}$ across southwest British Columbia, selected locations of study throughout Metro Vancouver as well as geographical distribution of reinforced concrete shear wall (RCSW) buildings (> 8 stories) constructed since 2000 (Eksir Monfared et al., 2021).

Table 2.4. Locations of study within Metro Vancouver including coordinates, Vs30, Z2.5, and SA(T=3s) corresponding to the NBC 2015 2475-year return period spectrum and the average of the simulated ground motions of M9 CSZ earthquakes (Eksir Monfared et al., 2021).

Locations	Latitude (°)	Longitude (°)	V_{s30} (m/s)[1]	$Z_{2.5}$ (km)[2]	*SA*(T=3s) (g)	
					M9	2475-year hazard
West Vancouver	49.33	-123.16	360-760	0.67	0.052	0.191
North Vancouver	49.32	-123.07	360-760	1.18	0.075	0.186
Vancouver	49.28	-123.12	360-760	1.22	0.081	0.197
Burnaby	49.25	-122.98	360-760	1.74	0.109	0.190
New Westminster	49.21	-122.91	360-760	2.23	0.099	0.189
Surrey	49.19	-122.85	180-360	2.23	0.102	0.188
Richmond	49.17	-123.13	180-360	3.22	0.136	0.206
Delta	49.09	-123.03	180-360	3.27	0.143	0.206

[1]Monahan, 2005, [2] Stephenson et al. (2017)
V_{s30}: Average shear wave velocity in the top 30 m of soil
$Z_{2.5}$: Depth to a shear wave velocity of 2.5 km/s
SA: Spectral acceleration

The variation in the 5% damped response spectra of the individual simulated M9 CSZ earthquakes is benchmarked against the NBC 2015 design response spectrum (i.e. 2475-year hazard) in Figure 2.7 for the site located in Vancouver. Note that the response spectrum is plotted for each component of the 30 pairs of simulated motions resulting in 60 response spectra in total. Two scenarios with different rupture distances, R_{rup}, are illustrated in Figure 2.7 to highlight the sensitivity of the spectra to M9 ground motion simulation parameters.

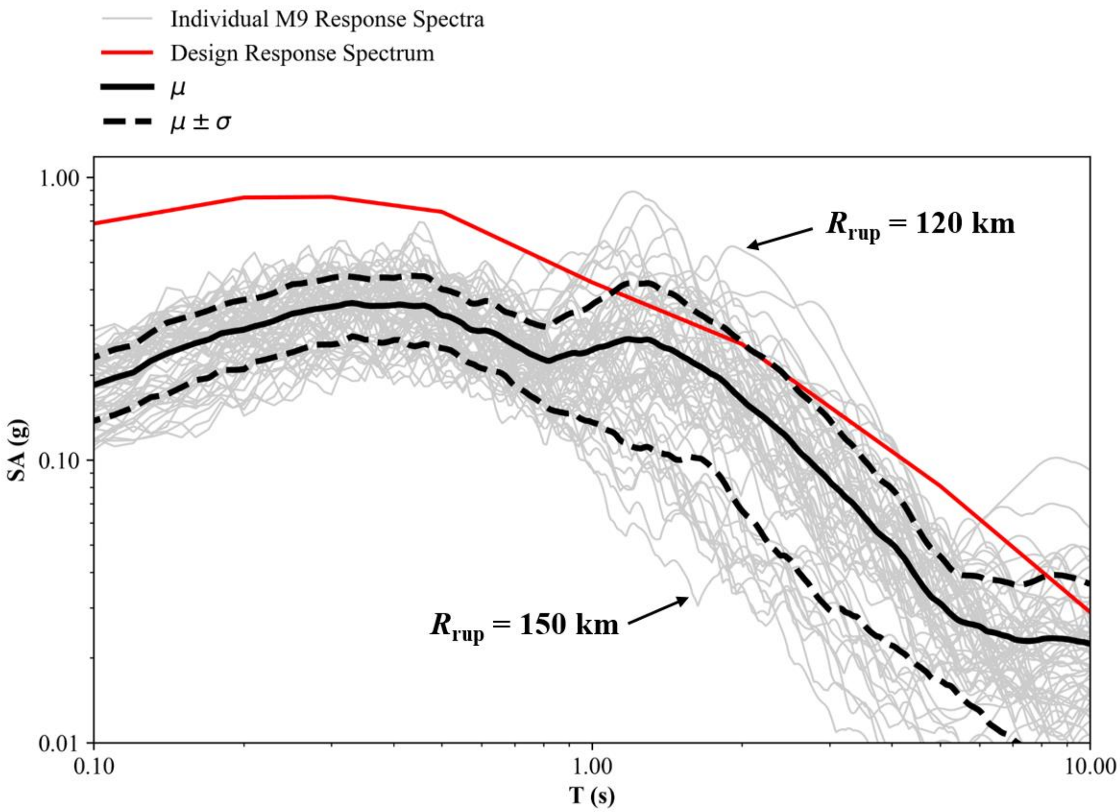

Figure 2.7. Variation of the simulated ground motions of M9 CSZ earthquakes response spectra in Vancouver against the design response spectrum (i.e. 2475-year hazard) (adopted from Eksir Monfared et al., 2021).

Additionally, the mean of the simulated M9 spectra is compared against the NBC 2015 design response spectrum at the selected locations in Figure 2.8. The variation in the spectral accelerations across sites is significantly higher in the M9 motions than in the NBC 2015 motions at medium to long periods. Moreover, the negligible variation of the design spectra at the selected locations highlights the fact that NBC 2015 does not explicitly account for the basin amplifications. Figure 2.8 demonstrates that spectral accelerations are higher at locations with higher $Z_{2.5}$, as previously reported in Figure 2.6 and Table 2.4. Also, the M9 spectral accelerations exceed the corresponding 2475-year hazard spectral accelerations in Delta, Richmond, and Burnaby at medium-to-long periods despite the lower return period of the M9 motions, i.e., 500-year according to Atwater & Hemphill-Haley (1997).

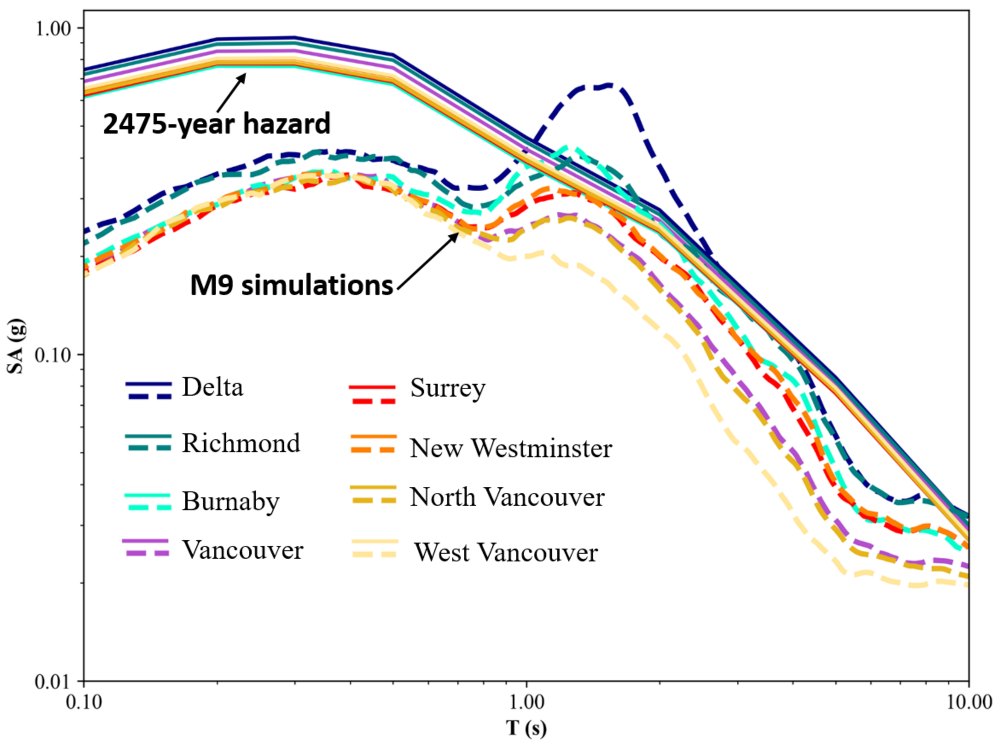

Figure 2.8. Variation of the simulated ground motions of M9 CSZ earthquakes response spectra against the design response spectra (i.e. 2475-year hazard) in different locations (adopted from Eksir Monfared et al., 2021).

The simulated M9 motions are generated assuming an average shear wave velocity in the top 30 meters of soil, Vs_{30}, which represents NEHRP Site Class C (360 m/s < Vs_{30} < 760 m/s) (NEHRP, 2003). Per Monahan (2005), this assumption is valid for Burnaby, New Westminster, Surrey, Vancouver, North Vancouver, and West Vancouver as shown in Table 2.4. Nonetheless, Delta and Richmond have softer soils where the site class can vary between D, E, or F. Similar to Eksir Monfared et al.'s (2021) study, while additional amplification is expected at these two locations, this study assumes a uniform Vs_{30} profile, consistent with the assumption of the Pacific Northwest velocity model used to generate the simulated ground motions of M9 CSZ earthquakes. As a result,

V_{S30} assumptions are consistent both in the design (2475-year spectra) and in the assessment (M9 spectra).

2.5 Nonlinear Modeling of Reinforced Concrete Shear Wall Buildings

In this section, a summary of different nonlinear modeling approaches of the flexure-controlled RCSW buildings is provided with the advantages and disadvantages of each approach. Also, the selected modeling approach used in this study is explained in detail.

When a flexure-controlled wall is subjected to increasing lateral displacement, the damage in the wall typically initiates with development of horizontal cracks in the extreme tension region of the wall and diagonal cracks in the interior of the wall. This is followed by yielding of longitudinal reinforcement in tension in the extreme tension region and spalling of cover concrete in the extreme compression region of the wall. Higher lateral displacement levels cause core damage resulting in exposure of longitudinal reinforcement, buckling of longitudinal reinforcement in the extreme compression region of the wall, crushing of the core concrete in the boundary element and/or web, and fracture of the longitudinal bars in the boundary element (NIST, 2017b).

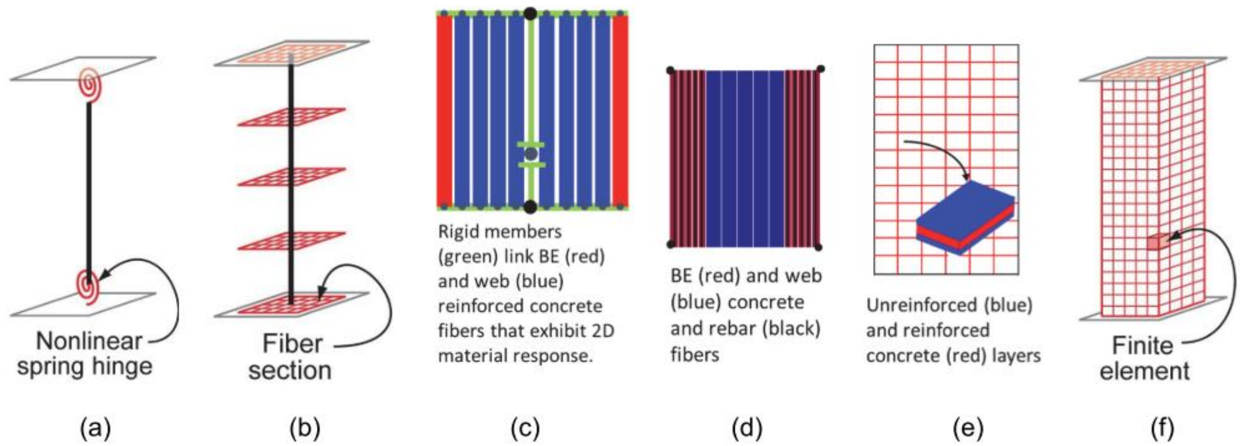

Figure 2.9. Different approaches to simulate the nonlinear response of RCSW: (a) zero-length hinge model; (b) fiber-type beam column element; (c) beam-column element with flexure-shear interaction; (d) fiber-shell element; (e) layered-shell element; (f) 3D continuum elements (NIST, 2017b). Note that BE means boundary element.

NIST (2017b) provides a list of different modeling approaches commonly used to generate nonlinear model of RCSWs as shown in Figure 2.9. The simplest model is the zero-length model (Figure 2.9a) where nonlienar response of the critical section can be captured using a moment-rotation response model assuming a linear axial and shear response or a fiber-type section model with a user-defined plastic-hinge length. While this modeling approach is highly efficient from a computational perspective, it cannot provide accurate simulation of the response (NIST, 2017b). In the fiber-type beam column element model (Figure 2.9b), force- or displacemnet-based beam column elements are used over the height of the wall with multiple integration points to capture the flexural response of the wall through fiber-type section models and nonlinear concrete and steel material models. This modeling approach is computationally efficient and can accurately estimate the resposne of the walls when shear effects are not significant. However, the approach is not suitable for shear walls with significant shear contribution to the overal response of the wall. While this limitation is improved in the fiber-type beam-column element with flexure-shear interaction (Figure 2.9c), this approach is not implemented in commonly employed commercial and research software. The fiber-shell element model (Figure 2.9d) leverages plane stress elements with normal stress-strain response determined by the 1D stress-strain response of the horizontal and vertical strips that lie within the plane of the element and the shear response is defined by a 1D shear stress-strain model decoupled from the flexural response. An advantage of this model over fiber-type beam column element models is the ease of representing the 3D configuraiton of the wall and interaction between wall and other structural components. However, this model is not as computationally efficient as fiber-type beam column elements. The layered-shell element model (Figure 2.9e) employs 3D shell elements with multiple 2D plane-stress layers defined by 2D continuum concrete models with or without horizontal or longitudinal steel bars. Multiple shell elements along the height and length of the wall cross-section are required in this modeling approach. Besides being computationally demanding, the 2D concrete constituitive model can cause numerical instability (NIST, 2017b). Lastly, the 3D continuum element model (Figure 2.9f) employs 3D solid elements, a 3D concrete constituitive model, and a 1D reinforcing steel model. In a 3D continuum elements model, multiple elements are required along the height, length, and the thickness of the wall. This modeling approach is the most computationally demanding one. A more detailed description of each model with its advantages and disadvantages can be found in chapter 7.4 of NIST (2017b).

Fiber-type beam column elements are commonly used in the literature to model the nonlinear response of slender RCSWs (e.g. Pugh et al., 2015; Marafi et al., 2019b; Zhong et al., 2021). This modeling approach provides an accurate, computationally efficient and numerically robust simulation of the flexure-dominated concrete walls with low to moderate shear demand (NIST, 2017b). This model assumes that plane sections remain plane and perpendicular to the neutral axis during bending. Despite these assumptions, experimental tests have shown that, even for slender walls, the strain profiles across critical wall sections do not remain plane (Bohl & Adebar, 2011; Birely, 2012). Nevertheless, fiber sections can provide a sufficiently accurate response of the flexure-controlled shear walls by including the shear response in the model (Pugh, 2012).

As discussed in NIST (2017b), the nonlinear response of the element is captured through numerical integration of the section response at different points throughout the element, namely, at the integration points. At each integration point, a fiber-type discretization of the wall cross-section is utilized to simulate the nonlinear response at the section level. 1D cyclic stress-strain models of steel or concrete are implemented in each fiber that enables simulation of the impact of axial load on flexural response (i.e., P-M interaction). Figure 2.10 demonstrates a fiber-type beam column element model with five integration points used to simulate nonlinear response of a planar shear wall.

Two types of element formulation can be used with the fiber-type beam column elements which are Force Based Element (FBE) and Displacement Based Element (DBE) formulations. The former employs the assumption of linear moment distribution and constant axial force along the length of the element. The latter assumes linear curvature field and constant axial strain field along the length of the element. Pugh (2012) recommended the use of more than five displacement-based elements per story, each with five sections to accurately capture the deformation and load distributions developed in a building's wall. On the other hand, the use of one force-based element with at least five elements per story is recommended by Pugh (2012) to reach an accurate simulation of the wall response. Both FBE and DBE approaches can be adequate for modeling the nonlinear response of walls.

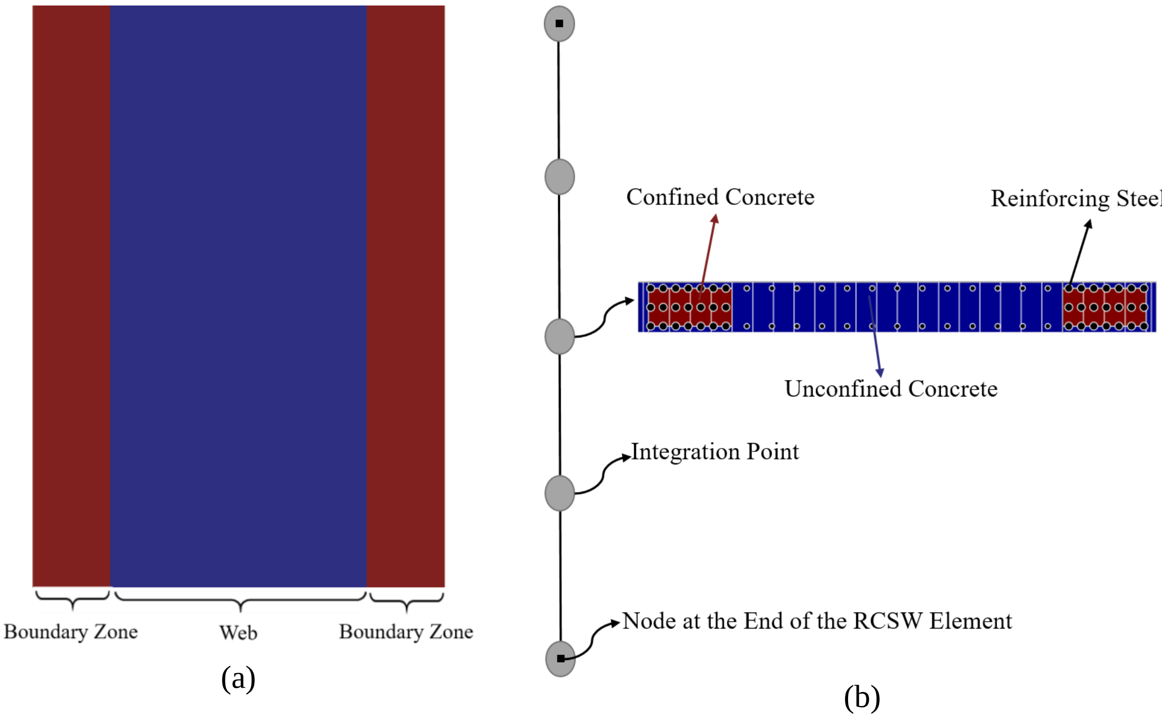

Figure 2.10. Modeling of RCSWs using fiber-type beam column element model: (a) sample shear wall; (b) Fiber-type beam column element model.

As discussed earlier, fiber-type beam column elements provide a better estimation of the wall response where shear response is also accounted for in the modeling. This modeling approach, however, does not account for shear-flexure interaction, i.e., the shear and flexural responses are decoupled. The shear response can be included in different ways depending on the type of element formulation. For FBE formulation, a shear spring is introduced at each fiber section while for the DBE formulation, a shear spring is introduced at the base of each floor (Pugh, 2012). Both linear (Pugh, 2012; ATC-72-1, 2010; PEER TBI, 2017) and nonlinear (Pugh, 2012) shear response models have been proposed in the literature. The effective shear stiffness of the shear wall depends on different factors including the web reinforcement and the axial load; thus a single shear stiffness modifier is not appropriate for analysis of shear walls (ATC-72-1, 2010). Pugh (2012) recommended using a 0.1 shear stiffness reduction factor within the plastic-hinge region and no shear stiffness reduction factor outside the plastic-hinge region. A shear stiffness reduction factor of 0.1 is also proposed by Oyen (2006) and in ATC-72-1 (2010) for walls with a shear strength of $10\sqrt{f_c^{'}}A_v$ where A_v is the effective shear area of the wall. By contrast, PEER TBI (2017) suggests using a 0.5 reduction factor for MCE level nonlinear models and no reduction factors for service level linear models.

The use of FBE formulation is more common in the literature than the DBE formulation since it can provide exact section-level moments, axial loads, and associated deformations when a converged solution state is achieved (NIST, 2017b). The assumption of uniform axial strain along the length of the element in the DBE formulation may result in significant variation in the axial force demand at each integration point and therefore, more elements are required to limit the axial force variation at different integration points (Pugh et al., 2015). The lack of accuracy of the DBE approach is also discussed in Correia et al. (2008) where the strength, loading and unloading stiffness, as well as cyclic strength degradation are found to be more accurately estimated using the FBE approach. Also, Correia et al. (2008) found that the DBE approach tends to results in a stiffer response than the real response of the element and is mostly advantageous in simulating the linear elastic prismatic elements without any distributed loads.

According to Pugh (2012), most slender RCSWs exhibit a softening response at the onset of loss of lateral load carrying capacity which is due to concrete crushing prior to failure. Accurate prediction of this failure mode using fiber-type beam column elements is hard because of severe mesh dependent localization of deformation. To address this issue, material regularization is proposed in the literature where the concrete strain capacity is defined as a function of the mesh-dependent characteristic length and the concrete crushing energy, (i.e., the energy dissipated as the concrete goes from the point of peak strength to the point of residual compressive strength) (NIST, 2017b). In addition to the concrete, steel material regularization is required when the RC section softens and deformations localize in a single fiber section. For reinforcing steel, post yield response and strain capacity are determined as a function of the mesh-dependent characteristic length and a steel yielding energy (NIST, 2017b). The regularized stress-strain behavior of concrete and steel material models is shown in Figure 2.11. In Figure 2.11a, G_{fc} and L_{IP} represent the unconfined concrete crushing energy and the mesh-dependent characteristic length, ε_{0} and ε_{20u} are the strain associated with the points of peak and residual compressive strength of unconfined concrete. In Figure 2.11b, $f_{cc}^{'}$ is the confined concrete maximum strength, E_{cc} denotes the modulus of elasticity of confined concrete, ε_{0c} and ε_{20c} represent the strain associated with the point of peak and residual compressive strength of the confined concrete, and G_{fcc} is the crushing energy of the confined concrete. In Figure 2.11c, f_u and $\varepsilon_{u,exp}$ are the ultimate steel stress and strain, respectively; b denotes the strain hardening stiffness ratio of steel, G_s and L_{gage} determine the steel yielding energy and the gage length used in laboratory testing.

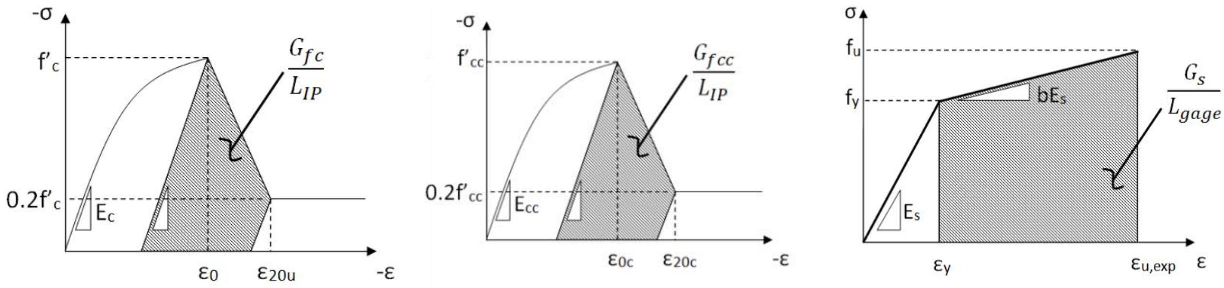

(a) Unconfined concrete compression response
(b) Confined concrete compression response
(c) Steel tension response

Figure 2.11. Regularized material response (Pugh, 2012).

More information regarding material regularization of softening walls can be found in Pugh et al. (2015), including the equations required to obtain the concrete crushing energy and the steel yielding energy. The proposed regularization method works for both planar and c-shaped wall sections (Pugh, 2012).

According to Pugh (2012), material regularization is not appropriate when the critical section does not soften due to strength deterioration of compressive concrete, but instead hardens until steel fracture occurs. In such cases, no damage localization occurs prior to failure and material regularization introduces mesh-sensitivity that would not be present otherwise. Therefore, before performing material regularization, a moment-curvature analysis is required to determine whether the response is softening or hardening. If the former is the case, material regularization is required while no regularization is required otherwise.

2.6 Damage and Loss Assessment

This section provides an overview of performance-based assessment frameworks, a brief description of the well-established FEMA P-58 methodology employed in this study, and an overview of the loss assessment studies performed on tall RCSW buildings.

2.6.1 Performance-based Earthquake Engineering

Performance-based earthquake engineering permits developing a link between expected structural performance and key decision variables such as annual loss and exceedance of certain limit states (e.g. immediate occupancy, life safety, and collapse prevention) (Cornell & Krawinkler, 2000). According to Moehle & Deierlein (2004), the early generations of performance-based earthquake engineering (PBEE), e.g., ATC-40 (1996), FEMA-273 (1997), establish relations between structural responses and different performance-oriented descriptions as shown in Figure 2.12. Moehle & Deierlein (2004) also observed shortcomings in this methodology which include: the lack of robust nonlinear analysis, lack of consistent approaches to relate the engineering demands to the component performance, and the assumption that overall building performance is equal to the worst performing component in the building.

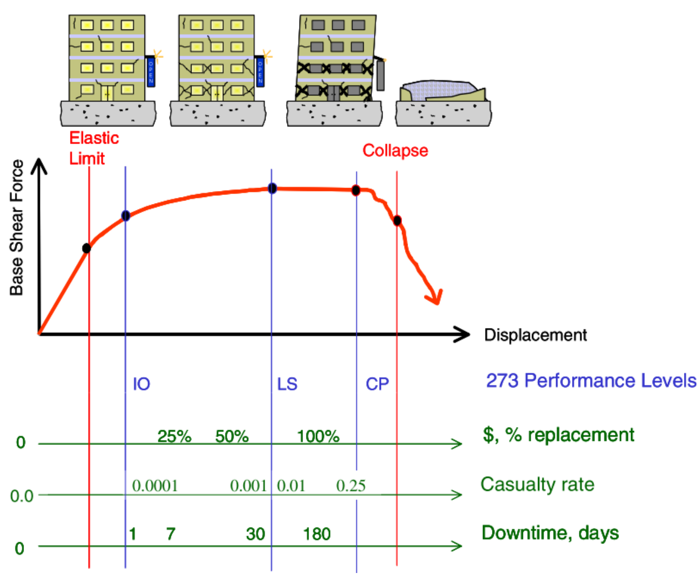

Figure 2.12. First generation performance-based earthquake engineering methodology (after Holmes)(Moehle & Deierlein, 2004).

The Pacific Earthquake Engineering Research Center (PEER) proposed a more rigorous and consistent methodology (Moehle & Deierlein, 2004) which provides the technical background for

FEMA P-58's (FEMA, 2018) seismic performance assessment methodology. This methodology is very well documented and the reader is referred to the extensive FEMA P-58 documents for a detailed description of the methodology. A brief overview is provided here for completeness. The flowchart shown in Figure 2.13, outlines the five major steps required to evaulate the seismic performance of buildings using the FEMA P-58 methodology. These steps are briefly introduced in Sections 2.6.1.1 to 2.6.1.5.

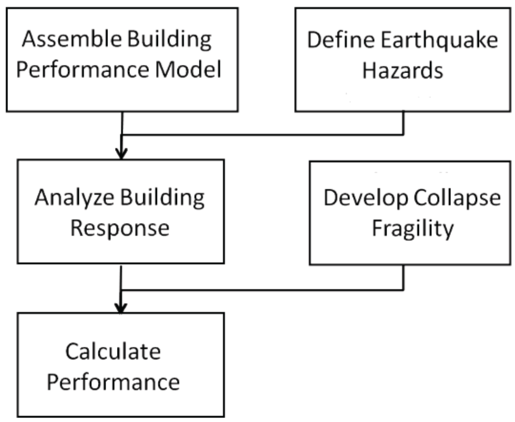

Figure 2.13. Flowchart of FEMA P-58 performance assessment methodology (FEMA, 2018).

2.6.1.1 Assembling Building Performance Model

The performace assessment of the building starts with assembling the building performance model, which includes information regarding building occupancy, size, replacement cost, and replacemnt time. In addition, it includes quantities, location, and different damage types of strucutral and non-structural components of the building, the consequences of damage in terms of different risks and performance measures such as component repair costs and repair times.

FEMA (2018) categorizes vulnerable building components by fragility and component groups where FEMA P-58 defines the former as "sets of similar components with the same damage characteristics in terms of vulnerability and consequences", and the latter as "subsets of a fragility group that will experience the same earthquake demands in response to earthquake shaking".

FEMA P-58 determines the damage to different building components by means of fragility functions, which are lognormal distributions that indicate the conditional probability of incurring damage at a given level building response, e.g., floor acceleration. The damage is then translated into different performance measures by means of consequence functions. Two of the important performance measures are the repair cost and the repair time of the building (Kourehpaz et al., 2020; Molina Hutt et al., 2016, 2019; Ramirez et al., 2012). In this context, repair cost is defined by FEMA P-58 as "the cost of all construction activities necessary to return damaged components to their pre-earthquake condition" (FEMA, 2018). Similarly, FEMA P-58 defines repair time as the time required for a damaged building to recover to its pre-earthquake condition.

2.6.1.2 Define Earthquake Hazards

After assembling the building performance model, the seismic hazard and performance assessment type should be determined. FEMA P-58 defines three types of performance assessments: (1) intensity-based, (2) scenario-based, and (3) time-based (also referred to as risk-based) assessments. According to FEMA P-58, intensity-based assessments evaluate a building's performance when it is subjected to a specified earthquake shaking intensity (e.g. 2% probability of exceedance in 50 years), where shaking intensity is defined by a 5% damped, elastic, acceleration response spectrum. Scenario-based assessments evaluate a building's performance when it is subjected to a specific earthquake magnitude and location relative to the building site (e.g. M9 CSZ earthquakes).

Time-based assessments evaluate building performance over time. In these types of assessments, all possible earthquakes and their probabilities of occurrence are considered.

2.6.1.3 Analyze Building Response

After defining the earthquake hazards, the building response analysis should be carried out. FEMA P-58 allows conducting nonlinear response history analysis or simplified static analysis performed on linear models to determine the *Engineering Demand Parameters* (*EDPs*). The uncertainty in the performance of the building is captured through modeling uncertainty and ground motion record to record variability.

2.6.1.4 Develop Collapse Fragility

The next step of FEMA P-58 seismic performance assessment methodology is collapse fragility development. Collapse fragilities are relationships that define the probability of collapse given a ground motion intensity. These functions are primarily used to obtain the collapse-induced earthquake casualties and losses. Details regarding different methods of collapse fragilities development can be found in FEMA P-58 (FEMA, 2018).

2.6.1.5 Calculate Performance

FEMA P-58 methodology leverages a Monte Carlo procedure to assess a range of possible outcomes from a limited set of inputs. For a particular intensity of motion, statistical distribution of demands are obtained from a series of building response states. Statically consistent demand sets are then generated from these distributions which represent a large number of possible building response states. The demand sets are then used along with the fragility and consequence functions to determine the damage state of the building and the associated consequences. FEMA P-58 then defines as one "realization", each unique outcome of building damage state or consequence resulting from the simulated demand set. The various realizations in this methodology will be then used to produce loss distribution for probabilistic assessment of the building performance. The performance calculation flowchart in each realization is shown in Figure 2.14.

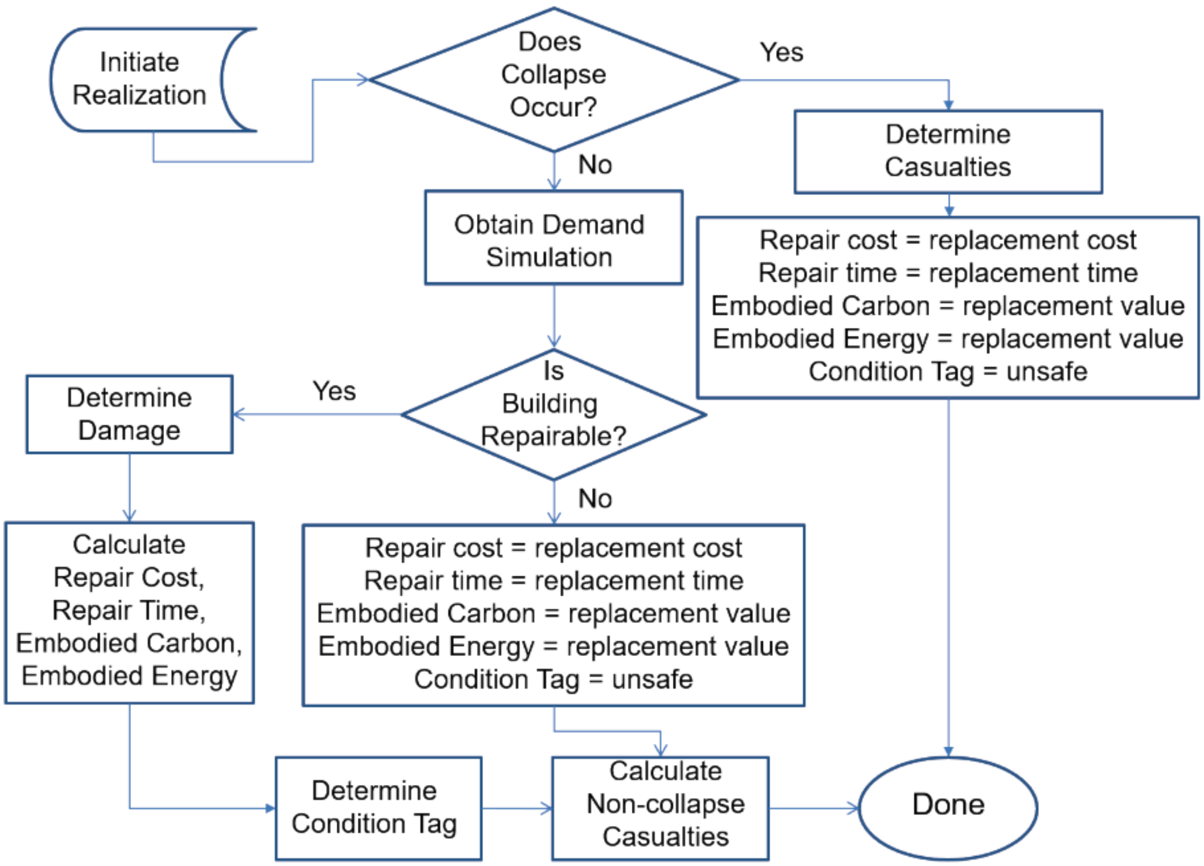

Figure 2.14. Flowchart for performance calculation in each realization (FEMA, 2018).

After initialization of each realization, collapse determination is done by means of collapse fragility functions (FEMA, 2018) or by an input a conditional collapse probability (Zsarnoczay & Kourehpaz, 2021). If collapse is deemed to occur, the repair cost of the building will be equal to the replacement cost of the building. If collapse has not occurred, the methodology checks if the building is repairable using the building repair fragility which determines the probability of the building being irreparable given a residual drift ratio. The repair cost associated with the irreparable realizations are equal to the replacement cost of the building. If collapse has not occurred and the building is repairable in a realization, then the damage state of each component can be obtained based on the demand set of the realization and the corresponding fragility functions. After determining the damage state of each component, consequence functions are utilized to obtain the loss associated with each component. By aggregating the losses across components, the overall building loss is determined. Eventually, loss distributions can be obtained by repeating the loss calculations for all realizations.

2.6.2 Loss Assessment of Tall RCSW Buildings

Several studies have been carried out on the loss assessment of tall RCSW buildings using the well-established FEMA P-58 methodology. Some of these studies are described in the following paragraphs.

Tipler (2014) evaluated the economic loss of a 42-story residential coupled core wall building located in downtown San Francisco and reported loss ratios equal to 15.2% and 30.9% for the DE and MCE_R intensity levels, respectively. In addition, Tipler (2014) proposed two strategies to reduce the financial loss of the building archetype: a damped outrigger system which reduced the loss ratios to 13.6% and 23.9% under the DE and MCE_R levels, respectively, and a base isolated system which reduced the loss ratios to 10.1% and 17.9% under the DE and MCE_R levels, respectively. Tipler (2014) also performed similar loss assessments for each structural scheme by considering non-structural components designed per the Resilience-based Earthquake Design initiative (REDi) (Almufti & Willford, 2013). With this modification, the loss ratios of the baseline, damped outrigger, and the base isolated buildings under the DE level were 8.1%, 7%, and 2.4%, respectively. Similarly, the loss ratios of the baseline, damped outrigger, and the base isolated buildings under the MCE_R level were 27.5%, 19.1%, and 10.5%, respectively. Loss deaggregation results provided by Tipler (2014), highlighted that the main contributor to financial loss is the damage to partitions. Also, most of the structural loss was attributed to the slabs damage. These were consistent among all structural schemes for both DE and MCE_R levels.

Almufti et al. (2018) performed loss assessment on several of 42-story residential RCSW building archetypes located in San Francisco and Oakland under the magnitude 7.0 HayWired scenario. The resultant median repair costs were in the range of 3.1% to 5.1% of the replacement cost. Loss deaggregation results suggested that the main contributor to the financial loss was the damage to the wall partitions.

Kourehpaz et al. (2020) performed loss assessment on a range of eight- to 24-story residential RCSW building archetypes in Seattle. Different design strategies were considered in their study which included a reference building archetype designed per ASCE 7-16 (*ASCE*, 2016), different levels of drift limit and lateral load, and a performance-based design. They performed the loss assessments under the 975-year and 2475-year seismic hazard levels according to 2014 NSHM (Petersen et al., 2014) which does not account for the basin effects, as well as the 2018 NSHM (Petersen et al., 2020) which explicitly accounts for the basin effects. They also performed loss analyses under a range of simulated ground motions of M9 CSZ earthquakes. The resultant mean loss ratios for the reference building archetypes under the M9 motions ranged from 47% for the 24-story archetype to 61% for the 12-story archetype. While these loss ratios were between the 975-year and 2475-year hazard levels per the 2018 NSHM, they exceeded those of the 975-year and 2475-year hazard levels per the 2014 NSHM.

Molina Hutt et al. (2021) performed loss assessments on a 42-story residential RCSW building archetype located in San Francisco, CA (Site Class D) under the DE and MCE_R ground motion shaking intensities. The median loss ratios reported under the DE and MCE_R levels were 7.7% and 13.6%, respectively. In addition, they performed the loss assessment on the same RCSW building archetypes for Site Class B and showed that under lower ground motion intensities and story drifts, the median loss ratios under DE and MCE_R levels were reduced to 3.2% and 5.2%, respectively. Loss deaggregation results demonstrated that the main contributor to financial loss under Design Earthquake ground motions is the damage to structural components and the interior finishes for Site Classes D and B, respectively.

2.7 Downtime Assessment

This section provides an overview of existing downtime assessment methodologies in Section 2.7.1. A recent framework developed by Molina Hutt et al. (2022) is leveraged for the downtime assessments conducted in this study. A summary of this framework is provided in Section 2.7.2.

2.7.1 Background on Downtime Assessment

FEMA P-58 (FEMA, 2018) defines repair time as the time required for a damaged building to reach its pre-earthquake condition. Similar to the repair cost calculation, for each repairable Monte

Carlo realization, the damage is translated to repair time by means of time consequence functions. The repair time of collapse and irreparable realizations are equal to the building replacement time. The FEMA P-58 methodology conducts the repair time calculation in series, which assumes work occurs sequentially across floors, and in parallel repair, where work occurs simultaneously on all floors. While FEMA P-58 has a well-established methodology to calculate repair costs, it has many shortcomings in determining the repair time of buildings (Molina Hutt et al., 2022). For instance, the FEMA P-58 methodology only determines the downtime to achieve full recovery, the recovery state where the building achieves its pre-earthquake functionality, and not any intermediate recovery states. Additionally, FEMA P-58 considers the workforce only based on the building floor area and not on the extent of building damage. FEMA P-58 also assumes only one trade can make repairs at a time on a floor. Most importantly, the impeding factor delays such as contractor mobilization, financing, and inspection are not included in repair time calculation within the FEMA P-58 methodology (Comerio, 2006).

The Resilience-based Earthquake Design initiative (REDi) (Almufti & Willford, 2013) addressed some of the issues associated with the FEMA P-58 methodology to calculate downtime. For instance, the REDi guidelines account for the impeding factor delays and utility disruptions. Also, in addition to the full recovery state considered in FEMA P-58, the REDi guidelines introduce two more recovery states which are reoccupancy and functional recovery. Reoccupancy is the state where the building is safe enough to occupy, and functional recovery is the state where the building restores its functionality. In the REDi guidelines, a repair class is assigned to each component based on its damage state and what damage state is hindered by such damage. The repairs required to achieve a recovery state can then be obtained from the repair class of each component. Some of the limitations of the REDi guidelines are outlined in Molina Hutt et al. (2022). For instance, the REDi methodology utilizes the reoccupancy recovery state to determine if the building is safe enough to occupy (i.e. it can be used for shelter). However, necessary repairs to achieve the reoccupancy recovery state are overly conservative. Many researchers recommended relaxed habitability standards for sheltering criteria in buildings (SPUR, 2012; FEMA P-2055, 2019). In addition, the REDi guidelines assume non-structural components repair begins only after repairs of all structural components in the building are complete and it assumes these are carried out one story at a time. Terzic & Yoo (2016) noted that following the 1994 Northridge earthquake, contractors repaired several floors at a time and some non-structural components such as the elevators and the staircases were repaired in parallel with the structural elements. Another limitation of the REDi guideline is the lack of provisions for repair time calculation of buildings with high residual drift ratios. Such cases are deemed to be irreparable and contribute to downtime significantly as highlighted in past research (e.g. Molina Hutt et al., 2019) due to the need to demolish and reconstruct the building.

Tipler (2014) assessed the functional recovery time of a 42-story residential coupled core wall building located in downtown San Francisco using the REDi guidelines. For the DE and MCE_R intensity levels, functional recovery times of 588 and 959 days were reported, respectively. Also, Tipler (2014) proposed two structural systems to enhance the performance of the building archetype: a damped outrigger system which can reduce the functional recovery downtime to 434 and 770 days under the DE and MCE_R levels, respectively, and a base isolated system with which the functional recovery times were reduced to 301 and 623 days, respectively. In addition, Tipler (2014) performed similar assessments on the above-referenced structural schemes considering an enhanced scheme for non-structural components design per the REDi guidelines. With this modification, the functional recovery time of the baseline, damped outrigger, and the base isolated buildings under the DE event were significantly reduced to 203, 140, and 42 days, respectively. Similarly, the functional recovery time of the baseline, damped outrigger, and the base isolated buildings under the MCE_R event were significantly reduced to 728, 588, and 357 days, respectively. Results of this study suggested that by reducing both structural and non-structural components damage (particularly damage to the partitions), a timely recovery can be achieved.

Almufti et al. (2018) evaluated the downtime to achieve reoccupancy and the functional recovery time of 42-story residential RCSW building archetypes located in San Francisco and Oakland under the magnitude 7.0 HayWired scenario and reported median reoccupancy downtimes ranging from 121 to 139 days and functional recovery downtimes ranging from 224 to 245 days. The governing factor of the total downtime of the archetypes were found to be the contractor mobilization impeding factor delays.

In a study by Molina Hutt et al. (2021) on a 42-story residential RCSW building archetype located in San Francisco, CA (Site Class D), functional recovery times of 222 and 512 days were reported under the DE and MCE_R levels, respectively. Major contributors to total functional recovery time were found to be the contractor mobilization and other impeding factor delays which can be reduced significantly by employing the San Francisco's Building Occupancy Resumption Program (BORP) (Lang et al., 2018) and other mitigation measures, which can reduce the total functional recovery time under the DE and the MCE_R levels to 122 and 433 days, respectively. The main contributors to functional repairs were elevators, structural repairs, and mechanical equipment. In addition, they performed the downtime assessment on the same archetype in a Site Class B site (i.e., lower intensities and story drifts). The resultant downtime under the DE and MCE_R levels were 145 and 182 days, respectively. These values were reduced to 67 and 85 days under the DE and MCE_R levels, respectively by employing mitigation measures to minimize impeding factor delays.

In addition to the above-mentioned studies, ATC (2018) provides a good overview of the recent studies conducted on the downtime assessment of tall buildings. Per ATC (2018), the building damage under earthquake ground motions is very sensitive to the story drift ratio. While a story drfit limit of 2% is required by current US building codes for the DE event, the corresponding functional recovery time would be on the order of a year or more (ATC, 2018) which far exceeds the one month functional recovery goal suggested by this report. Therefore, this guideline provided the following recommendations to achieve the proposed target: (1) limiting the drift ratios to 1% under the DE earthquake, (2) enhancing the design and specification of critical MEP/elevator systems, and (3) implementing BORP and other measures to mitigate impeding factors for recovery.

2.7.2 Downtime Assessment Framework

Molina Hutt et al. (2022) proposed a framework to assess earthquake induced downtime which improves the limitations associated with FEMA P-58 and REDi guidelines frameworks. Downtime in this context is the time to achieve a recovery state after an earthquake. Five different recovery states are considered in the framework which are stability, shelter-in-place, reoccupancy, functional recovery, and full recovery. This framework is identical to FEMA P-58 methodology from structural simulation to component repair time estimates. However, it is different in estimating the building performance in terms of downtime. The methodology begins with evaluating the extent of damage to the building to determine the usability of the building after an earthquake. Next, the methodology evaluates the impeding factor delays which are different factors that can delay the initiation of repair activities. Some examples are building inspection, engineering services, and mobilizing a contractor. In the third step, the framework determines the building's repair time to the desired recovery state which depends on the sequence of repairs and number of workers. In the fourth step, a temporal recovery trajectory of the building is provided by the framework based on the delay time and the repair time. Similar to the FEMA P-58 methodology, this methodology utilizes thousands of Monte Carlo simulations to address uncertainties which results in thousands of downtime realizations and recovery trajectories with the same likelihood of occurrence. Lastly, the framework provides probabilistic resilience-based measures, robustness and rapidity, which are helpful measures for decision makers. More details about each of the framework steps are provided in the following sections.

2.7.2.1 Recovery States and Post-Earthquake Usability

Molina Hutt et al. (2022) considered five distinct recovery states in their downtime estimation framework. The recovery states and the associated building conditions and repair classes are summarized in Table 2.5. The building condition describes the condition of the building when the recovery state is achieved and the associated repair class in Table 2.5 is the repair class that hinders achieving the corresponding recovery state. Similar to the REDi guidelines, this framework assigns repair classes to different component damage states. Each recovery state is achieved only after repairing all damaged components flagged with a certain repair class, which indicates such damage hinders achieving that recovery state.

Table 2.5. Recovery states, building condition, and associated repair class for downtime estimation (Molina Hutt et al., 2022).

Recovery State	Building Condition	Associated Repair Class
Stability	Significant structural and non-structural damage that does not compromise the building stability	5
Shelter-in-place	Moderate structural and non-structural damage that does not threaten the safety of residents	4
Reoccupancy	Cosmetic structural and moderate non-structural damage	3
Functional recovery	Cosmetic structural and minor non-structural damage	2
Full recovery	No damage, pre-earthquake functionality maintained or restored	1

The Molina Hutt et al. (2022) framework proposes two additional recovery states to those defined in the REDi guidelines (i.e. the stability and shelter-in-place recovery states). The stability recovery state is the condition where the building might not be safe for the residents to enter, but it is stable and reparable. The risk of falling debris and aftershock collapse risks is considered negligible in this recovery state. The shelter-in-place recovery state is defined by SPUR (2012) as "a resident's ability to remain in his or her home while it is being repaired after an earthquake – not just for hours or days after an event, but for [the] months it may take to get back to normal". Definition of the reoccupancy recovery state in REDi guidelines is similar to the shelter-in-place recovery state in Molina Hutt et al. (2022) methodology. However, the criteria that REDi guidelines define to achieve the reoccupancy recovery state are more stringent than those proposed by Molina Hutt et al. (2022) for the shelter-in-place recovery state. EERI (2019) defines functional recovery as a "post-earthquake state in which [building] capacity is sufficiently maintained or restored to support pre-earthquake functionality". In this recovery state, the building should have primary functionality and utility functionality should also be satisfied to attain this recovery state. The last recovery state considered in the Molina Hutt et al. (2022) framework is the full recovery state where the building achieves its pre-earthquake condition.

2.7.2.2 Impeding Factor Delays

Several factors can delay the start of damage repairs (Comerio, 2006; Bilau et al., 2015; Marquis, 2015). The REDi guidelines used the term, impeding factors, to refer to these delays. The Molina Hutt et al. (2022) framework considers the following impeding factors: (1) post-earthquake inspection, (2) stabilization, (3) engineering mobilization and review, (4) permitting, (5) contractor mobilization, and (6) financing. Lognormal cumulative distributive functions are proposed to represent these impeding factor delays. By sampling these functions, the duration for each impeding factor can be obtained. This framework assumes the sequencing of the impeding factors as demonstrated in Figure 2.15. If the building experiences no seismic damage, i.e., the maximum repair class is equal to zero, the delay estimates will be zero.

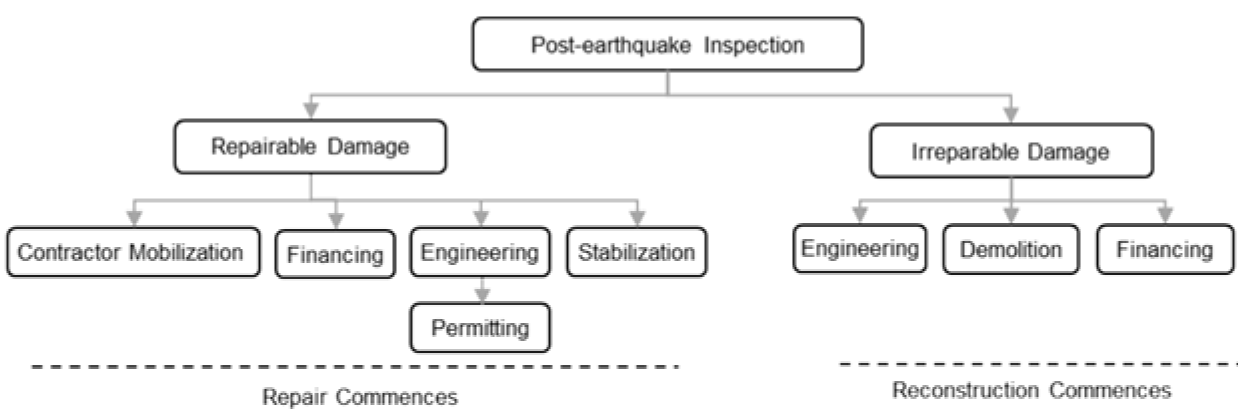

Figure 2.15. Sequencing of impeding factor delays for downtime estimation (Molina Hutt et al., 2022).

As demonstrated in Figure 2.15, post-earthquake inspection determines if the building is reparable or irreparable. If the building damage renders it irreparable, reconstruction delay estimates are considered in the framework which includes engineering, demolition, and financing. The associated impeding factor duration would be equal to the duration of inspection plus the maximum of the duration of engineering, demolition, and financing. If the building damage renders it reparable, different impeding factors considered in the framework are stabilization, contractor mobilization, financing, as well as engineering and permitting. Delays associated with the contractor mobilization are estimated for each repair sequence as described later in this chapter. Similar to the irreparable damage case, the total impeding factor duration is equal to the sum of the inspection delay and the maximum of the delays associated with stabilization, engineering and permitting, contractor mobilization (for each repair sequence), and financing.

As described by Molina Hutt et al. (2022), the stabilization delay is the time required to mobilize the emergency crews and perform necessary repairs to minimize the risk of instability or falling of debris. The engineering delay is the time required to assess the structural damage to the building after the earthquake and propose repair strategies if required. The time needed for local building officials to review and approve the repair strategy is reflected in the permitting delays. It should be noted that the Molina Hutt et al. (2022) framework only accounts for engineering and permitting delays if there is structural damage and the length of delay is different depending on the extent of damage. The contractor mobilization delay is the time needed to “find available contractors, to complete the bidding process, to procure materials and equipment, and to mobilize the necessary labor force” (Molina Hutt et al., 2022). Molina Hutt et al. (2022) followed Paul et al.'s (2018) approach to estimate the contractor mobilization delays for different repair sequences as opposed to REDi guidelines, which consider a single contractor mobilization delay for all repair sequences. “The financing delay accounts for the time required to obtain the funds necessary to carry out repairs” (Molina Hutt et al., 2022). This impeding factor is a function of the economic loss ratio and the method of financing. Three methods of financing are considered in this framework which are insurance, private loans, and public loans. More details about impeding factors delay estimation are provided in Molina Hutt et al. (2022).

2.7.2.3 Building Repair Time

After the estimation of different impeding delay factors, the time to repair all components required to achieve the desired recovery state is evaluated based on the repair class associated with each component (Molina Hutt et al., 2022). Then, the building repair time is estimated based on sequencing of repairs and the workers assigned to each repair sequence. Seven repair sequences defined in this framework are as follows: (1) RS1 which represents structural repairs, (2) RS2 which denotes the interior repairs (e.g. plumbing and partitions), (3) RS3 which represents repairs to the building envelope (e.g. curtain wall glazing), (4) RS4 denotes the mechanical equipment repairs, (5) RS5 demonstrates the electrical equipment repairs, (6) RS6 corresponds to elevator repairs, and (7) RS7 which refers to staircase repairs.

Based on the damage state of each component, FEMA P-58 determines the repair time in worker-days utilizing the associated consequence functions. By dividing the repair time by the number of workers contributing to the repair efforts, the repair time in days can be obtained. The Molina Hutt et al. (2022) framework accounts for the contribution of four different factors in worker allocation: (1) the number of damaged units per Paul et al.'s (2018), (2) the floor area to consider the limitation associated with the number of workers assigned to a repair path on a given floor to prevent congestion (FEMA, 2018), (3) contractor resource limitations per Paul et al.'s (2018), and (4) site restrictions per the REDi guidelines.

After determining the repair time of each repair sequence and each floor, the repair time of each repair phase is calculated. Each repair phase is group of floors that will be repaired simultaneously. This framework assumes each repair phase consists of three floors. Therefore, the repair time of each repair sequence in a given phase is equal to the maximum repair time in each sequence among all floors in that phase. Thus, the time to complete repairs for repair sequence i (RS_i) on floor j, which is part of repair phase n, is the sum of (1) impeding factor delays for RS_i, (2) the sum of repair times for RS_i in each phase from 1 to n-1, and (3) the repair time of RS_i on floor j.

In the next step of the framework, the repair time associated with each repair path is determined. Repair paths determine the order of repairs needed to be carried out. Each repair path consists of one or more repair sequences. Based on the study by Terzic & Yoo (2016) on the repair process after the 1994 Northridge earthquake, contractors can perform the elevator and staircase repairs in parallel with the structural repairs in groups of two to three floors at a time. These studies further show that the interior repair starts immediately after the structural repair completion. Based on these observations, Molina Hutt et al. (2022) considered the following repair paths: (A) Repair path A starts with structural repairs (RS1) followed by the interior repair (RS2), the mechanical equipment repair (RS4), and the electrical equipment repair (RS5) on each floor; (B) Repair path B represents the exterior repair (RS3); (C) Repair path C represents the elevator repair (RS6); and (D) repair path D represents the staircase repairs (RS7). This framework assumes all four repair paths proceed in parallel. Details regarding the calculation of the repair time associated with each repair path is provided in Molina Hutt et al. (2022). For each of the four repair paths, the methodology calculates a recovery trajectory which provides a floor-wise recovery time for each repair path. The governing trajectory for a realization is the upper bound time of the four individual trajectories and would not necessarily represent any single repair path.

This process is repeated for thousands of Monte Carlo realizations and a governing recovery trajectory is obtained for each realization. The methodology gives the median trajectory after sorting all trajectories with respect to the final downtime, the time at which the building fully achieves the desired recovery state. For collapse or irreparable realizations, downtime is equal to the building replacement time which consists of the time for demolition and reconstruction. Molina Hutt et al. (2022) suggested considering two weeks per floor to calculate the reconstruction time.

2.7.2.4 Robustness and Rapidity

Two performance metrics are proposed by Molina Hutt et al. (2022) which can be used to determine the rapidity and robustness of buildings, quantitatively.

Robustness is defined as “the ability [of the building] to withstand a given level of stress or demand without suffering degradation or loss of function” (Bruneau et al., 2003). Molina Hutt et al. (2022) proposed a robustness performance metric described as the probability of a building not achieving a target recovery state immediately after an earthquake with a pre-defined ground motion shaking intensity. This probability should be less than the robustness target of *Y*% as shown in Eq. 2.2 (Molina Hutt et al., 2022).

$$P(\text{Criticality}_{RS} > \text{Criticality}_{\text{TARGET-RS}}) < Y\% \tag{2.2}$$

where Criticality_{RS} and $\text{Criticality}_{\text{Target-RS}}$ are the criticality of the immediate post-earthquake recovery states and the criticality of the target recovery state, respectively. To better understand the concept of criticality of a recovery state, it can be linked to the repair class of a recovery state as shown in Table 2.5. Criticality of recovery state “A” is higher than that of recovery state “B” if the repair class associated with recovery state “A” is higher than that of recovery state “B”. Therefore, to use Eq. 2.2, one should first obtain the percentage of realizations for which the repair class associated with a building recovery state immediately after the earthquake is higher than that of the target recovery state (i.e., $P(\text{Criticality}_{RS} > \text{Criticality}_{\text{Target-RS}})$). Then the resultant probability should be compared with the robustness target of *Y*%.

Molina Hutt et al. (2022) suggests setting *Y* equal to 10% for a “functional-level earthquake” (i.e. ground motion with 10% probability of exceedance in 50 years) following the “function loss” performance metric defined by 2015 National Earthquake Hazards Reductions Program (NEHRP, 2015) that requires all buildings in risk category IV to have a probability of not being operational after a functional-level earthquake of 10% or less.

Rapidity is defined as “the capacity to meet priorities and achieve goals in a timely manner in order to contain losses and avoid future disruption” (Bruneau et al., 2003). To evaluate this performance metric, FEMA P-2082 (FEMA, 2020) recommends assigning target functional recovery downtimes to new buildings based on the building’s risk category. The tendency estimates, i.e., mean or median results, are not good measures to evaluate rapidity due to the high variation in downtime estimates (Molina Hutt et al., 2022). Thus, Molina Hutt et al. (2022) proposed a performance metric to determine if the probability of not achieving a recovery state within a specified timeframe after the earthquake is less than a threshold, *Y*% as shown in Eq. 2.3 for the functional recovery state.

$$P(DT_{FR} > DT_{TARGET}) < Y\% \tag{2.3}$$

where DT_{FR} is the estimated downtime to the functional recovery, DT_{TARGET} is the target downtime, and *Y* is the threshold beyond which building performance is unacceptable. Molina Hutt et al. (2022) suggested using a threshold of 10% (for a risk category II building based on FEMA, 2020) and the DT_{TARGET} of four months for the 475-year hazard level per Poland (2009).

Chapter 3: Structural Analysis Model Development and Validation

This chapter provides details of the structural model developed in this study for the purpose of performing nonlinear time-history analyses. Section 3.1 provides a brief description of the finite element software OpenSeesPy, and the author's motivations to use it in this study. Section 3.2 provides an overall description of the building model and subsections 3.2.1 to 3.2.6 describe the modeling approach and assumptions in more detail.

3.1 OpenSeesPy

OpenSeesPy (Zhu et al., 2018) is a python interpreter for OpenSees (McKenna, 2011). OpenSeesPy was developed in 2018 and has since been widely used by researchers (e.g. Zou et al., 2020 and Slotboom, 2020). One of the advantages of OpenSeesPy over OpenSees is the suitability of python for scientific computing applications. Tcl, the language used to write OpenSees applications, only uses string data type, which makes the mathematical expression's syntax more difficult (Zhu et al., 2018). In addition, many python libraries such as Matplotlib, Numpy, and Pandas can be used for post-processing of the results as done in this study. The python environment of OpenSeesPy makes it particularly useful for conducting studies which require many simulations such as reliability studies and sensitivity analyses.

OpenSeesPy's automation capability is a suitable choice for this study given that more than 500 nonlinear analyses are required for the performance-based assessment framework. In addition, the python environment of OpenSeesPy facilitates going from OpenSees to the loss assessment tool, Pelicun, and then from Pelicun to the downtime tool, TREADS (Molina Hutt et al., 2022), all within Python.

3.2 Building Model

The nonlinear model of the 30-story residential RCSW building archetype in the cantilevered direction is described in this section. Note that this thesis only explores the behavior of the building in the cantilevered direction and not the coupled direction. Information regarding building geometry, material properties, section properties, reinforcement layout, seismic weight and dynamic characteristics of the building can be found in Section 2.2.

Figure 3.1a shows the plan view of the building archetype and Figure 3.1b describes the analytical nonlinear model in OpenSeesPy. The building is modeled in 2D and consists of three main parts (see Figure 3.1b) all fully supported at the foundation level: (1) RC pier, (2) leaning column, and (3) basement; a detailed description of the modeling approach of each component is provided in Sections 3.2.1, 3.2.2, and 3.2.3, respectively.

Due to symmetry of the structure in the cantilevered direction, only one of the two piers is modeled and half of the building weight is included in the model, as illustrated in Figure 3.1a. Note that this assumption reduces the runtime of the analyses without changing the dynamic properties of the building. The green rectangle in Figure 3.1a indicates the half of the building modeled in OpenSeesPy, and the areas surrounded by the blue and red lines show the tributary area of the RC pier and the leaning column, respectively. The building seismic weight is obtained from the load combination of $1.0D$+$0.5L$+$1.0E$ for nonlinear time-history analysis per PEER TBI (2017). This weight is lumped to the wall pier and the leaning column based on their tributary areas. Using this load combination to calculate the seismic mass, the periods and mode shapes of the first three modes of the archetype building are provided in **Table 3.1**. Note that these three modes achieve 90% modal mass participation.

Table 3.1. Modal analysis results.

Mode	Period (s)	Mode shape
1	3.98	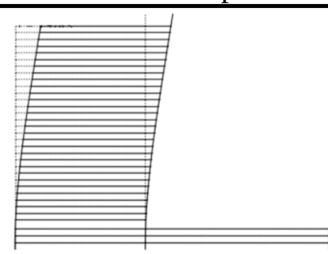
2	0.72	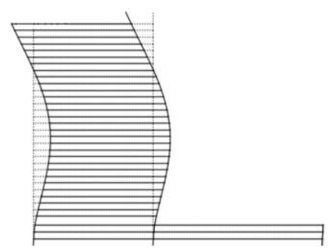
3	0.29	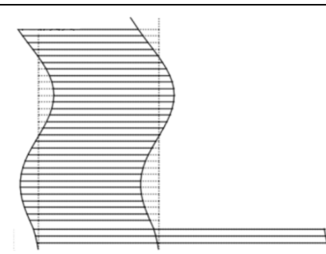

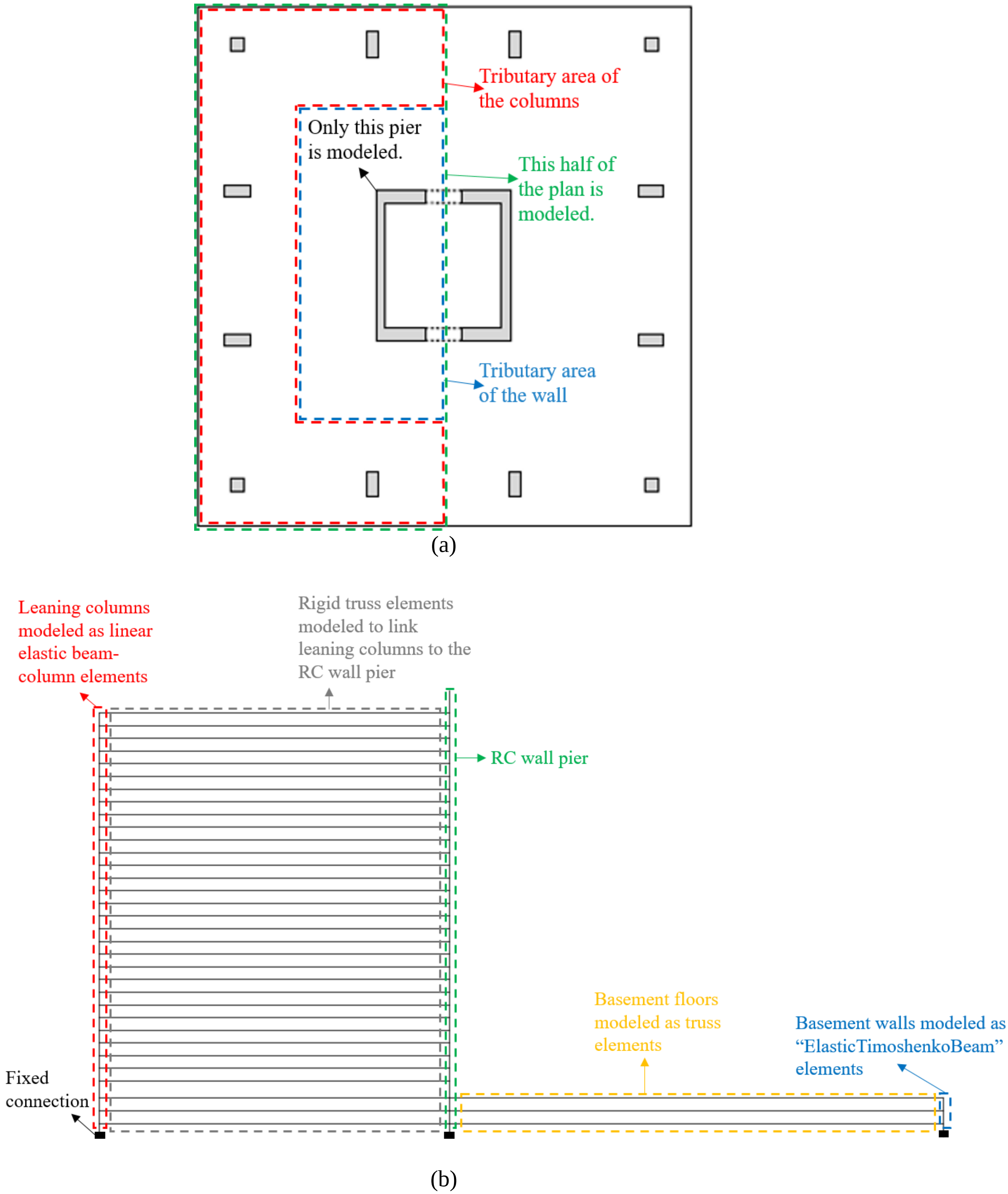

Figure 3.1. Schematic of the (a) building plan and tributary area of the walls and columns; (b) OpenSeesPy analytical model.

3.2.1 Reinforced Concrete Shear Wall Model

This study employed fiber-type beam column elements to model the RCSWs. Due to the high aspect ratio (i.e., height to length ratio) of these shear walls, it is expected that their flexural response will govern the overall behaviour of the building and therefore, this model is suitable. Nevertheless, because shear contributions to the response are not negligible (Pugh et al., 2015), shear contributions are also considered (see 3.2.1.3). The computational efficiency of fiber-type beam column elements compared to other elements such as layered shell elements and continuum elements provides additional motivation to use this modeling approach due to the large number of simulations required in this study.

Both Force-Based Element (FBE) and Displacement-Based Element (DBE) formulations (see Section 2.5) are available in OpenSees. This study uses the FBE approach to model the RC pier because it is less sensitive to the axial load variation through the length of the element (Pugh et al., 2015) and to the number of elements used per story. One limitation of the FBE formulation is that more convergence issues are observed when using this approach compared to the DBE approach. The approach followed to address this problem is discussed in section 3.2.6.

Pugh et al. (2015) showed that a high number of elements are required to reduce the axial load variation through the length of the element when the DBE approach is employed. A similar study is carried out here to evaluate the variation of axial force through the height of a wall modeled using the DBE approach. The results, provided in Figure 3.2, show that a high number of elements (on the order of 20 to 30) are required to limit the axial load error to 10%. Note that the flexural capacity of the wall is highly dependent on the axial load it is subjected to and therefore, unless a high number of elements are used with the DBE approach, the error in estimating flexural response of the wall is high.

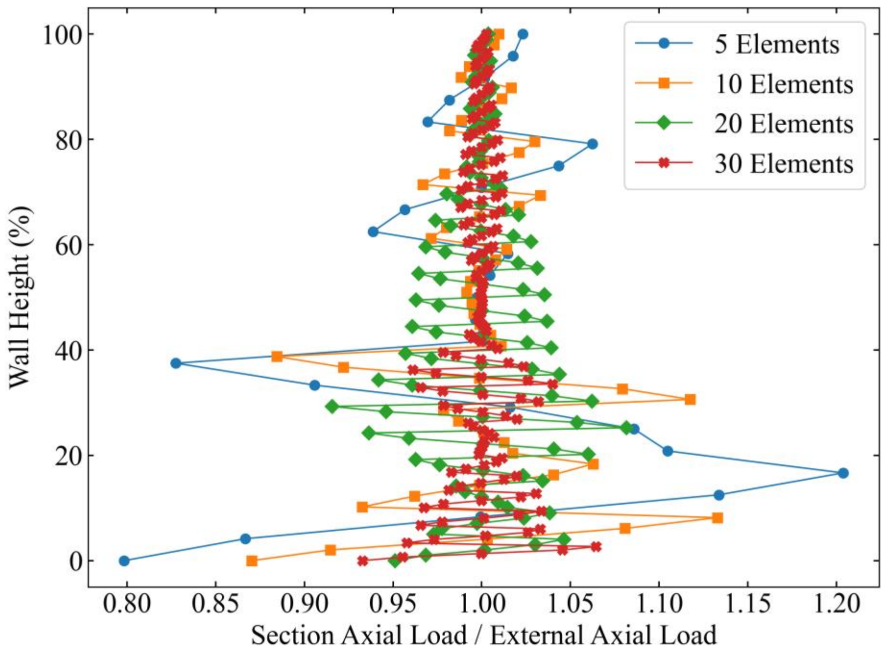

Figure 3.2. Variation in the axial force in different integration points along the height of the shear wall with different number of elements.

In this study, the RCSWs are modeled using only one force-based element per story with seven integration points. The Newton-Cotes beam integration approach is adopted in which integration points are uniformly distributed along the element with a point placed at each end of the element (Scott, 2011) and an intra-element tolerance of 1e-6 with a maximum of 1000 iterations is defined as suggested by (Pugh, 2012).

A fiber section is assigned to each integration point. The C-shaped shear wall section (see Figure 3.1a) is modeled as an I-shaped section discretized to confined and unconfined concrete, we well as steel fibers. The model assumes all fibers with the same distance from the neutral axis share the same strain when the section is subjected to uniaxial bending. For this reason, fiber discretization is only required along the direction perpendicular to the axis about which the section bends. While the analysis results are the same using both C- and I-shaped configurations, the latter is easier to implement in OpenSeesPy. Note that this approach has been followed in other studies (e.g. Marafi et al., 2019b). Both configurations of the wall fiber sections are shown in Figure 3.3. The red zones denote the boundary regions and steel bars are not shown for clarity.

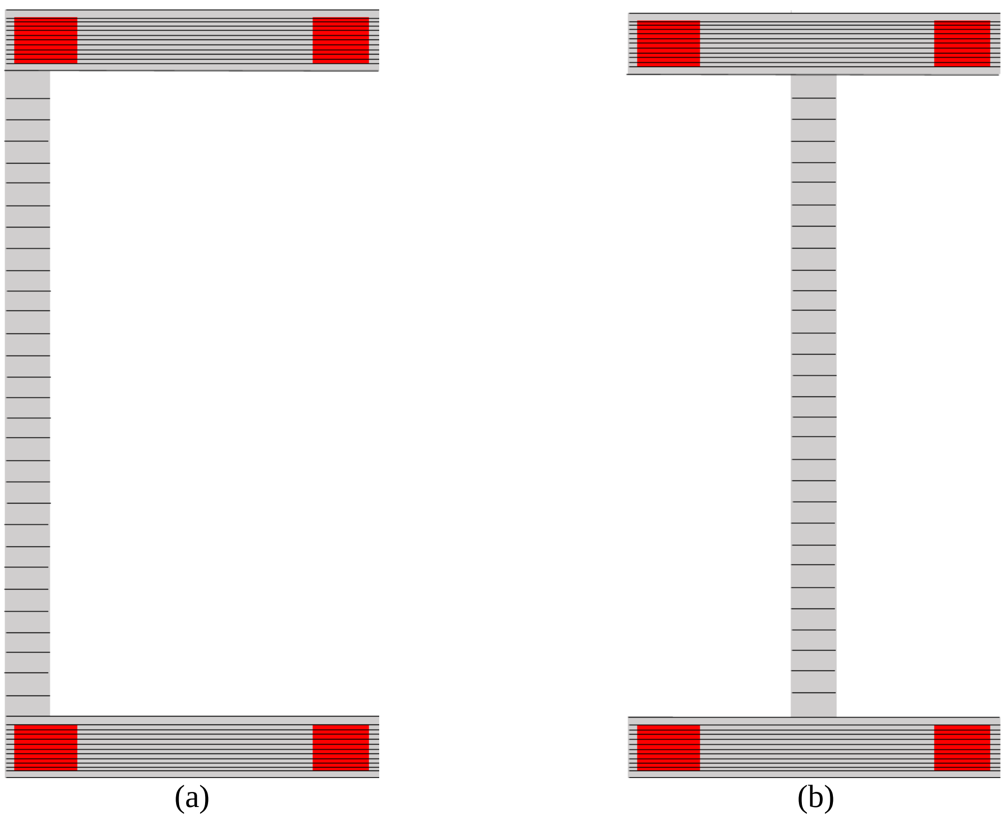

Figure 3.3. Possible configurations of the fiber-discretized wall sections of each cantilevered pier in the building model: (a) C-shaped configuration; (b) I-shaped configuration. The steel bars are not shown for clarity and the red zones are the boundary regions.

The discretization needs to be fine enough to capture proper variation of the strain throughout the wall section depth. Originally, the wall flanges and web are divided into 12 and 30 fibers, respectively (i.e., default number of fibers in Figure 3.4). To ensure enough fibers are used to discretize the section, the sensitivity of the moment-curvature response of the wall to the number of fibers is studied and the results are provided in Figure 3.4. The results suggest further discretization of the wall section does not change the analysis results. Therefore, in order to minimize the computational effort (without compromising the model accuracy), no further fiber discretization is considered. Note that a good value for the minimum number of fibers can be the number of distributed bars. In this study, the number of fibers are almost twice the number of distributed bars.

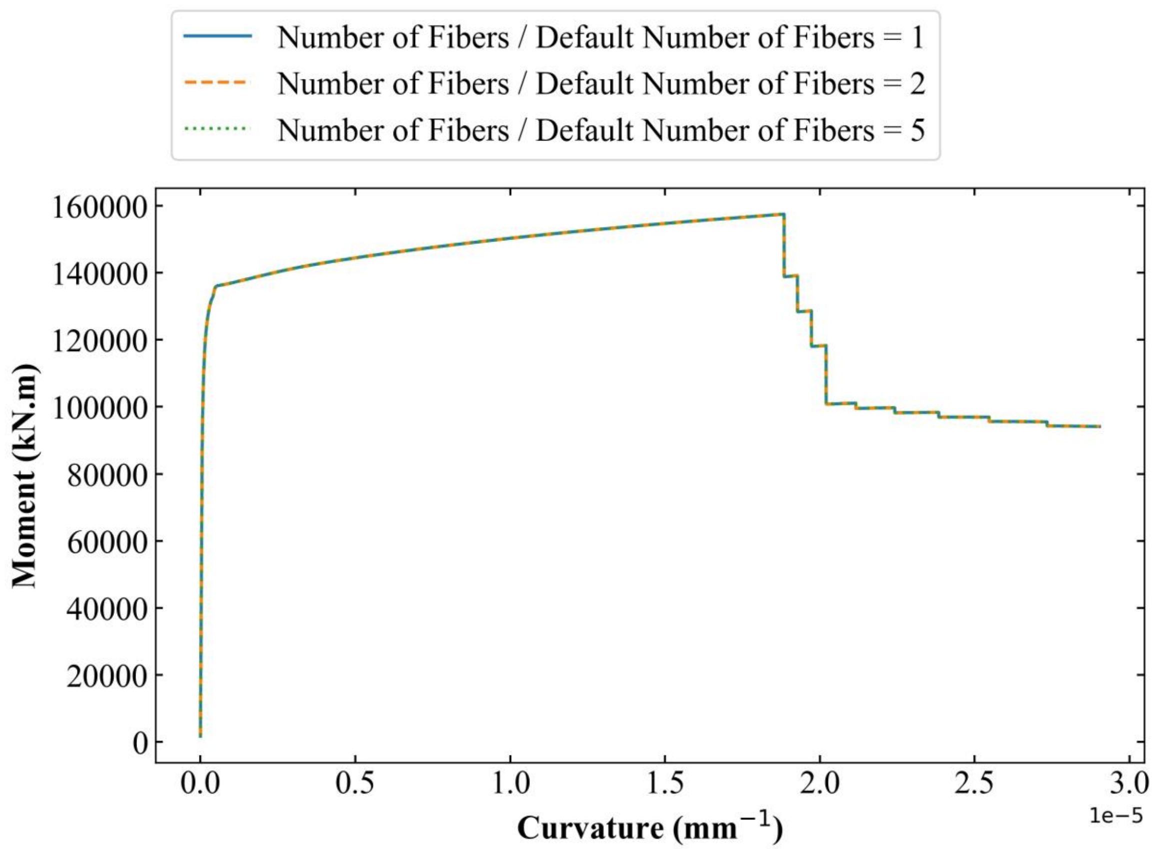

Figure 3.4. Sensitivity of moment-curvature response of the wall to the number of fibers. Default number of fibers refers to the case where 12 and 30 divisions are considered in each flange and web of the wall, respectively.

3.2.1.1 Constitutive Material Models

This section describes the concrete and steel constitutive material models used in the nonlinear structural analysis models.

3.2.1.1.1 Concrete Model

The "Concrete02" material in OpenSees is used to model the cyclic response of the confined and unconfined concrete fibers. This material model, proposed by Mohd Yassin (1994), is commonly used in the literature (e.g. Pugh et al., 2015; Marafi et al., 2019b). The stress strain relation of this material model is shown in Figure 3.5. The pre-peak response of the concrete is consistent with that proposed by Hognestad (1951), as shown in Figure 3.5 with an initial slope equal to the concrete elastic modulus, E_c. The strength degradation response is modeled as a linear function with negative slope initiating at the peak strength, f_p, and linearly degrading until reaching the residual strength, f_{res}. The tensile response is modeled with a linear elastic response with a slope equal to E_c for strains up to the cracking strain, ε_{cr}, followed by a strength-degradation segment at higher strains with a negative slope equal to E_t until reaching a residual tensile strength set to zero. The reloading and unloading paths are linear in the tensile envelope. The reloading path in the compression envelope is linear. However, the unloading path in the compression envelope is bilinear as described in Mohd Yassin (1994).

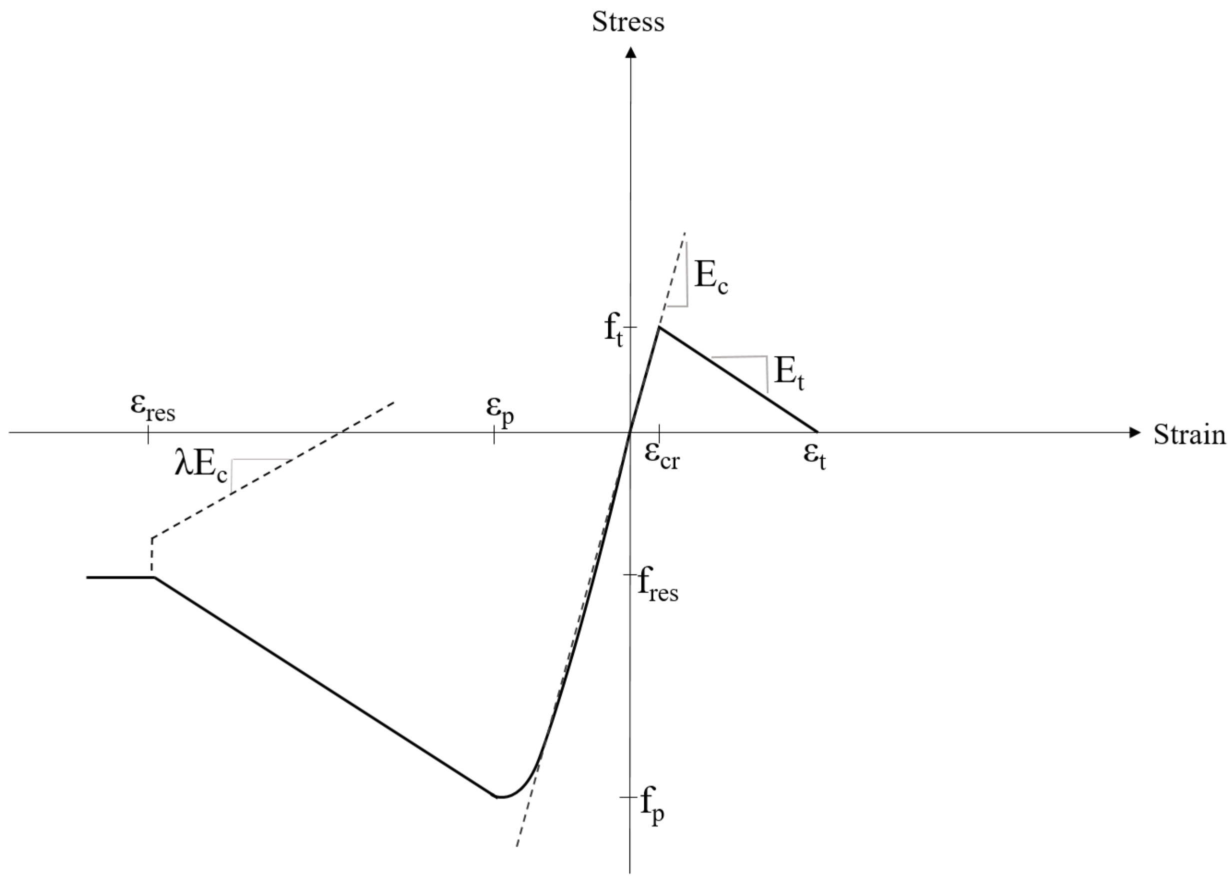

Figure 3.5. Stress-strain relation of the Concrete02 material in OpenSees (Mohd Yassin, 1994).

The peak concrete strength, f_p, is set equal to the concrete material expected strength, 1.3 f'_c per PEER TBI (2017). The modulus of elasticity, E_c, is obtained from ACI 318 (2014) using Eq. 3.1.

$$E_c = 4700\sqrt{f_p}\,(\text{MPa}) \tag{3.1}$$

The strain at the peak strength point, ε_p, is obtained using Eq. 3.2 (Mohd Yassin, 1994). The concrete crushing strength, f_{res}, is set equal to 0.2 f_p and the residual strain, ε_{res}, is set equal to 0.008 as suggested by Pugh et al. (2015).

$$\varepsilon_p = \frac{2 f_p}{E_c} \tag{3.2}$$

The concrete tensile strength, f_t, is obtained using Eq. 3.3 (Wong et al., 2013). Moreover, the cracking strain, ε_{cr}, and the ultimate tensile strain, ε_t, can be obtained from Eq. 3.4 and Eq. 3.5 as outlined in Massicotte et al. (1990).

$$f_t = 0.33\sqrt{f_p}\,(\text{MPa}) \tag{3.3}$$

$$\varepsilon_{cr} = \frac{f_t}{E_c} \tag{3.4}$$

$$\varepsilon_t = 16\varepsilon_{cr} \tag{3.5}$$

In the Concrete02 material, λ is the ratio of the unloading slope at the crushing point to the initial slope and is taken as 0.1. Also, the tensile softening stiffness of the concrete, E_t, is equal to 0.05 E_c as outlined in Mohd Yassin (1994).

The confined concrete maximum compressive strength, f_{pc}, and residual strain, $\varepsilon_{res\text{-}c}$, are determined using the Saatcioglu & Razvi (1992) model. The tensile response of the confined concrete is the same as that of unconfined concrete. Confined concrete modulus of elasticity, E_{cc}, is same as that of the unconfined concrete. Eq. 3.2 is used to obtain the strain at the point of maximum compressive strength in the confined concrete, ε_{pc}, by setting f_p to f_{pc}. Also, ε_{res} and f_{res} in Figure 3.5 are set to $\varepsilon_{res\text{-}c}$ and 0.2 f_{pc}, respectively and λ is also equal to 0.1 for the confined concrete.

3.2.1.1.2 Steel Model

The "Steel02" material model in OpenSees (Filippou et al., 1983) is common in the literature, and thus, is adopted in this study to model the cyclic response of the steel reinforcement in the walls.

This model employs a bilinear stress-strain envelope and the Giuffre-Menegotto-Pinto (Menegotto & Pinto, 1973) unload-reload paths. This model is capable of simulating the Bauschinger effect in the cyclic response of the steel. The stress-strain relation of the Steel02 model is shown in Figure 3.6.

The yield strength, f_y, is set to the expected strength of the steel material, which is set to 1.17 times the nominal steel strength per PEER TBI (2017) recommendations. The modulus of elasticity, E_s, is set equal to 200GPa. The strain-hardening stiffness ratio, b, is the ratio of the post yield stiffness to the initial elastic stiffness of the steel stress-strain curve. This value can be obtained from Eq. 3.6.

$$b = \frac{f_u - f_y}{(\varepsilon_u - \varepsilon_y)E_s} \tag{3.6}$$

where ε_y, f_u, and ε_u are the yield strain, ultimate strength, and rupture strain of the steel material. The value of ε_y is equal to f_y/E_s, and the values of f_u, and ε_u are obtained from the reported material properties. The value of the strain hardening stiffness ratio is usually between 0.5-5%. R_0 determines the initial value of the curvature parameter, R, which characterizes the Bauschinger effect. The curvature degradation parameters, $cR1$ and $cR2$, the isotropic strain hardening in compression parameters, $a1$ and $a2$, and the isotropic strain hardening in tension parameters, $a3$ and $a4$, are all set to the default values.

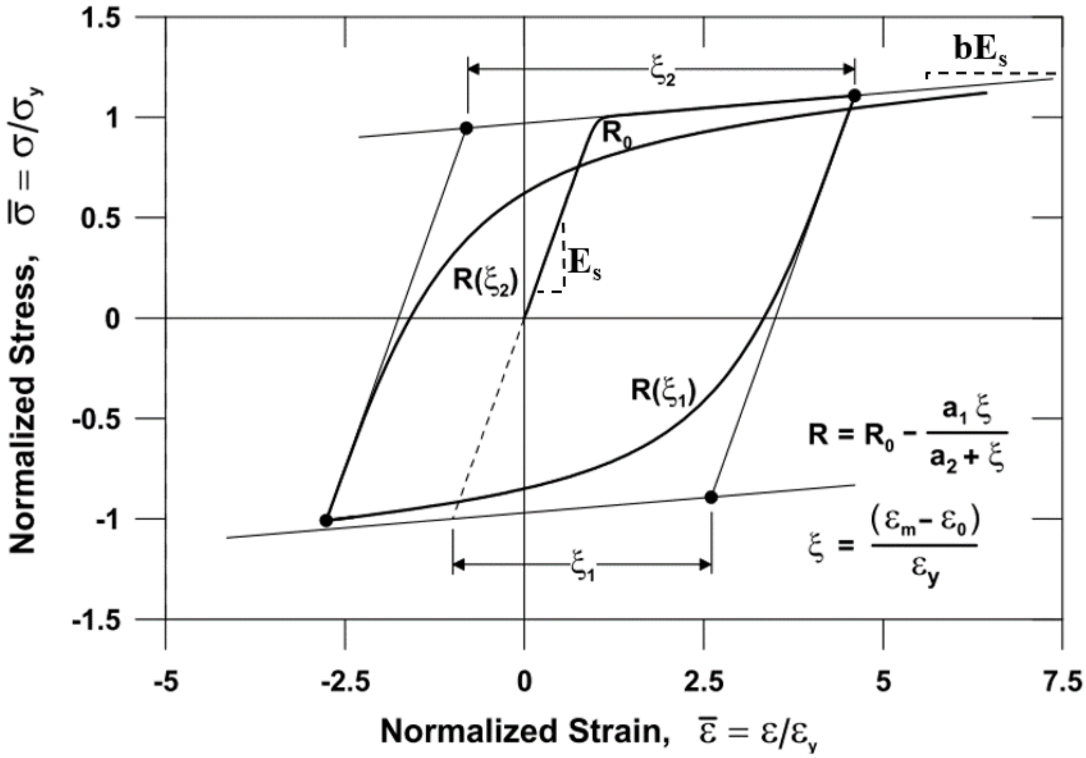

Figure 3.6. Steel material model stress-strain relation (Menegotto & Pinto, 1973).

The Steel02 material model can be modified to capture steel rupture and buckling by leveraging the “MinMax” material model in OpenSees. The steel rupture condition is provided by the max strain value of “MinMax” set equal to ε_u = 0.13, which is the fracture strain in steel. Buckling is captured by setting the min strain value of “MinMax” equal to eε_{res}, the concrete crushing strain that triggers rebar bucking.

3.2.1.2 Material Regularization

As described in Section 2.5, material regularization is needed to prevent damage localization in the RCSWs with a softening response when modeled using fiber-type beam column elements. Section analysis is carried out for each pier at the grade level, where the plastic hinge is anticipated to form, to determine if the wall has a softening response under the expected axial load. The results of the section analysis on these shear walls exhibit a hardening response prior to failure due to steel rupture, as shown in Figure 3.7; therefore, material regularization is not required in this study. Note that the walls would exhibit a softening response given one of the following cases: (1) lower concrete strength, (2) lower longitudinal reinforcement ratio, and (3) higher axial load demand.

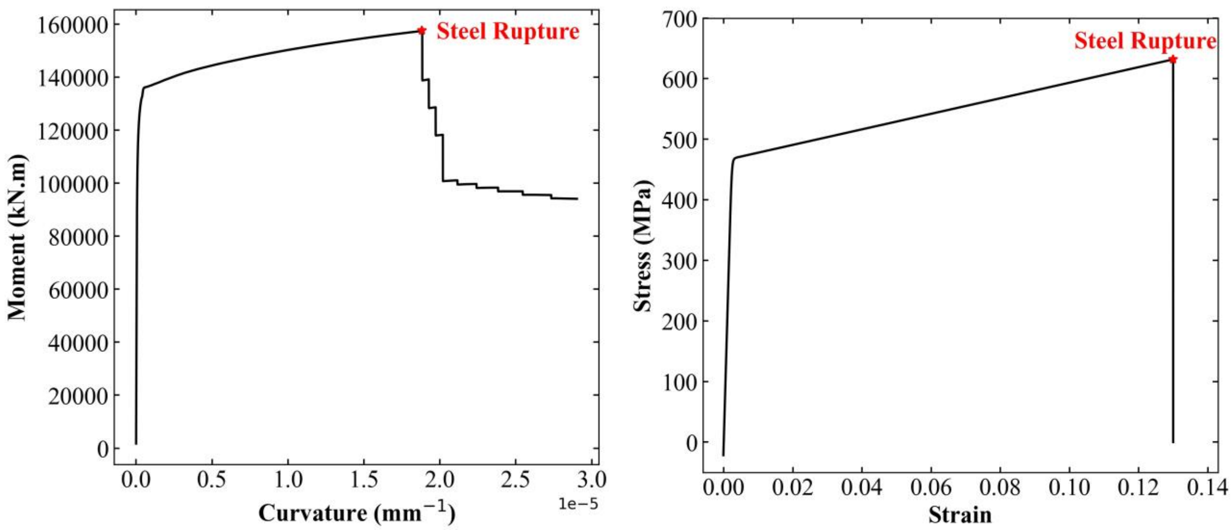

(a) (b)

Figure 3.7. Sectional analysis results of each cantilevered pier at the grade level of the building: (a) Moment-curvature response; (b) extreme tension steel fiber.

3.2.1.3 Shear Response

To account for shear response of the RCSWs in this study, an approach similar to Pugh et al. (2015) is followed. Shear response is aggregated with the axial-flexural response using the "Section Aggregator" command in OpenSeesPy (see Figure 3.8). The shear force, V is equal to $C_{GA}\,G\,A_v\,\gamma$ where C_{GA}, G, A_v, and γ are the shear stiffness reduction factor, the concrete shear modulus, the wall effective shear area, and the shear strain, respectively. G is estimated as $0.4E_c$ per ATC 72-1 (2010), and the effective area for a rectangular section is $5/6A_g$ where A_g is the gross area of the shear wall. Note that only the web of the C-shaped shear wall of the building archetype (Section 2.2) is considered in calculating the effective shear area. In this study, a C_{GA} of 10% is used when calibrating analytical models against experimental test data per the recommendations of Pugh

(2012). However, the shear stiffness modifier used in the building model for nonlinear time-history analyses is 50% for consistency with PEER TBI (2017) recommendations. The shear wall response is less sensitive to the shear stiffness modifier in the building model than the calibration model due to the high aspect ratio of the shear wall.

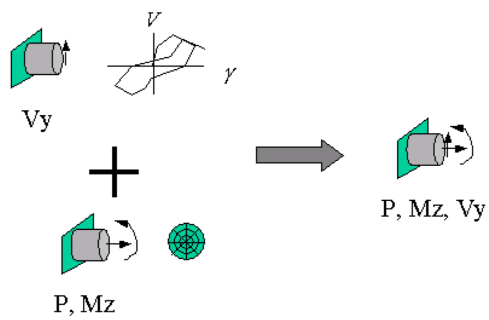

Figure 3.8. Section aggregator command in OpenSees (OpenSeesWiki, 2016).

3.2.1.4 Nonlinear Model Validation

To validate the proposed nonlinear model and calibrate the model parameters, the cyclic response of specimen RW-A20-P10-S38, as tested by Tran & Wallace (2015), is simulated under the same load and displacement protocols. Both DBE and FBE approaches are used to calibrate the model parameters. The results suggest that both approaches are capable of simulating the cyclic response of the sample shear wall specimen. A single element with five integration points is used to calibrate the shear wall with the FBE approach. Five elements with five integration points are utilized to calibrate the shear wall with the DBE approach. In order to obtain the best match between the analytical and experimental results, a modulus of elasticity equal to $0.8E_c$ is used in the calibration. This assumption is within the acceptable range outlined in ACI 318 (2014): “Measured elastic modulus values can range from 80 to 120 percent of calculated values”. A steel strain-hardening stiffness ratio of 0.6% resulted in a good agreement between the experimental and analytical results. Also, the *R*0 parameter in the Steel02 material, which controls the transition from elastic to plastic branches, is set to 12.95 and 10 in the FBE and DBE model, respectively. These values fall within the recommended range of 10 to 20. Other Steel02 model parameters (*cR*1, *cR*2, *a*1, *a*2, *a*3, and *a*4) are set to the default values. The analytical and experimental hysteretic responses of the specimen are shown in Figure 3.9. Note that while the proposed model is capable of capturing the stiffness during loading and unloading, as well as the wall strength up to a lateral drift of 3%, it fails to capture the cyclic strength degradation observed after the second 3% drift loading cycle. Note that this is not an issue in this study because the shear walls of the building archetypes will be subjected to lateral drifts below 3% and have a hardening response as discussed in Section 3.2.1.2. As shown later in Chapter 5, for the nonlinear time-history analyses performed in this study, the concrete strain is less than ε_p and thus, strength degradation is not expected in the hysteretic response of the walls.

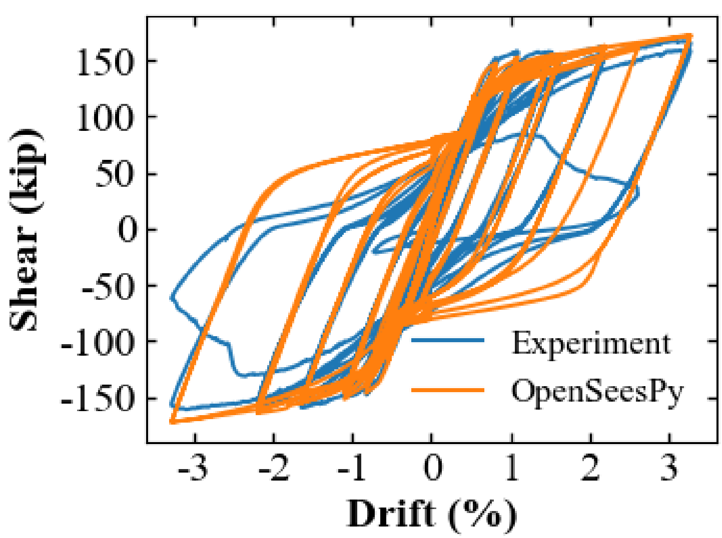

Figure 3.9. Shear wall calibration results.

3.2.2 P-Delta Effects

P-Delta effects are accounted for by means of a leaning column. Leaning columns are modeled as elastic beam column elements with high axial stiffness connected to the SFRS using axially rigid truss elements. An easy way to demonstrate the leaning column mechanism is through the Yura approach (Yura, 1971) schematically described in Figure 3.10. As shown in the figure, a lateral shear wall displacement of Δ, results in the same lateral displacement of the leaning columns because of the axially rigid truss connection. Equilibrium in column CD requires forming an axial force of $Q\Delta/L$ in the truss element which is transferred to the shear wall and causes an additional moment of $Q\Delta$ at the base of the wall (Geschwindner, 2002).

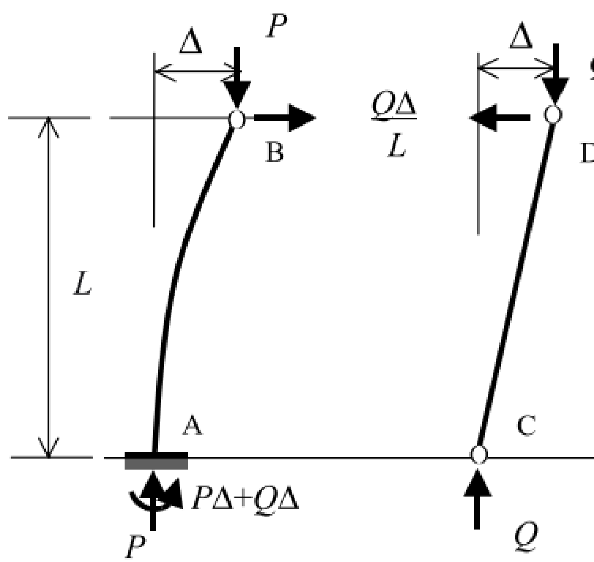

Figure 3.10. Equilibrium force for Yura derivation (Geschwindner, 2002).

Leaning columns should not contribute to the flexural resistance of the building; this can be satisfied either by modeling rotational springs with low stiffness at the ends of the leaning columns or by considering a low bending rigidity for the leaning columns. Both approaches lead to the same analysis results, however, the latter is easier to implement in OpenSeesPy, and therefore used in this study. The leaning column axial load can be obtained by subtracting the wall axial load from the total gravity load at each story in the building.

3.2.3 Basement Model

A similar approach to that of Marafi et al. (2019b) is used to model the basement structure (retaining walls and floor diaphragms). These elements are modeled using elastic springs with stiffness values obtained from a 3D finite element model in the commercial structural analysis software, ETABS. The basement retaining walls are modeled using the "ElasticTimoshenkoBeam" element in OpenSeesPy where shear deformations are accounted for. The bending and shear stiffness values of the shear wall are equal to $0.8E_cI_g$ and $0.2E_cA_g$ as per PEER TBI (2017) recommendations. The basement floors are modeled using truss elements with a modified axial stiffness of $0.25E_cA_g$, also per PEER TBI (2017) recommendations.

While this simplified model permits capturing the backstay effect, it is unable to capture the true behavior of the basement floors and walls. A sensitivity study was carried out to investigate the effects of basement walls and floors stiffness assumptions on the response of the structure above and below the grade. The building archetype is subjected to a simulated ground motion of M9 CSZ earthquake in Delta (described later in Chapter 4) and the maximum story shear is recorded for different values of basement diaphragm and walls stiffness. The results are shown in Figure 3.11 where the basement diaphragm or wall stiffness ratio is the ratio of the basement diaphragm or wall stiffness in OpenSeesPy to the basement diaphragm or wall stiffness obtained from ETABS. Figure 3.11 shows that the structural response above the grade is not significantly affected by changing the basement walls and floors stiffness assumptions, which primarily influence the response below grade. These results are consistent with the observations by Moehle (2015). Furthermore, because the focus of this study is on evaluating the superstructure, this modeling approach is deemed acceptable.

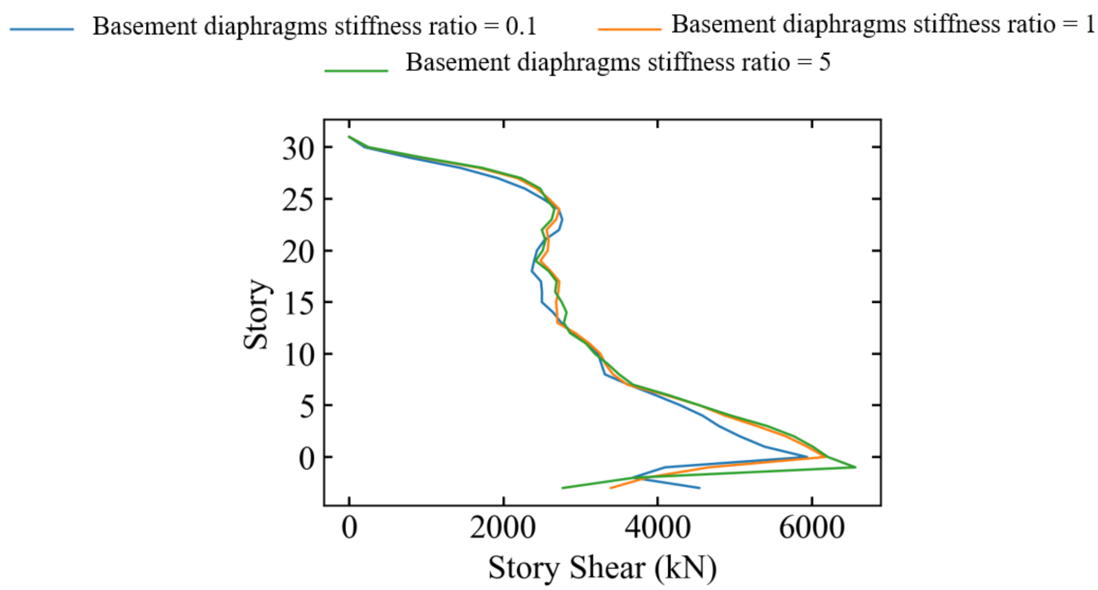

(a)

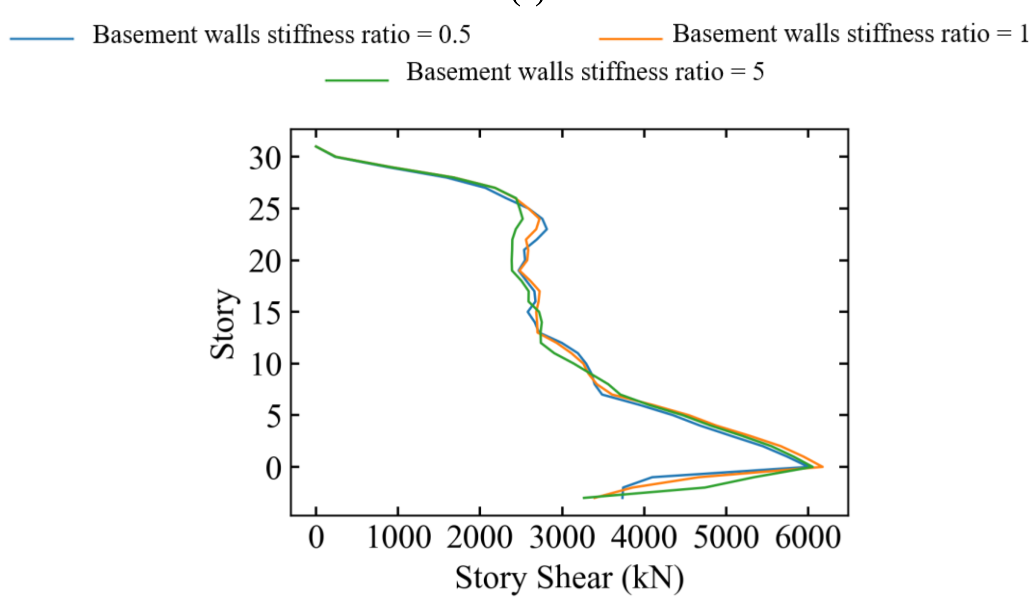

(b)

Figure 3.11. Story shear for different values of (a) basement diaphragm stiffness; and (b) basement wall stiffness under a simulated ground motion of M9 CSZ earthquake in Delta. Note that the default basement stiffness is used in this study for nonlinear time-history analysis.

3.2.4 Damping Assumptions

2.5% equivalent viscous damping is applied through the Rayleigh damping model. As suggested in ATC-72-1 (2010), mass proportional damping underestimates damping of higher modes, while the stiffness proportional damping results in excessive higher mode damping. Therefore, both mass and stiffness proportional damping are considered in the Rayleigh model. Due to the changes in the periods of a structure during a nonlinear analysis, the updated tangent stiffness matrix is considered in the Rayleigh damping model, while the mass and stiffness coefficients are constant (Petrini et al., 2008). Consistent with Marafi et al. (2019b), this study uses the first and second periods of the structure to obtain the Rayleigh mass and stiffness coefficients. The percent of critical damping is plotted for mass, stiffness, and Rayleigh proportional damping at different periods in Figure 3.12.

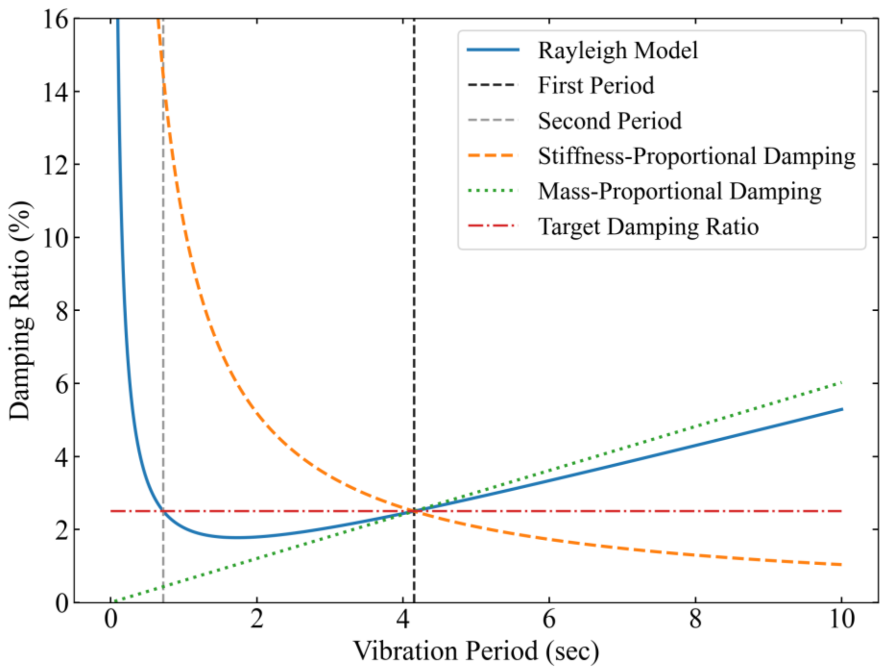

Figure 3.12. Percent of critical damping at different periods for mass, stiffness, and Rayleigh proportional damping.

3.2.5 Analysis Settings

The analysis settings used to conduct time-history analysis in OpenSeesPy are described in this section. The required objects are “ConstraintHandler”, “DOF_Numberer”, “Integrator”, “SolutionAlgorithm”, “Solver”, and “Convergence Test”. The definition of each analysis object can be found in the OpenSeesWiki (2016). The analysis objects used in this study are explained below.

The ConstraintHandler object determines the way the constraint equations are enforced in the analysis. A “Plain Handler” is not an appropriate constraint handler for the building archetypes as it only enforces single-point constraints (such as pin or fixed boundary conditions). In this study, some of the nodes in the nonlinear model of the building archetype are involved in more than one constraint. Therefore, the “Transformation” constraint handler is used. This constraint handler object does not work properly if a node is involved as a retained node in one constraint and as the constrained node in another (OpenSeesWiki, 2016). This constraint handler method is preferred to the “Penalty” and “Lagrange” methods because choosing the proper penalty numbers and Lagrange multipliers requires care. In addition, some solvers do not work with the “Penalty” and “Lagrange” methods (Scott, 2020).

The convergence criterion can be set using the convergence test object. The “NormDispIncr” convergence test is used as convergence criterion with a global solution tolerance of 1e-6 and maximum of 1000 iterations. Use of the “NormUnbalance” test object, an alternate convergence test object, is not advised in this study due to the existence of stiff elements in the model.

The “KrylovNewton” algorithm was found to be helpful in solving convergence issues. The solver object in OpenSeesPy determines how to store and solve the system of equations in the analysis within the solution algorithm and the DOF_Numberer determines the mapping between equation numbers and degrees of freedom (OpenSeesWiki, 2016). The “UmfPack” solver in OpenSees is used with the “RMC” numberer. The Integrator object is required to determine the predictive step for time t+dt (OpenSeesWiki, 2016). The “Newmark” integrator object is used with γ and β values equal to 0.5 and 0.25, respectively.

3.2.6 Solving Convergence Issues

Convergence issues are often observed in OpenSeesPy analyses and they are associated with modeling assumptions or analysis settings. To achieve convergence, it is recommended to first revisit the analysis settings (Scott, 2019). Increasing the number of iterations in the test object and changing the algorithm to “KrylovNewton” were found to be useful in this study. However, decreasing the time step in the time-history analysis is the most effective strategy to minimize convergence problems. In this study, each time-history analysis begins with an analysis time step equal to the ground motion time step; if convergence is not achieved, the analysis time step is reduced to 0.1, 0.02, or 0.002 times the default time step, which varies from record-to-record from 0.02 to 0.0029 seconds.

In this study, sensitivity studies are carried out on different material model parameters and modeling assumptions to identify which parameters or assumptions cause non-convergence. Another helpful strategy leveraged in this study is starting from a linear model and introducing nonlinearity incrementally until the building structure is fully nonlinear. Whenever convergence issues are identified in this procedure, the last modification was identified as a possible cause for non-convergence. This has helped in this study with choosing material models which are numerically more robust.

Chapter 4: Seismic Hazard and Ground Motion Selection

This chapter provides an overview of different approaches to assess the seismic performance of buildings. Section 4.1 describes different types of seismic performance assessments defined by FEMA P-58 (FEMA, 2018) and an overview of the assessments used in this study. Sections 4.2 and 4.3 provide details of ground motion selection and scaling procedures employed.

4.1 Scenario and Intensity-Based Seismic Performance Assessments

As described in Sections 2.4 and 2.6, intensity- and scenario-based assessments are performed in this study for the purpose of loss and downtime evaluation. The intensity-based performance assessment is leveraged to evaluate performance of the archetype buildings under four different shaking intensities with 2%, 5%, 10%, and 40% probabilities of exceedance in 50 years (i.e., return periods of 2475, 975, 475, and 100 years, respectively). These shaking intensities are referred to as the 2475-year, 975-year, 475-year, and 100-year hazard levels hereinafter. Ground motion selection and scaling is done per Commentary J of NBC 2015 (Canadian Commission on Building and Fire Codes, 2017) where all three dominant seismic sources in southwestern British Columbia (i.e., shallow crustal, subduction intraslab, and subduction interface earthquakes) are considered in the assessment. As the Georgia sedimentary basin effects are not accounted for in 2015 NSHM (Adams et al., 2015), which is used to determine the hazard in the intensity-based assessments, the basin amplifications are not explicitly considered in this type of assessment.

The scenario-based assessment is carried out by subjecting the archetype building models to simulated ground motions of M9 CSZ earthquakes generated by Frankel et al. (2018), which explicitly account for the effects of the Georgia sedimentary basin. These motions have an approximate return period of 500 years (Atwater & Hemphill-Haley, 1997) and are of more concern due to their high spectral accelerations at long periods, attributed to the amplification effects of the Georgia basin, and the resulting impacts on tall buildings. More details are provided in Sections 2.3 and 2.4.

4.2 NBC 2015 Ground Motions

As mentioned previously, four hazard levels are considered in the intensity-based assessments. The scaling procedure described in this section is the same for all shaking intensities. For each of the three major seismic sources near Metro Vancouver (i.e., shallow crustal, subduction intraslab, and subduction interface earthquakes), the ground motions are selected with magnitudes and distances similar to the dominant range of magnitudes and distances that control the seismic hazard of the region. The exceptions are a few intraslab and interface motions due to the limited number of available records. In this study, 11 seismic events are considered for each source to meet the criteria of Commentary J of NBC 2015. The databases of ground motion records are summarized in Table 4.1. The spectral shapes of the selected motions are similar to those of the target response spectrum over the period ranges of interest.

Table 4.1. Ground motion records database.

Source	Database
Crustal	PEER NGA-West2 (Ancheta et al., 2014)
Subduction-Intraslab	NGA-Subduction (Ahdi et al., 2017) and S2GM (Bebamzadeh et al., 2015)
Subduction-Interface	K-NET and Kik-net (Aoi et al., 2004) and S2GM (Bebamzadeh et al., 2015)

As mentioned in Section 2.4, the NBC 2015 design response spectra at all the locations considered are fairly similar. However, because of the slight variations in response spectral accelerations, the envelope of the uniform hazard spectra is used as the target spectrum for selecting and scaling ground motions.

According to Commentary J of NBC 2015, the lower-bound and upper-bound periods, $T_{\min}$, and $T_{\max}$, that defined the period range of interest can be obtained from Eq. 4.1 and Eq. 4.2.

$$T_{\min} = \min(0.1T_1, T_{90\%}) \tag{4.1}$$

$$T_{\max} = \max(2T_1, 1.5s) \tag{4.2}$$

In Eq. 4.1, T_1 is the fundamental period of the structure, and $T_{90\%}$, represents the minimum period required to achieve 90% modal mass participation. Modal analysis is performed on the structural model used for the time history analysis, and the resultant periods are used to calculate the period range for ground motion selection and scaling. The lower-limit, $T_{\min}$, and upper-limit, $T_{\max}$, are 0.29 and 7.91 seconds, respectively. Due to the contribution of different seismic sources to the hazard in the locations of interest, a scenario-specific period range, T_{RS}, is also defined for each source. The scenario-specific period ranges are specified in Table 4.2 for each seismic source. Note that for the interface source, the upper-limit period is set equal to $T_{\max}$.

Table 4.2. Scenario-specific period range.

Seismic Source	T_{RS} **(s)**
Crustal	[0.2, 0.8]
Intraslab	[0.3, 1.5]
Interface	[1, 7.91]

Commentary J of NBC 2015 requires two different steps in the ground motion scaling procedure. First, each motion should be scaled individually such that, on average, its response spectrum equals or exceeds the target response spectrum over the scenario-specific period range. This is done by minimizing the mean squared difference of the spectral accelerations over the appropriate scenario-specific period range. Next, the mean response spectrum of the suite must fall above 90% of the target response spectrum at each period over the period range of interest. Figure 4.1 demonstrates the ground motions response spectra scaled to the design target spectrum (i.e., 2% in 50 years response spectrum) per Commentary J of NBC 2015.

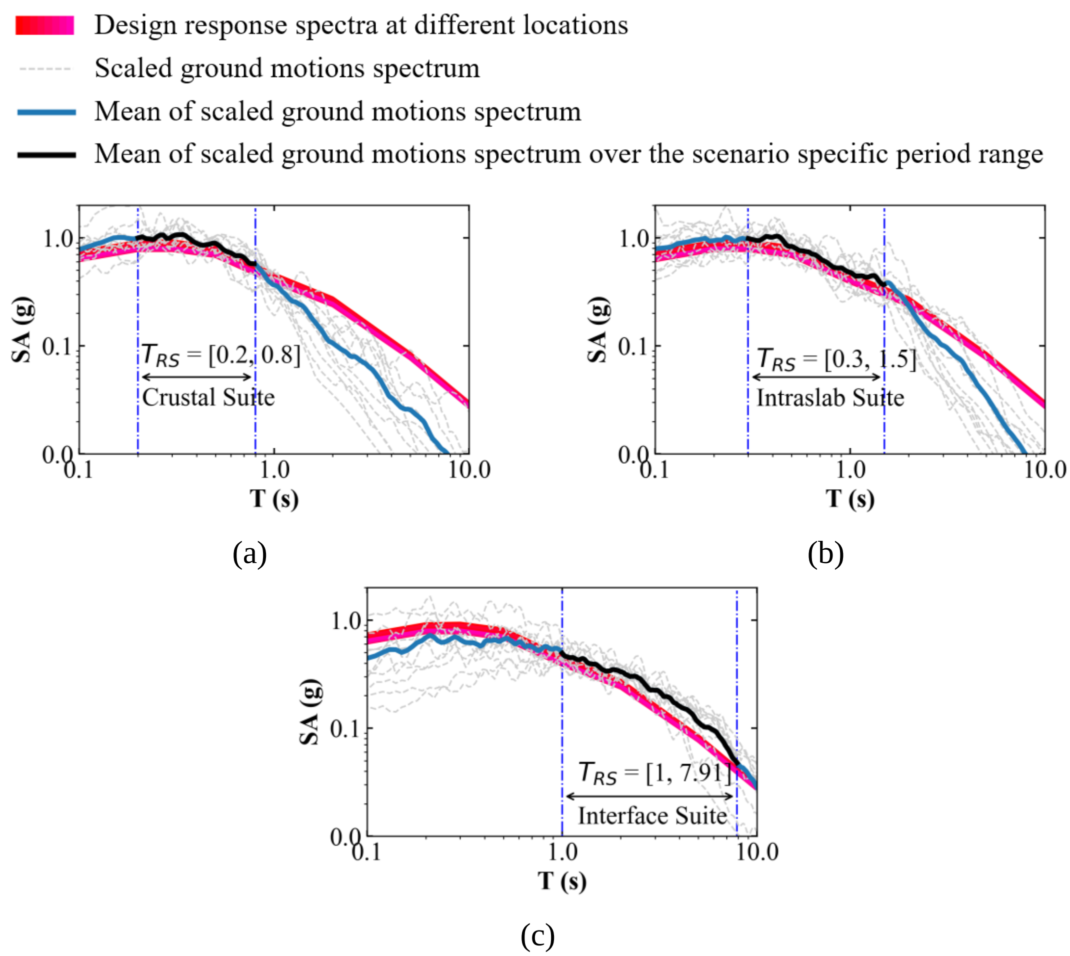

Figure 4.1. 10% in 50-year target spectra, individual ground motions spectra, and average spectra for seismic sources: (a) Crustal, (b) Intraslab, (c) Interface.

4.3 Simulated M9 CSZ Earthquake Ground Motions

For the purpose of the scenario-based assessments, 30 pairs of simulated ground motions of M9 CSZ earthquakes produced by Frankel et al. (2018) are used in the analysis. Since each pair has two components, 60 motions in total are applied to the 2D analysis models used in this study. The response spectrum of each of the 60 components is compared with the NBC 2015 2% in 50 years design spectrum at the eight locations of interest across Metro Vancouver, as shown in Figure 4.2. Although the M9 motions have a much lower return period than that of the design earthquake (i.e., 500 vs 2475 years), the mean response spectrum of the M9 motions lies above the design response spectrum at long periods in deeper basin sites (i.e., basin sites with a higher depth to shear wave velocity of 2.5 km/s) as indicated in Figure 4.2.

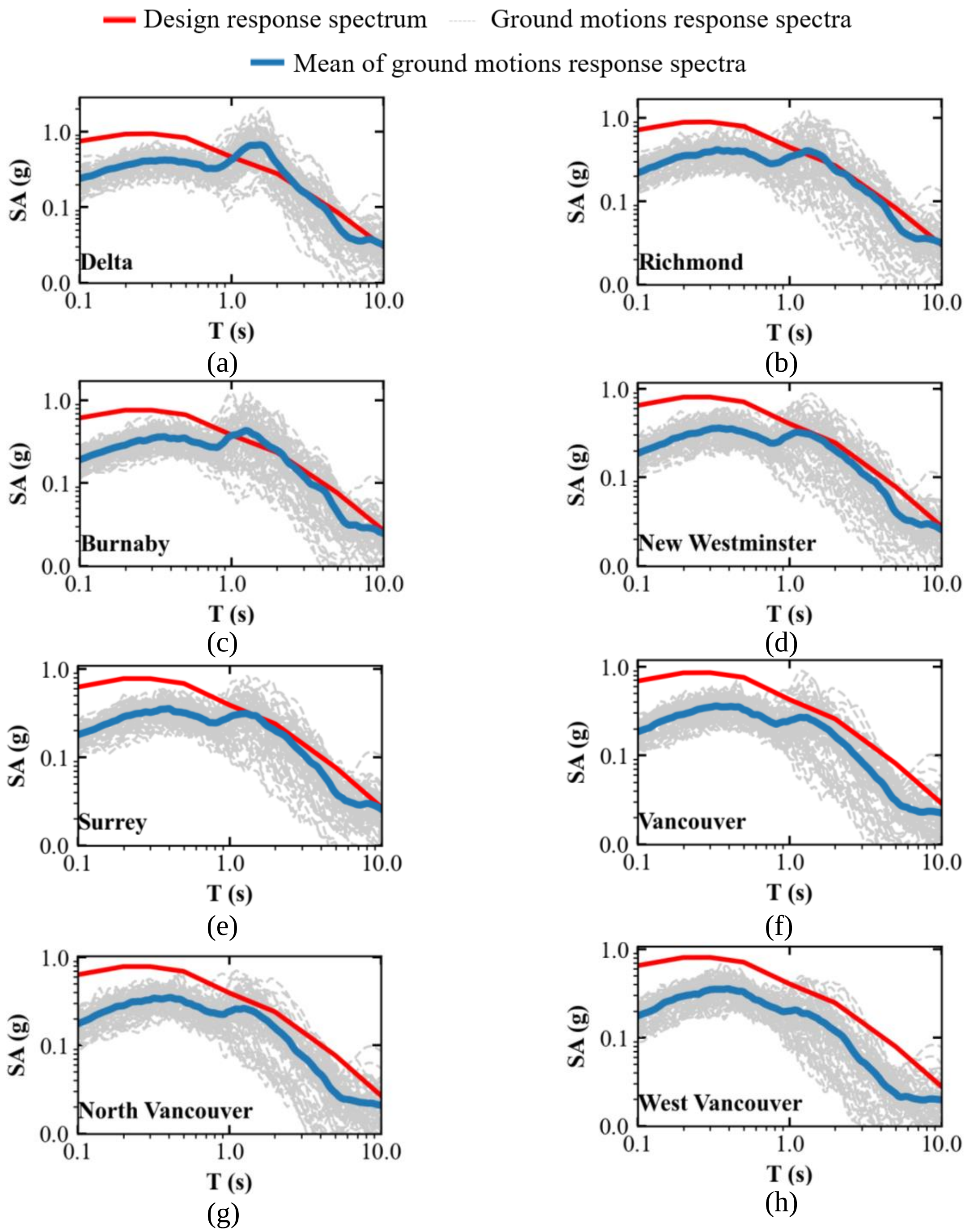

Figure 4.2. Design target spectrum, individual ground motions spectra, and average spectra for M9 motions in the locations of interest across Metro Vancouver area: (a) Delta; (b) Richmond; (c) Burnaby; (d) Surrey; (e) New Westminster; (f) Vancouver; (g) North Vancouver; (h) West Vancouver.

Chapter 5: Nonlinear Simulation of Structural Response

This chapter presents the results of the nonlinear time-history analysis performed on the archetypical RCSW buildings for both intensity- and scenario-based assessments. The sensitivity of the structural responses to different hazard levels and basin depths are investigated, and the significance of the Georgia sedimentary basin effects on seismic response of the building archetypes is highlighted by comparing the seismic demands associated with the intensity- and scenario-based assessments.

Four intensity levels are considered with return periods of 100, 475, 975, and 2475 years (2015 NSHM motions). The structural analysis results associated with the intensity-based assessment are provided for each seismic source (i.e., crustal, subduction interface, and subduction intraslab) separately. In order to check whether the code-prescriptive design also complies with PEER TBI (2017) requirements for performance-based design of tall buildings, as demonstrated by Eksir Monfared et al. (2021), the 100-year intensity level is used to check PEER TBI serviceability limits, and the 2475-year intensity-level is used to check the Maximum Considered Earthquake (MCE_R) requirements. The scenario-based assessment is conducted using the simulated ground motions of M9 CSZ earthquakes at eight critical locations across Metro Vancouver.

While all nonlinear time-history analysis simulations required for the intensity-based assessment converged, simulated and non-simulated collapse cases were observed at some locations in the M9 simulations. The structural responses associated with such motions are not provided in this section nor are they included in mean structural response calculations.

5.1 Story Drift Ratio

5.1.1 Transient Drift Ratio

Figure 5.1 represents the transient drift ratios at all locations obtained from the scenario-based assessments and compared with the average results of the three suites of 2475-, 975-, 475-, and 100-year motions. It is evident in Figure 5.1 that transient drift ratios are higher in sites with deeper basins. The highest transient drift ratios are observed in Delta, Richmond, and Burnaby, respectively. The results in Surrey and New Westminster are almost the same (they have a similar $Z_{2.5}$ value) and the lowest responses are observed in West Vancouver, which is located outside the basin. The transient drift ratios in Delta, the deepest basin site, exceeds those of the 2475-year motions.

As per PEER TBI (2017), in each story, the absolute value of the mean peak transient story drift ratio from each suite or set of analyses should not exceed 3%, and each analysis with a peak transient story drift ratio greater than 4.5% is an unacceptable response. Figure 5.2 represents the mean transient drift ratios of the four hazard levels considered in the intensity-based assessment. As shown in Figure 5.2a, in 2475-year motions, the average transient drift ratios associated with each seismic source are well below the 3% threshold specified in PEER TBI (2017) and the individual motions have transient drift ratios well below 4.5%; so, the transient drift ratios meet the requirements of PEER TBI (2017) for the MCE_R evaluation. Similarly, the mean of transient drift ratios of 100-year motions are below the 0.5% limit of PEER TBI (2017) for the SLE evaluation (see Figure 5.2d). Note that the transient drift ratios are considerably higher in interface motions than the crustal and intraslab motions. This is because long-period ground motions, i.e., the interface motions, have higher demands at long periods compared to other earthquake sources, which result in larger displacements.

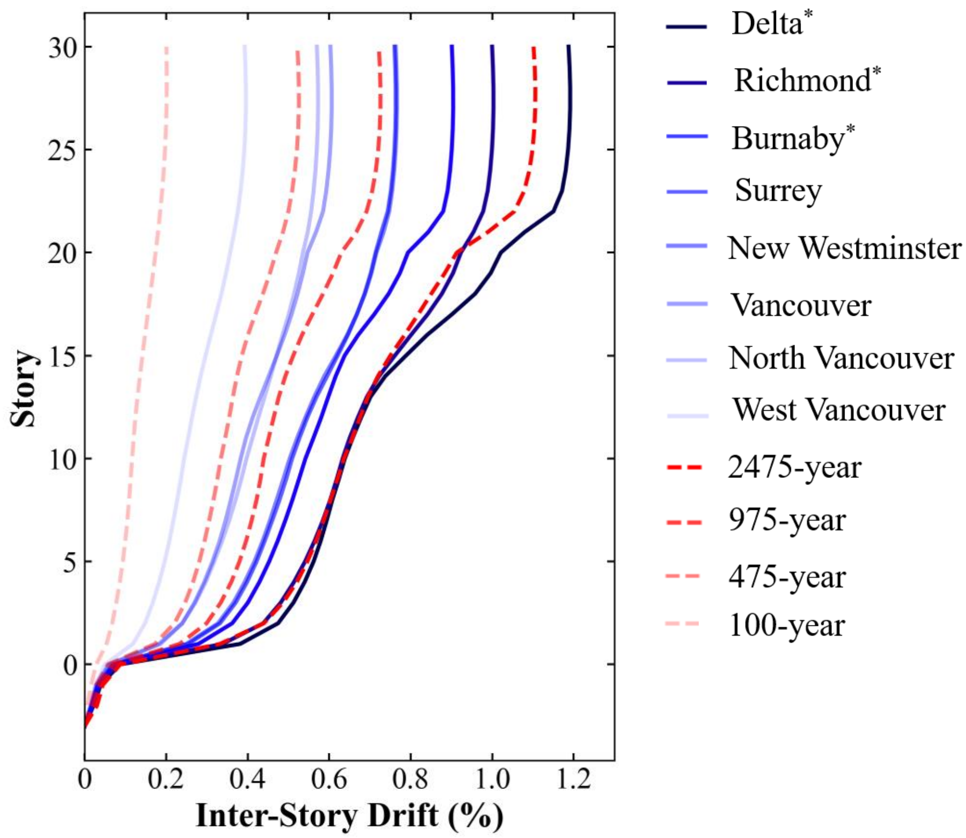

Figure 5.1. Comparison of the transient drift ratios associated with the scenario-based assessments and average response of each hazard level considered in the intensity-based assessments. Sites flagged with an * indicate locations where some time-history analyses resulted in collapse. Refer to Table 6.2 for exact collapse probabilities. Results shown are the average of non-collapse time-history analyses.

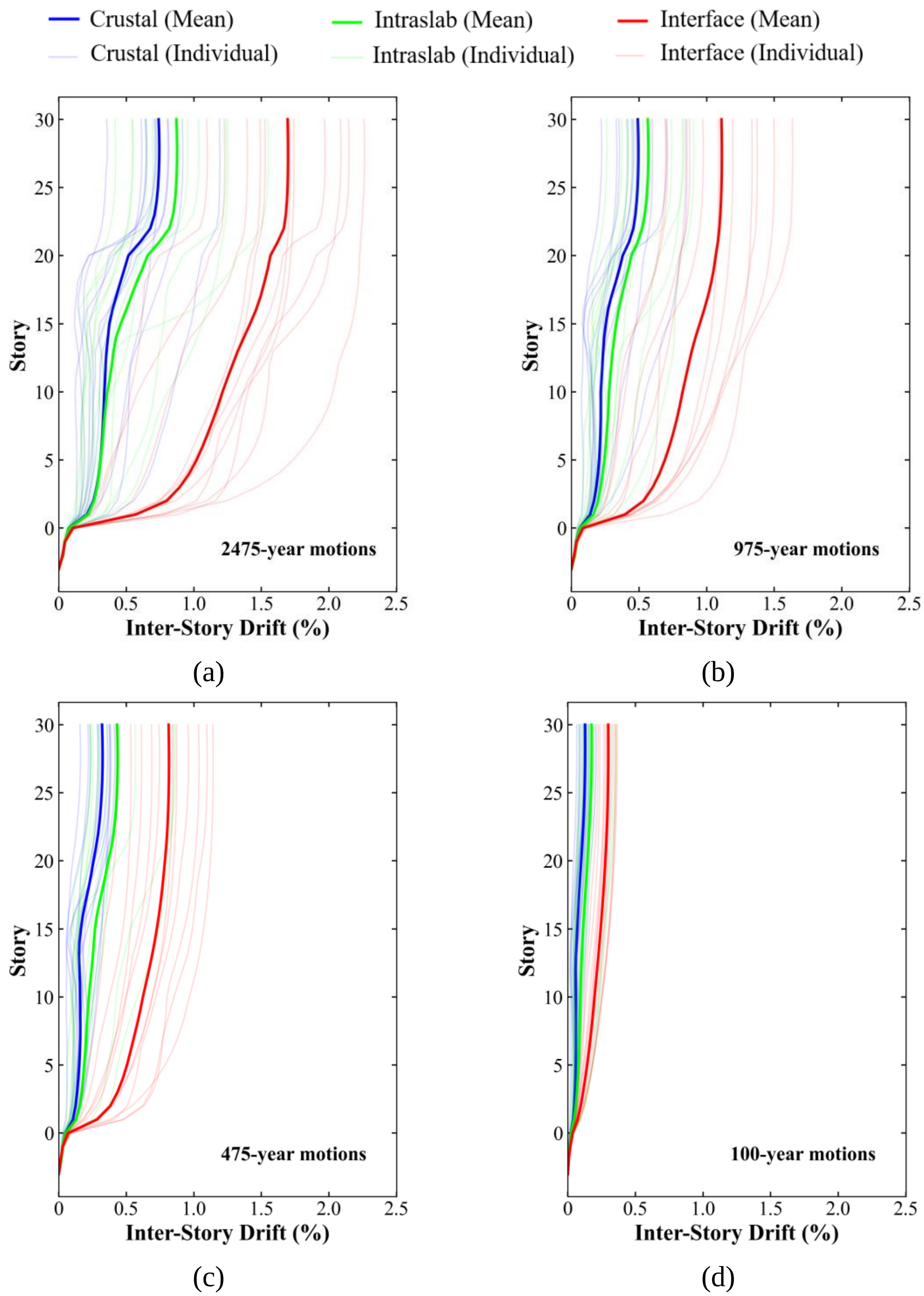

Figure 5.2. Transient drift ratios associated with each seismic source for different hazard levels in the intensity-based assessments: (a) 2475-year motions; (b) 975-year motions; (c) 475-year motions; (d) 100-year motions.

5.1.2 Residual Drift Ratio

Accurate estimation of the residual drift ratio is hard to achieve due to its sensitivity to the hysteretic response of the structural components and ground motion characteristics (Ruiz-García & Miranda, 2006). Therefore, FEMA P-58 (FEMA, 2018) proposed a simplified method to obtain the median residual drift ratio, Δ_r, from the median story drift ratio, Δ, and the median story drift ratio calculated at yield, Δ_y, as shown in Eq. 5.1. In this study, the value of Δ_y is set equal to 0.5% as recommended in Table C-2 of FEMA P-58 (FEMA, 2018) for RCSWs.

$$\begin{aligned} &\Delta_r = 0 && \text{for } \Delta \le \Delta_y \\ &\Delta_r = 0.3(\Delta - \Delta_y) && \text{for } \Delta_y \le \Delta \le 4\Delta_y \\ &\Delta_r = \Delta - 3\Delta_y && \text{for } \Delta \ge 4\Delta_y \end{aligned} \tag{5.1}$$

Figure 5.3 represents the M9 residual drifts at all locations across Metro Vancouver compared with the average responses of the structure under each of the four intensities considered in the intensity-based assessment. The residual drift trend is very similar to that of the transient drift ratios, with Delta having the highest responses, which exceed those of 2475-year motions.

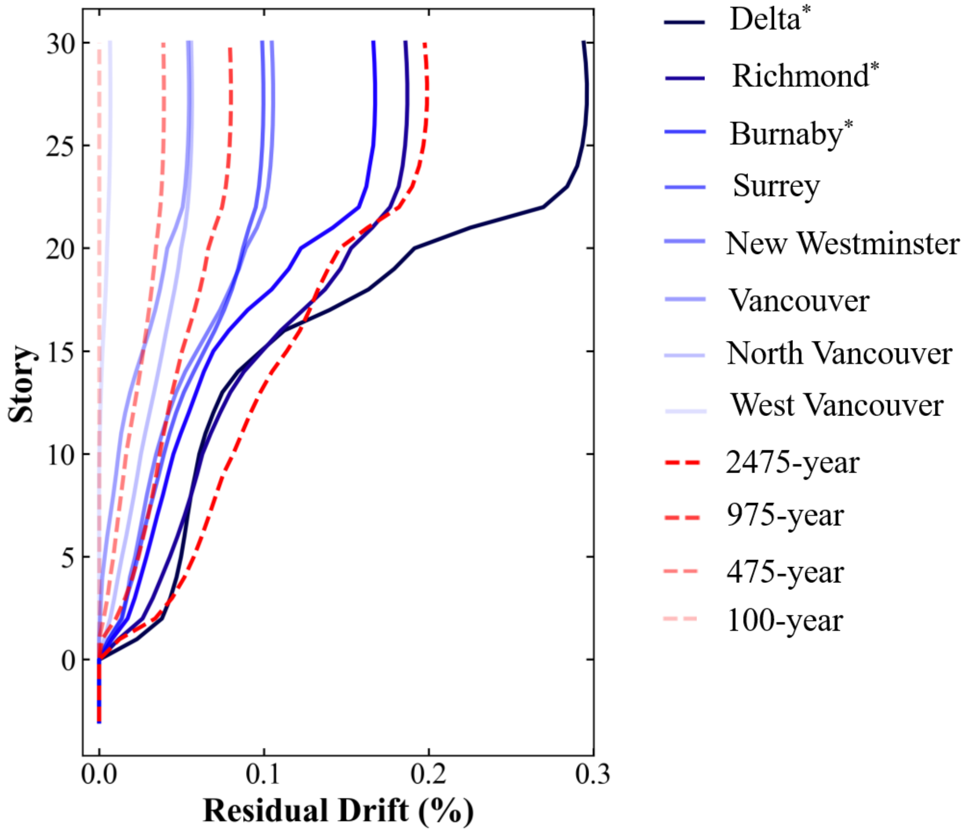

Figure 5.3. Comparison of the residual drift ratios associated with the scenario-based assessments and average response of each hazard level considered in the intensity-based assessments. Sites flagged with an * indicate locations where some time-history analyses resulted in collapse. Refer to Table 6.2 for exact collapse probabilities. Results shown are the average of non-collapse time-history analyses.

Residual drifts associated with different intensity levels are shown in Figure 5.4. Note that PEER TBI (2017) requires that in each story, the mean of the absolute values of the residual drift ratios of the suite of analyses be less than 1%, and the residual drift in each analysis be less than 1.5%. Residual drifts associated with 2475-year motions meet this requirement as illustrated in Figure 5.4a. The inter-story drifts associated with 100-year motions were all less than Δ_y. Therefore, according to Eq. 5.1, residual drifts associated with the 100-year motions are equal to zero.

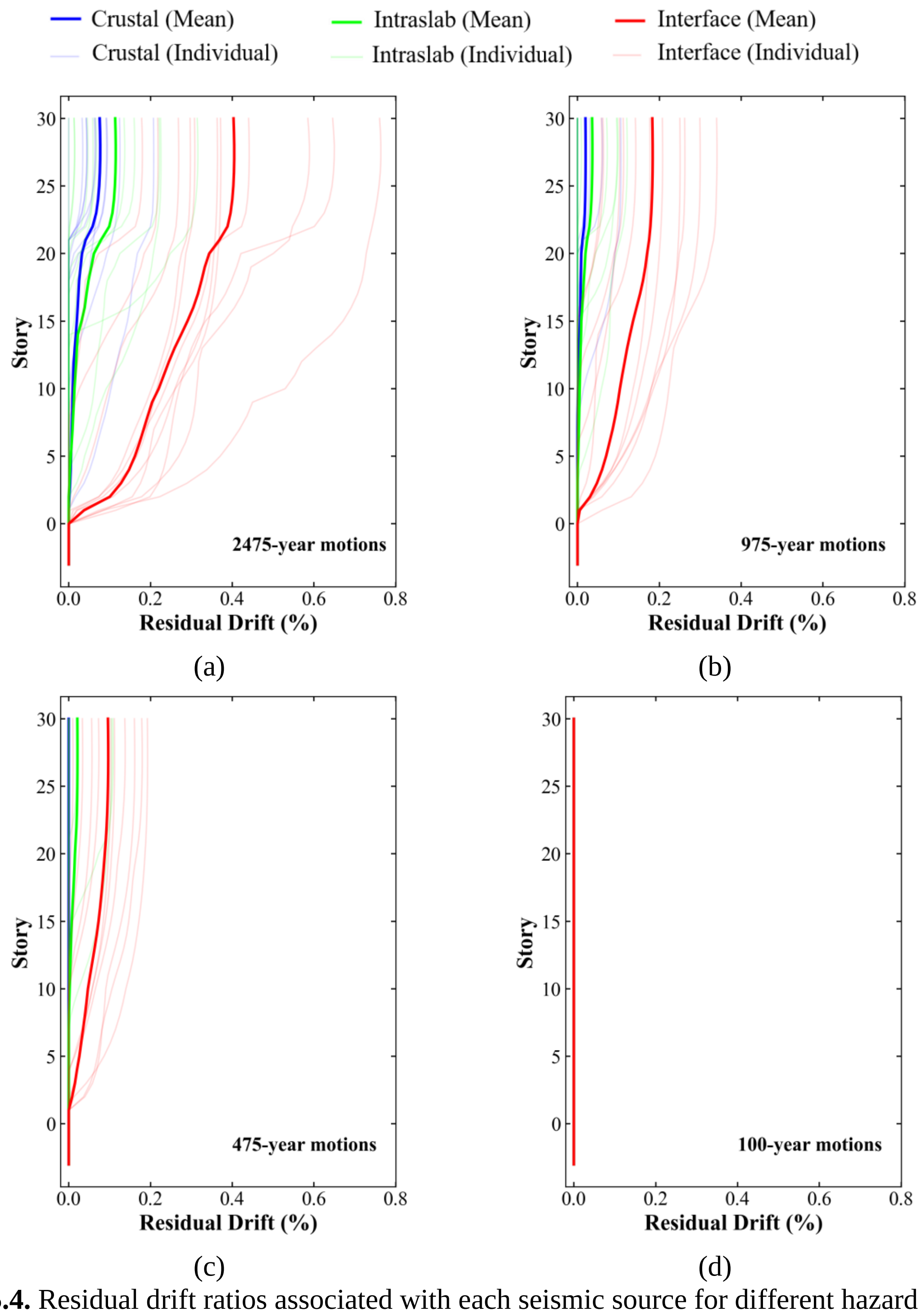

Figure 5.4. Residual drift ratios associated with each seismic source for different hazard levels in the intensity-based assessments: (a) 2475-year motions; (b) 975-year motions; (c) 475-year motions; (d) 100-year motions.

5.1.3 Racking and Damageable Wall Drifts

The damage to the shear walls and gravity wall panels can be measured using different structural responses such as transient drift ratio and racking shear demand. As explained in Section 6.7 of NIST (2017a), story racking shear demand is a better metric than transient drift ratio in measuring the damage to structural and non-structural panels in tall RCSW buildings as the former accounts for vertical racking due to flexural deformation of tall RCSWs and high axial deformation of gravity columns resisting large overturning moments. Also, in contrast to transient drift ratio, the racking shear demand does not include the rigid body rotation which does not cause damage to structural and non-structural elements (Aswegan, 2013). Therefore, this study uses the story racking shear demand instead of the transient drift ratio to determine the damage to wall and gravity panels.

Charney (1990) proposed an index for measuring the racking shear demand, *drift damage index* (DDI), which accounts for horizontal and vertical racking of each panel in the building. Figure 5.5 outlines this *drift damage index* calculation. The figure highlights the deformed shape of a typical tall building and the resultant shear deformations of the wall and gravity panels. In Figure 5.5, horizontal and vertical rotations of the gravity panel are denoted with $\theta_{h,AB}$ and $\theta_{v,AC}$, respectively, and $\theta_{h,CD}$ and $\theta_{v,CE}$ denote the horizontal and vertical rotations of the wall panel, respectively. The *drift damage index* for panel ABCD in Figure 5.5 can be obtained using Eq. 5.2 where X_i and Y_i are respectively the horizontal and vertical displacements of point i, and H and L denote the height and length of the panel, respectively. A similar approach can be followed to obtain the *drift damage index* of the wall panel (i.e., panel CDEF in Figure 5.5). Note that the horizontal and vertical rotations of the gravity panels are in the opposite direction and thus the floor uplift increases the shear racking distortion in the gravity panels. In contrast, the vertical and horizontal rotations of the wall panel are in the same direction which leads to *drift damage index* values lower than the transient drifts in wall panels.

$$\mathrm{DDI} = 0.5\left(\frac{X_B - X_A}{H} + \frac{X_D - X_C}{H} + \frac{Y_C - Y_A}{L} + \frac{Y_D - Y_B}{L}\right) \tag{5.2}$$

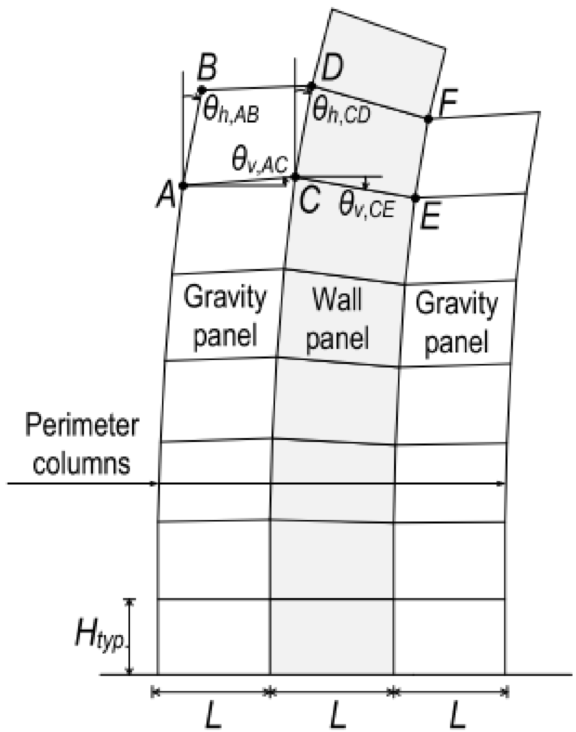

Figure 5.5. Idealized schematic of the building deformation to illustrate damageable drift calculations (Molina Hutt et al., 2022).

The *drift damage index* of the wall panel, hereinafter called damageable wall drift, is obtained using Eq. 5.2 (by using the wall panel corner displacements). Note that since a 2D model is utilized in this study, where shear walls are modeled using line elements (with only one node at each level), it is not possible to obtain horizontal or vertical deformation of the corners of each wall panel directly from the analysis. Therefore, it is assumed that the rotation of lines CD and EF (i.e., $\theta_{h,CD}$ and $\theta_{h,EF}$) are equal to the transient drift ratio at the corresponding level and the rotation of lines

CE and DF (i.e., $\theta_{h,CD}$ and $\theta_{h,EF}$) are equal to the rotation of the nodes at each end of the wall element at the corresponding level. A similar approach is used in Marafi et al. (2019b).

The racking drift ratio is defined as the *drift damage index* of the gravity panel and is used to estimate the slab-column rotation, SCR, consistent with the approach used by Marafi et al. (2019b). The slab-column rotation can be obtained as the maximum story drift, MSD, amplified by a racking factor, λ_{rack} per Eq. 5.3 (Charney, 1990).

$$SCR = \lambda_{rack} \cdot MSD = (1 + \frac{l_w}{2l_{bay}}) \cdot MSD \tag{5.3}$$

where l_{w} is the length of the central core, and l_{bay} is the distance between the face of the core wall and the gravity columns. These result in a value of λ_{rarck} equal to 1.57 in this study. Note that if the gravity columns were modeled in the analysis, it would be possible to obtain the racking drift ratio directly from the analysis using Eq. 5.2.

5.1.3.1 Racking Drift Ratio

The racking drift ratios of the intensity- and scenario-based assessments are plotted in Figure 5.6 for different locations across Metro Vancouver showcasing similar trends to the transient drift ratios. Since the racking drift ratio is computed as 1.57 times the transient drift ratio, the racking drift trend is same as the transient drift ratio (see Figure 5.1). As demonstrated in Figure 5.6, the maximum racking drift ratio in the scenario-based assessment is observed in Delta, which exceeds the racking drift ratio associated with the 2475-year intensity-based assessment. Additionally, the racking drift ratio at each location considered in the scenario-based assessment is higher than that of the 475-year intensity-based assessment except for West Vancouver. Figure 5.7 also demonstrates the racking drift ratios of each seismic source for the four hazard levels considered in the intensity-based assessment.

Racking drift ratio can further be used to determine the collapse of the gravity system. Based on past experimental (Dilger & Brown, 1995; Dilger & Cao, 1991; Megally & Ghali, 2000) and analytical studies (Kourehpaz et al., 2020; Marafi et al., 2020; Eksir Monfared et al., 2021), when the racking drift ratio exceeds 5.9%, non-simulated collapse is assumed to occur due to failure of the gravity system as a result of slab-column connection failure. Based on the analysis results shown in Figure 5.7, the racking drift ratios are less than 5.9% for each hazard level considered in the intensity-based assessments. By contrast, for the scenario-based assessments, there are a few non-simulated collapse cases which are described later in Chapter 6 (Table 6.2).

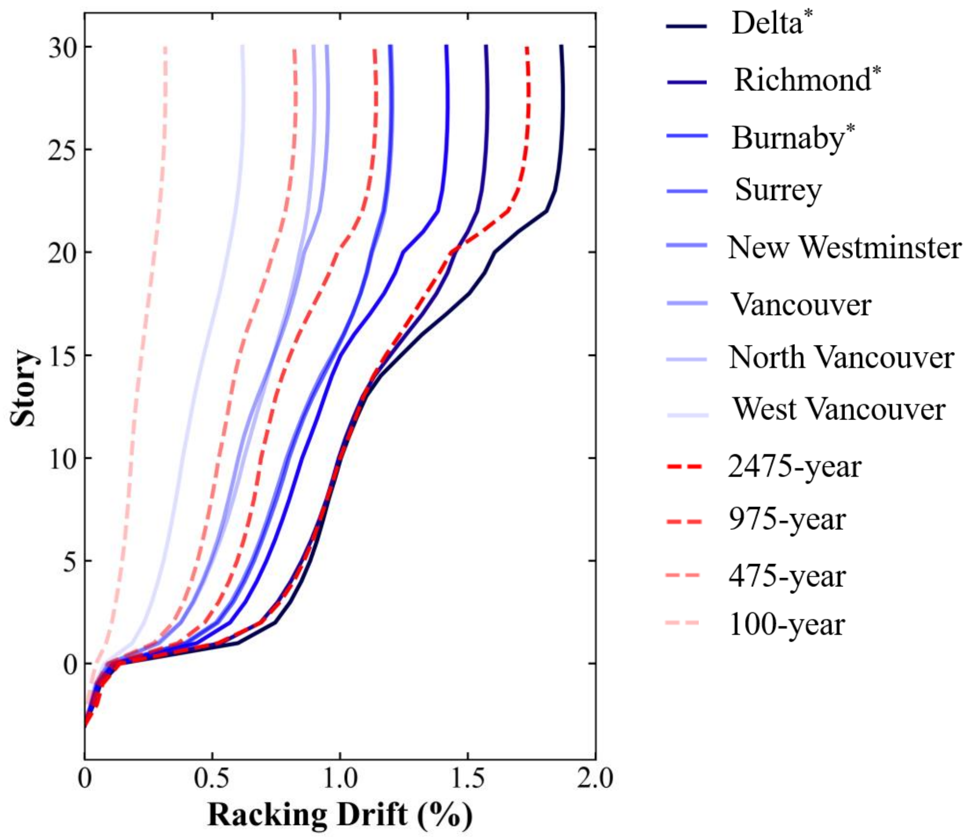

Figure 5.6. Comparison of the racking drift ratios associated with the scenario-based assessments and average response of each hazard level considered in the intensity-based assessments. Sites flagged with an * indicate locations where some time-history analyses resulted in collapse. Refer to Table 6.2 for exact collapse probabilities. Results shown are the average of non-collapse time-history analyses.

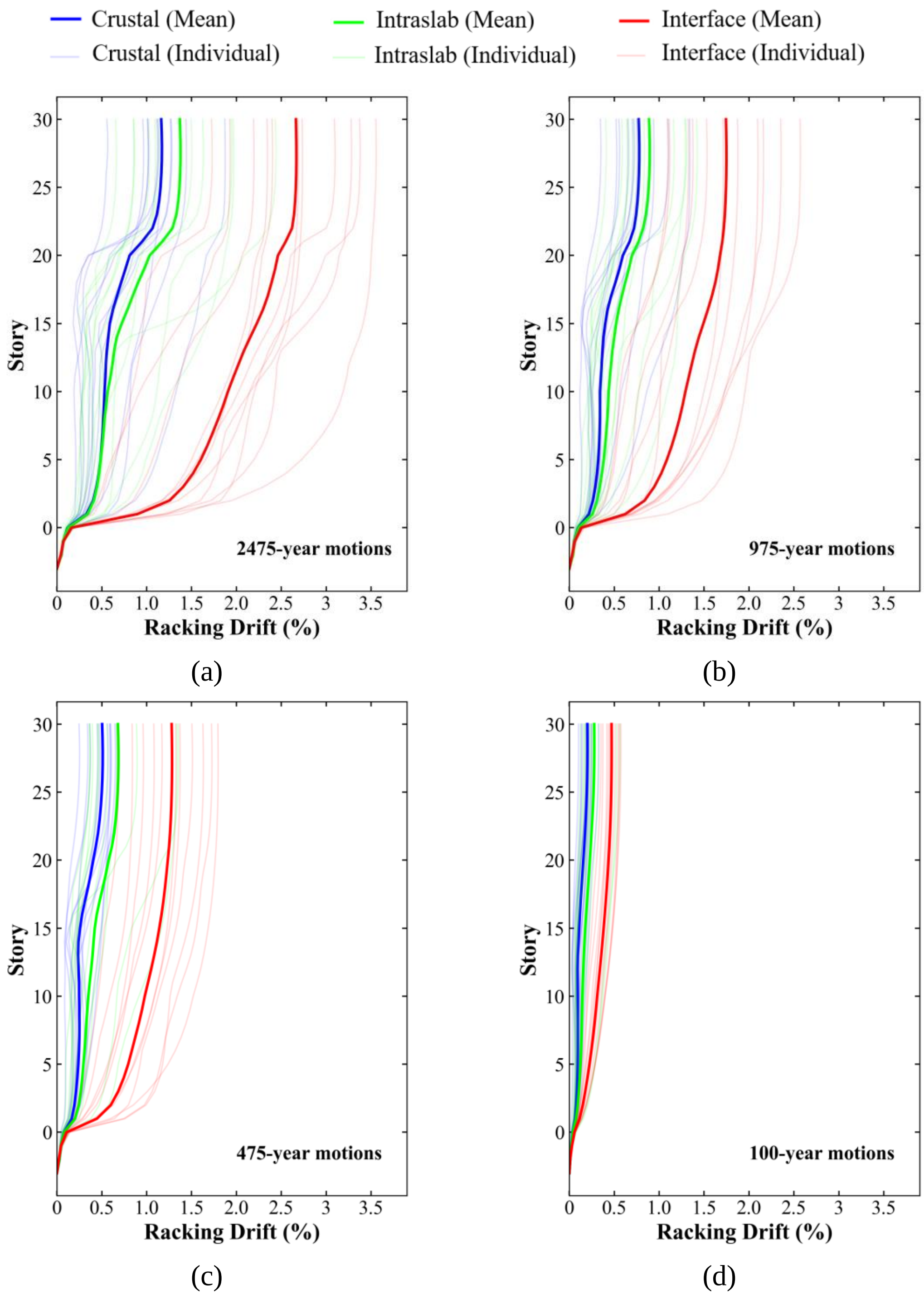

Figure 5.7. Racking drift ratios associated with each seismic source for different hazard levels in the intensity-based assessments: (a) 2475-year motions; (b) 975-year motions; (c) 475-year motions; (d) 100-year motions.

5.1.3.2 Damageable Wall Drift Ratio

Figure 5.8 depicts the damageable wall drift ratios for the scenario-based assessments in all locations compared with the average results of the four hazard levels in the intensity-based assessment. Highest responses are observed at the first story in all locations and for all intensities. The spike in damageable wall drift ratios at story 20 is due to the reduction in wall strength at level 20. Also, the damageable wall drift ratios of all seismic sources considered in the intensity-based assessments are plotted in Figure 5.9. As intended by CSA A23.3-14 (CSA, 2014), the highest damage to the wall occurs at the first story where hinging is expected to initiate.

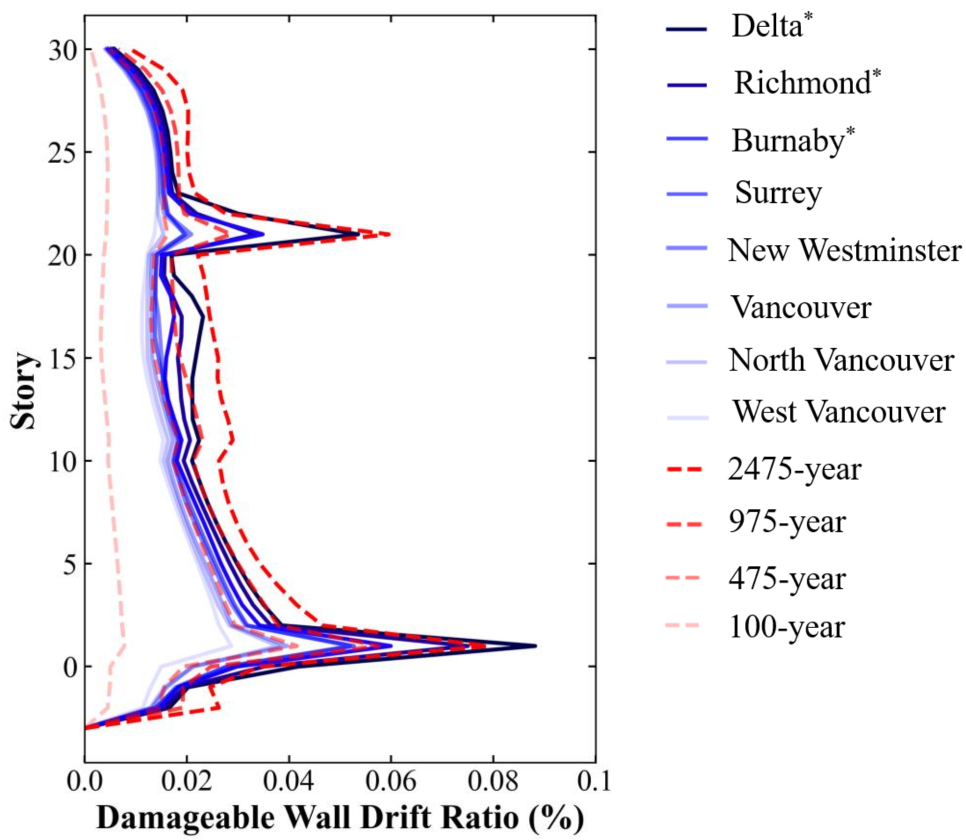

Figure 5.8. Comparison of the damageable wall drift ratios associated with the scenario-based assessments and average response of each hazard level considered in the intensity-based assessments. Sites flagged with an * indicate locations where some time-history analyses resulted in collapse. Refer to Table 6.2 for exact collapse probabilities. Results shown are the average of non-collapse time-history analyses.

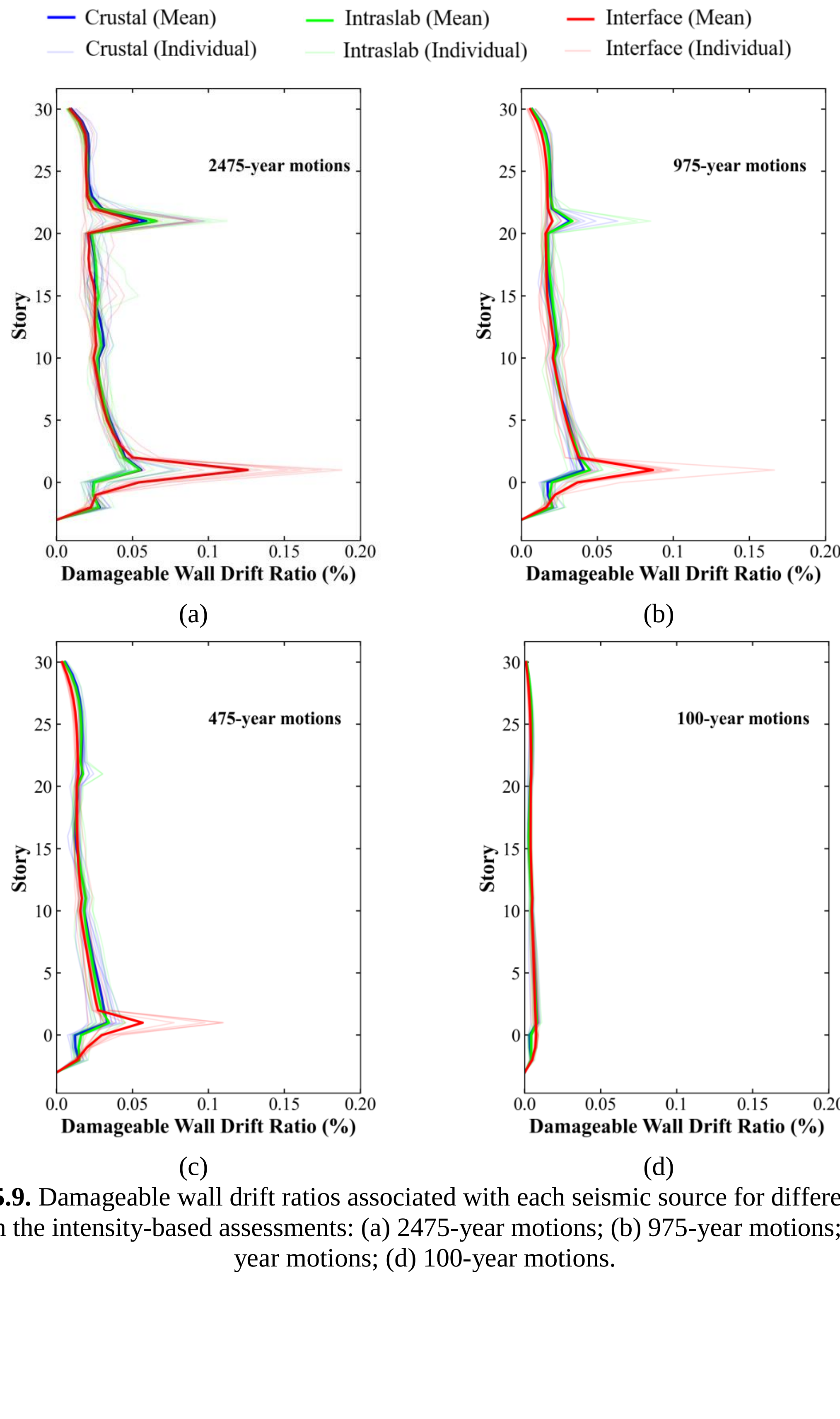

Figure 5.9. Damageable wall drift ratios associated with each seismic source for different hazard levels in the intensity-based assessments: (a) 2475-year motions; (b) 975-year motions; (c) 475-year motions; (d) 100-year motions.

5.2 Peak Floor Acceleration

The peak floor accelerations associated with the average of the three suites used in the intensity-based assessments are compared with those associated with the scenario-based assessments in Figure 5.10. A sharp increase at level 20 can be observed in the 2475-year motions and the scenario-based assessment in Delta. These peaks can be attributed to the reduction in the wall's concrete strength and steel ratio at this level, which results in stress concentration, nonlinearity in the wall and increase in accelerations at level 20 at high shaking intensities. Other than this spike at level 20, the floor acceleration distribution is fairly uniform above the grade level. Also, Figure 5.11 represents the peak floor accelerations for all seismic sources at four different shaking intensities considered in the intensity-based assessments. Note that OpenSeesPy reports the relative floor acceleration when single support excitation is used which is the case in the models produced in this study. Therefore, in order to obtain the absolute floor acceleration, the relative floor acceleration is added to the ground motion acceleration at each time step.

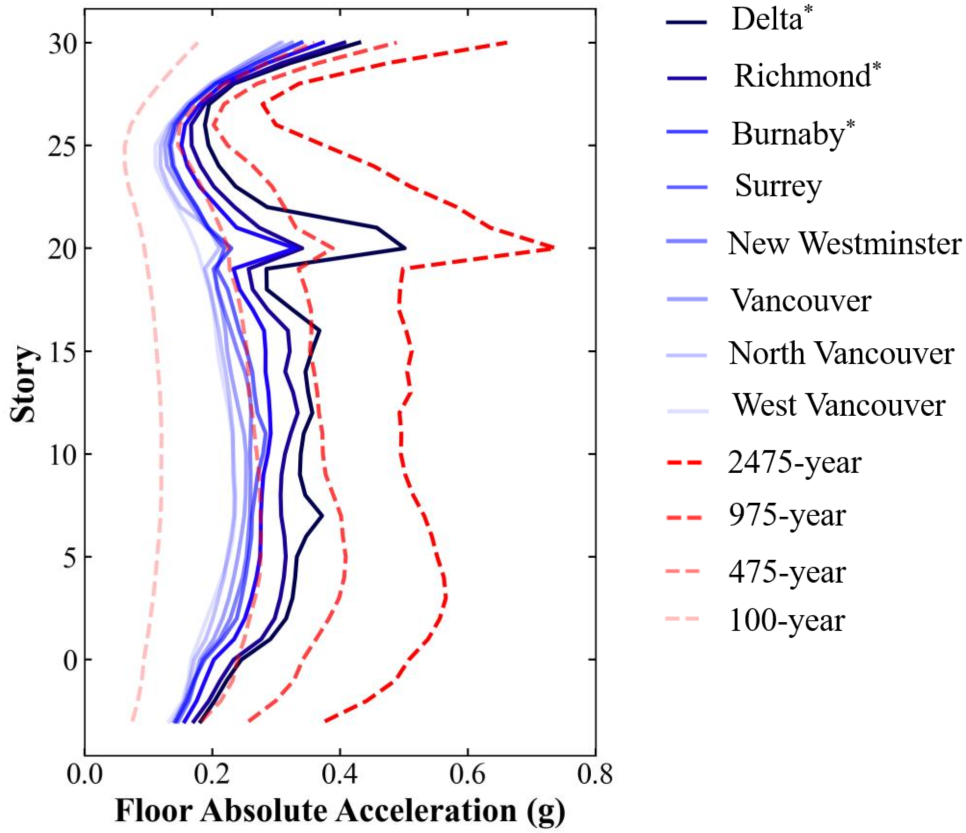

Figure 5.10. Comparison of the peak floor accelerations associated with the scenario-based assessments and average response of each hazard level considered in the intensity-based assessments. Sites flagged with an * indicate locations where some time-history analyses resulted in collapse. Refer to Table 6.2 for exact collapse probabilities. Results shown are the average of non-collapse time-history analyses.

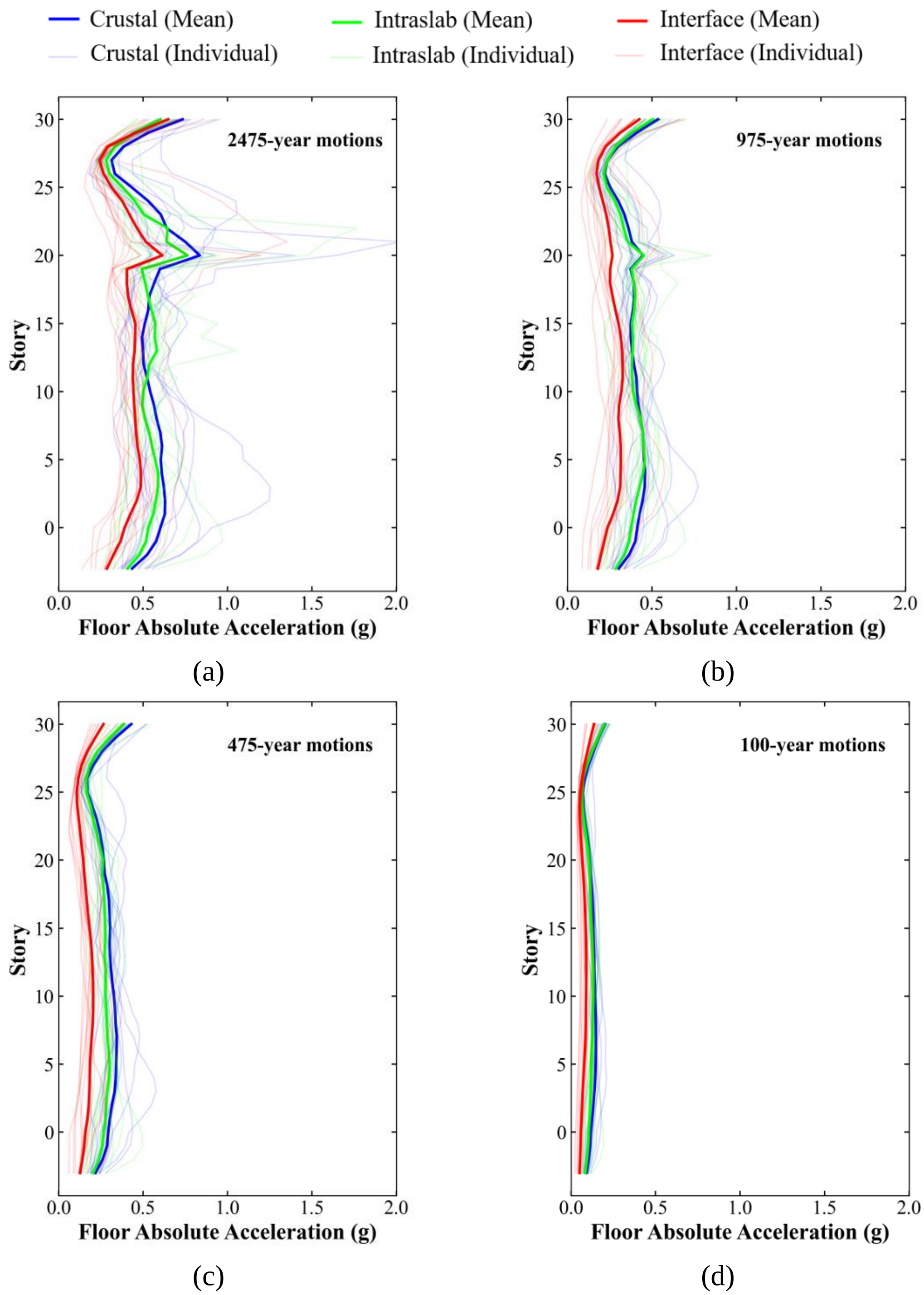

Figure 5.11. Peak floor accelerations associated with each seismic source for different hazard levels in the intensity-based assessments: (a) 2475-year motions; (b) 975-year motions; (c) 475-year motions; (d) 100-year motions.

5.3 Wall Strains

The strain values associated with the outermost concrete and steel fibers are recorded during the analysis and the maximum compression strain of concrete and tensile strain of steel are reported in Sections 5.3.1 and 5.3.2, respectively, and checked against the MCE_R evaluation criteria of PEER TBI (2017).

5.3.1 Concrete Compression

Figure 5.12 shows the maximum compressive strain of concrete at all locations considered in the scenario-based assessments compared with average responses of the four hazard levels considered in the intensity-based assessments. Maximum responses in the scenario-based assessments are observed at the grade level and level 20 (at deep basin sites). The maximum response at Delta exceeds that of 2475-year motions.

The maximum compressive strain of concrete is presented in Figure 5.13 for all seismic sources and hazard levels considered in the intensity-based assessments. As expected, the maximum concrete compressive strain happens at the grade level under the interface motions. However, under the 2475- and 975-year crustal and intraslab motions, the maximum concrete compressive strain occurs at level 20 due to the significant higher mode response of the building when subjected to such motions, as well as the reduction in concrete strength and steel reinforcement ratio at this level. The maximum concrete compressive strain is far less than the limit of 0.015 as required by PEER TBI (2017). In fact, the concrete does not reach its peak compressive strength and therefore, no softening response of the concrete material is observed.

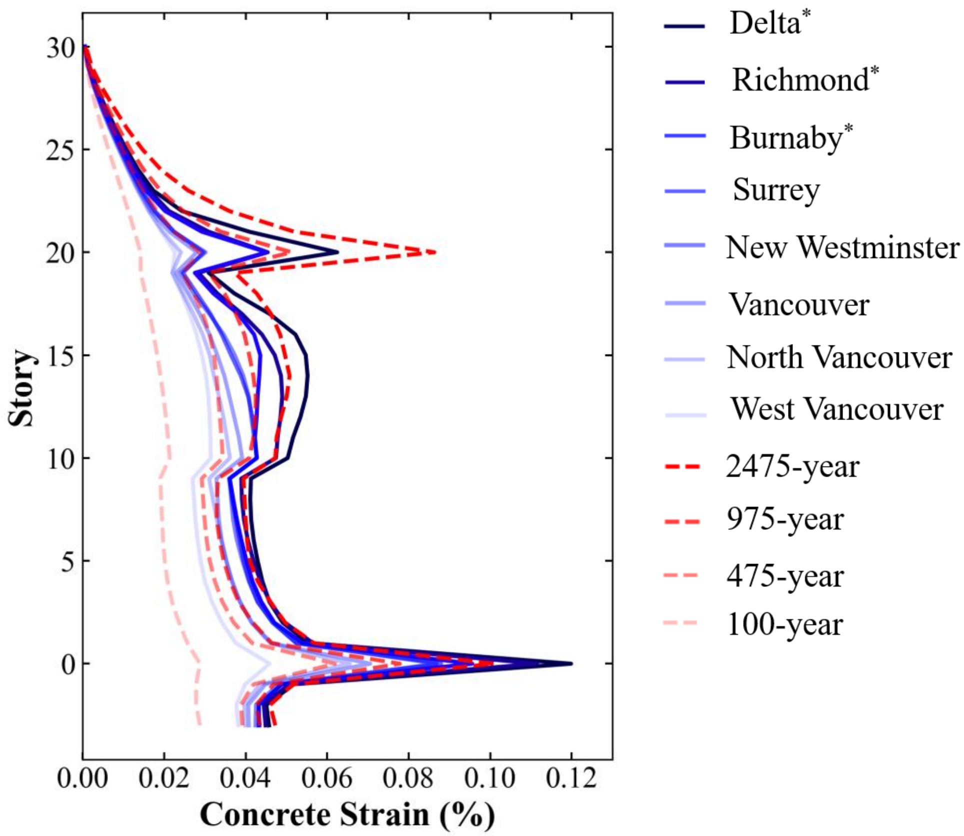

Figure 5.12. Comparison of the peak concrete compressive strain associated with the scenario-based assessments and average response of each hazard level considered in the intensity-based assessments. Sites flagged with an * indicate locations where some time-history analyses resulted in collapse. Refer to Table 6.2 for exact collapse probabilities. Results shown are the average of non-collapse time-history analyses.

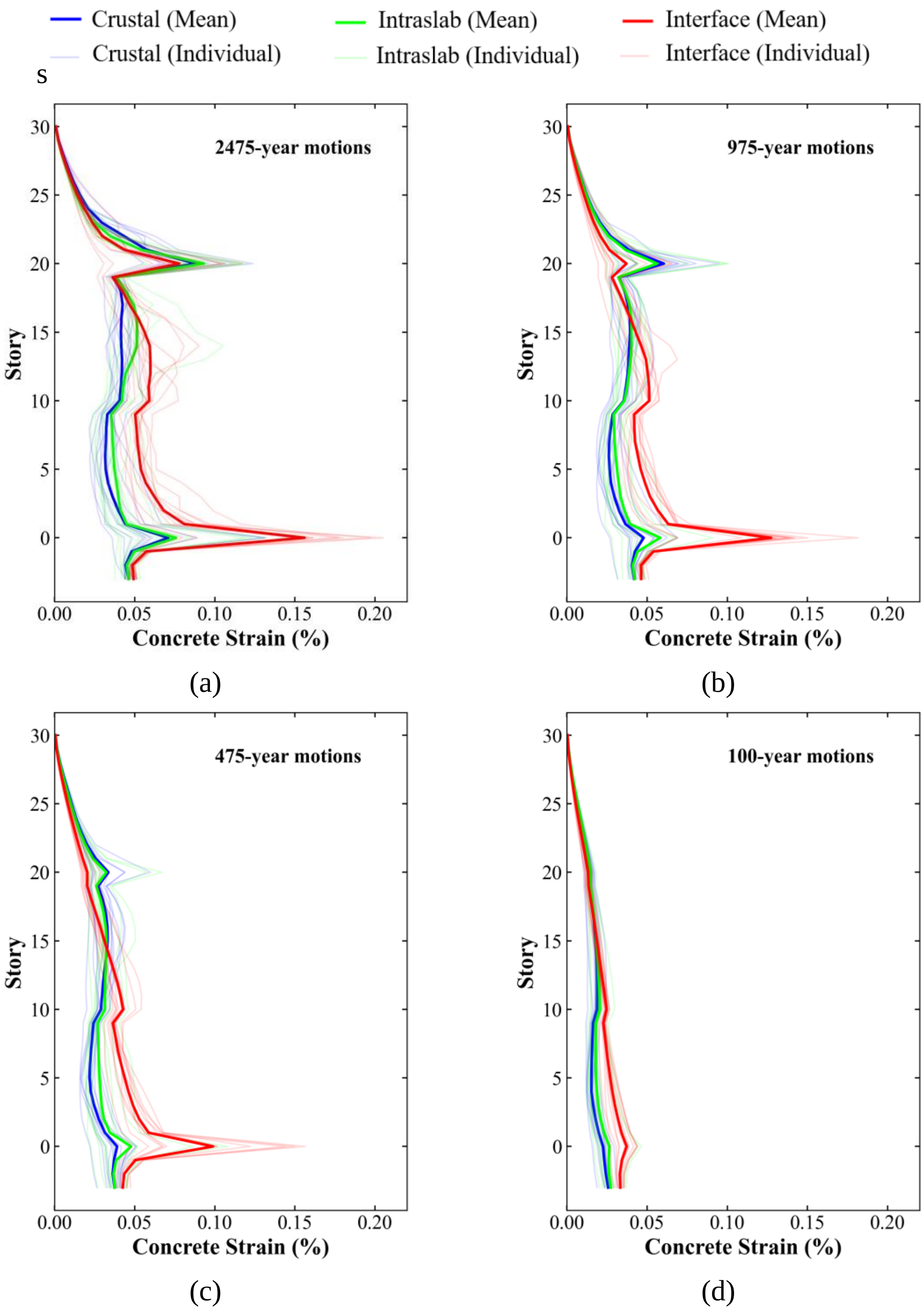

Figure 5.13. Peak concrete compressive strain associated with each seismic source for different hazard levels in the intensity-based assessments: (a) 2475-year motions; (b) 975-year motions; (c) 475-year motions; (d) 100-year motions.

5.3.2 Steel Tension

Figure 5.14 represents the maximum steel tensile strain for all locations considered in the scenario-based assessments compared with the average of the three suites used in the intensity-based assessments. The steel strain distribution in scenario-based assessments is similar to that under the 2475-year motions with peak responses at grade level and a sharp increase at level 20. Figure 5.14 shows that maximum steel strain in Delta exceeds that of 2475-year motions.

The mean of the maximum tensile strain of steel material for each seismic source and shaking intensity is shown in Figure 5.15. The maximum steel tension happens at grade level in the interface motions. However, as mentioned in Section 5.3.1, the maximum responses of crustal and intraslab suites are observed at level 20 due to significant higher mode response of the building when subjected to these motions as well as the lower concrete strength and steel reinforcement ratio of the wall at this level which causes stress concentration and more nonlinearity in the walls. Nonetheless, the tensile steel strain is far less than the 5% limit of PEER TBI (2017) under the MCE_R evaluation.

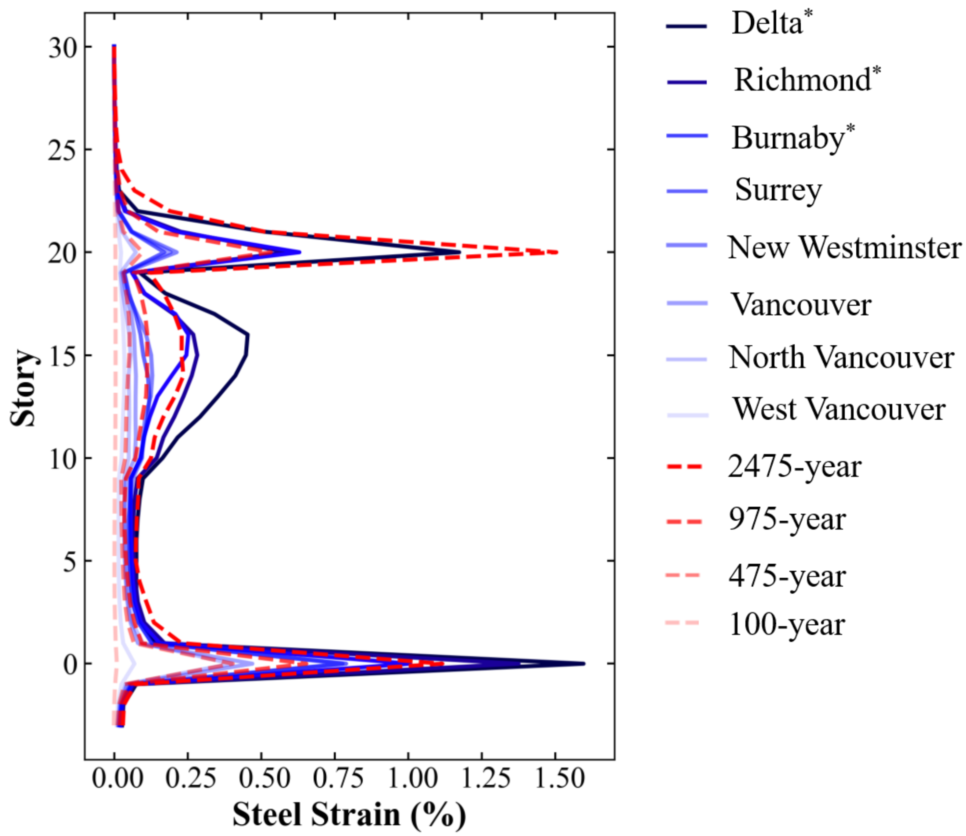

Figure 5.14. Comparison of the peak steel tensile strain associated with the scenario-based assessments and average response of each hazard level considered in the intensity-based assessments. Sites flagged with an * indicate locations where some time-history analyses resulted in collapse. Refer to Table 6.2 for exact collapse probabilities. Results shown are the average of non-collapse time-history analyses.

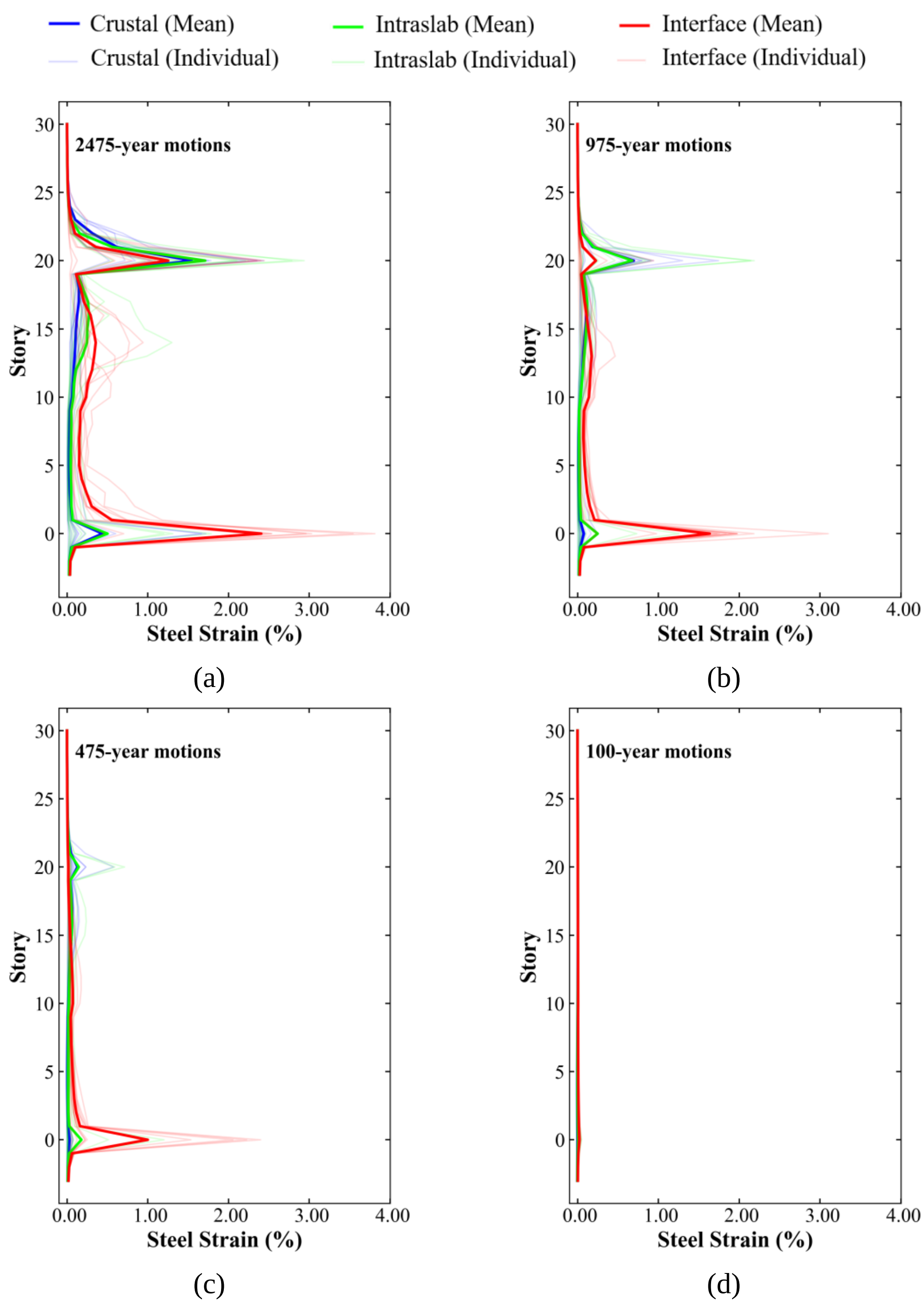

Figure 5.15. Peak steel tensile strain associated with each seismic source for different hazard levels in the intensity-based assessments: (a) 2475-year motions; (b) 975-year motions; (c) 475-year motions; (d) 100-year motions.

5.4 Wall Shear Force

Figure 5.16 illustrates the mean shear demand of each pier for the scenario-based assessments at different locations as well as different hazard levels in the intensity-based assessments. The highest shear demand is observed at grade level. Higher shear demands are observed at sites with higher $Z_{2.5}$ values.

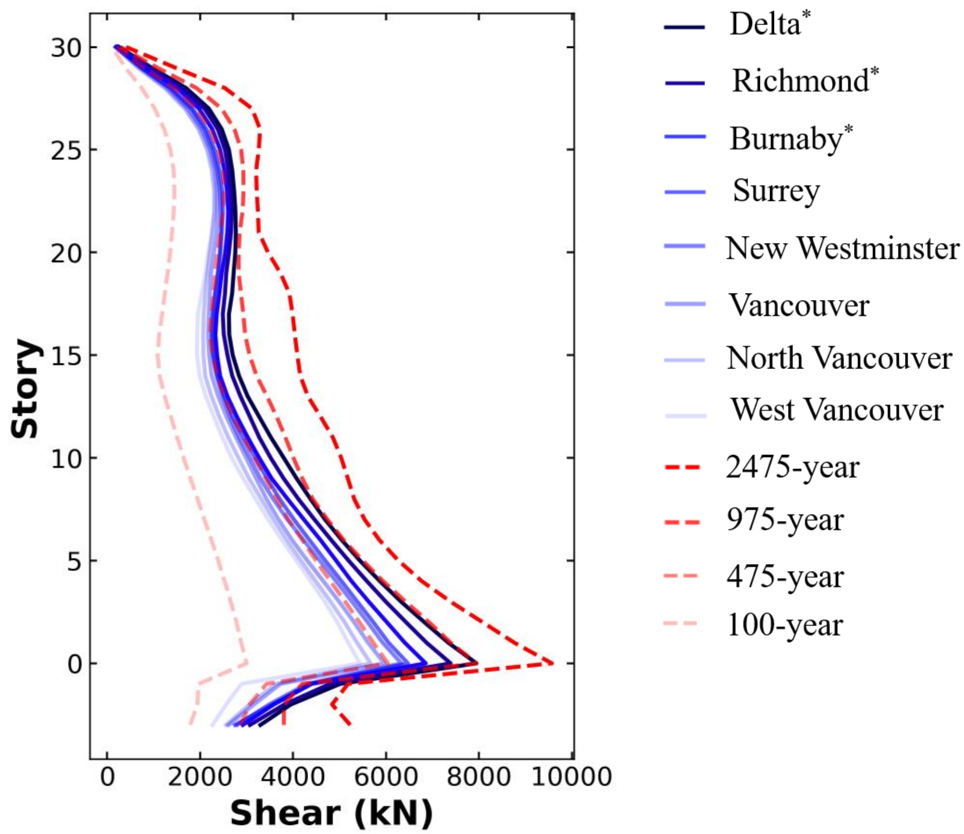

Figure 5.16. Comparison of RC pier shear demand associated with the scenario-based assessments and average response of each hazard level considered in the intensity-based assessments. Sites flagged with an * indicate locations where some time-history analyses resulted in collapse. Refer to Table 6.2 for exact collapse probabilities. Results shown are the average of non-collapse time-history analyses.

The mean shear demand of each pier for each seismic source and hazard level is plotted in Figure 5.17. As expected, the highest shear demand is observed at grade level. Note that as opposed to the inter-story drifts, the shear demands are more consistent across the three seismic sources (see Figure 5.17a). This is because the higher modes associated with the short-period ground motions, i.e., crustal and intraslab motions, result in higher shear demands (Eksir Monfared, 2020). As explained in Eksir Monfared (2020), PEER TBI (2017) requires mean shear demands be amplified by a factor of 1.3 to be less than the ultimate capacity, V_u, amplified by a bias factor determined as a function of the ductility demands in the walls as outlined in PEER TBI (2017). The shear forces obtained from the nonlinear analyses in this study meet the performance-based seismic design requirements of PEER TBI (2017).

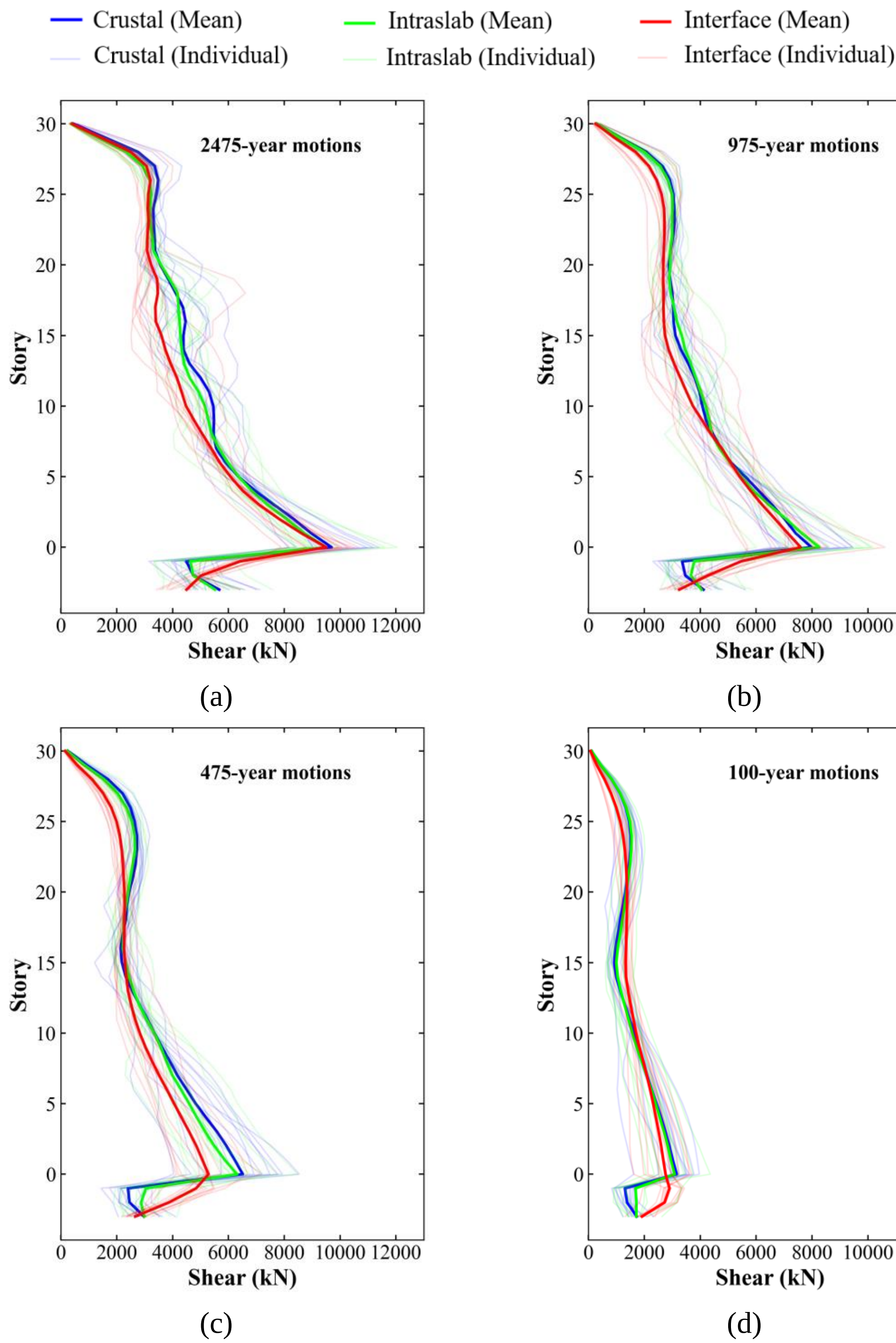

Figure 5.17. RC pier shear demand associated with each seismic source for different hazard levels in the intensity-based assessments: (a) 2475-year motions; (b) 975-year motions; (c) 475-year motions; (d) 100-year motions.

5.5 Summary of Structural Responses

The peak structural responses of each location considered in the scenario-based assessments and each hazard level included in the intensity-based assessments are summarized in Table 5.1. As observed in the table, the structural responses are significantly higher at locations with deeper basin depths due to higher basin amplification effects. Most of the responses at Delta exceed those of the 2475-year motions, which are used to design the building archetypes. Even though the M9 motions have a return period of approximately 500 years, the structural responses associated with the simulated M9 motions are significantly higher than those associated with the 475-year motions at all locations except West Vancouver which is located outside the basin.

Table 5.1. Summary of peak of the means of structural responses for all locations and hazard levels.

Site/Hazard level	SDR[1] (%)	ReDR[2] (%)	RaDR[3] (%)	DWDR[4] (%)	PFA[5] (g)	ε_c[6] (%)	ε_s[7] (%)	V[8] (kN)
Delta*	1.19	0.30	1.87	0.09	0.61	0.12	1.60	7946
Richmond*	1.00	0.19	1.58	0.08	0.57	0.11	1.37	7390
Burnaby*	0.90	0.17	1.42	0.06	0.52	0.10	1.01	6854
Surrey	0.76	0.10	1.20	0.05	0.46	0.09	0.79	6472
New Westminster	0.77	0.11	1.20	0.05	0.46	0.09	0.78	6330
Vancouver	0.61	0.05	0.95	0.04	0.44	0.07	0.47	5963
North Vancouver	0.57	0.06	0.90	0.04	0.41	0.07	0.40	5670
West Vancouver	0.40	0.01	0.62	0.03	0.40	0.05	0.07	5439
2475-year	1.11	0.20	1.74	0.08	0.74	0.10	1.50	9570
975-year	0.73	0.08	1.14	0.06	0.49	0.08	0.65	7948
475-year	0.53	0.04	0.83	0.04	0.36	0.06	0.40	6038
100-year	0.20	0.00	0.32	0.01	0.18	0.03	0.01	3001

* Sites flagged with an * indicate locations where some time-history analyses resulted in collapse. Refer to Table 6.2 for exact collapse probabilities. Results shown are the average of non-collapse time-history analyses.

[1]Story drift ratio

[2]Residual drift ratio

[3]Racking drift ratio

[4]Damageable wall drift ratio

[5]Peak floor acceleration

[6]Concrete strain

[7]Steel strain

[8]Shear

Other important findings of this section are summarized below:

- The nonlinear response-history analyses results of 2475-year motions meet the MCE_R evaluation criteria of PEER TBI (2017) which suggests that the prescriptive design of the Canadian standard also complies with performance-based seismic design requirements.

- While the structural responses associated with probabilistic seismic hazards (NSHM 2015) are similar at different locations across Metro Vancouver, high variations are observed in structural responses associated with M9 motions across Metro Vancouver. For instance, the maximum transient drift ratio in Delta, the deepest basin site, is more than five times of the maximum transient drift ratio at West Vancouver which is located outside the basin. This sharp variation is not observed in 2015 NSHM (Adams et al., 2015) which neglects the sedimentary basin effects.

- Maximum damageable wall drift ratios are observed at grade level in the intensity-based assessments motions, which complies with the intended seismic mechanism of core RSCW buildings in the cantilevered direction. A spike in structural damage is observed at level 20 due to higher mode effects as well as wall strength reduction. This is more significant in the intraslab and crustal 2475-year motions, as well as scenario-based assessments in Delta, Richmond, and Burnaby due to significant higher mode response in such motions. For the same reason, the maximum floor accelerations are observed at level 20 in these motions.

Chapter 6: Damage and Loss Assessment

This chapter discusses the earthquake-induced repair costs of the archetypical RCSW buildings associated with the intensity- and scenario-based assessments. The loss model assumptions are provided in Section 6.1 and loss assessment results are provided in Section 6.2, including a deaggregation of results to highlight main loss contributors.

6.1 Building Performance Model

The loss assessment is conducted in Pelicun, an open-source python-based loss estimation tool (Zsarnoczay & Kourehpaz, 2021), which leverages the well-established FEMA P-58 (FEMA, 2018) methodology as described in Section 2.6. Consistent with previous studies (e.g. Kourehpaz et al., 2020), 2000 Monte Carlo simulations are used for the loss assessment. The EDPs obtained from the time-history analysis (Chapter 5), are obtained using the 2015 NSHM and simulated ground motions of M9 CSZ earthquakes, as used in the intensity- and scenario-based assessments, respectively. Even though the time-history analyses have been carried out only in the cantilevered direction, similar to Kourehpaz et al. (2020), the resultant EDPs are used to evaluate damage and loss in both building directions. This assumption simplifies the structural modeling and the performance-based assessment of the building. Note that generally the structural responses are different in the coupled and cantilevered directions. However, the structural response parameters reported by Eksir Monfared et al. (2021) for the archetype building considered in this study are similar in both directions and thus, this assumption does not significantly affect the accuracy of the loss assessment results.

The EDPs used in the loss assessment are selected based on their ability to predict the damage to the structural and non-structural elements. To this end, peak floor acceleration is used to estimate the damage to acceleration-sensitive components, and the peak story drift is used to determine the damage to the staircase and curtain walls. The damage to the elevator guide rail system is estimated as a function of residual drift ratios. Also, damageable wall drift ratio is used to predict the damage to the shear walls, and racking drift ratio represents the damage to components such as slab-column connections and wall partitions. As discussed in Section 5.1.3, these EDPs account for both horizontal and vertical relative deformations of the structural and non-structural wall panels and do not consider the rigid body rotation which does not induce any damage to the panels. Therefore, the damageable wall and racking drift ratios are used in lieu of transient drift ratio in the loss assessment as they serve as a better proxy for damage.

The building performance model includes the typical components used in common RCSW buildings with quantities found in residential building as outlined in Kourehpaz et al. (2020). Details regarding the fragility groups and their quantities are provided in Table 6.1. Fragility functions are used in conjunction with the EDPs to determine the damage state of each component. Following damage state predictions, component specific consequence functions, as defined by FEMA P-58 (FEMA, 2018), are used to translate the damage states into repair costs.

Table 6.1. Components considered in the building performance model of the RCSW building archetype.

Fragility ID	Component	Quantity[1]	Unit	Location	EDP
B1044.101	Slender Concrete Wall (x-dir.)	1.83	144 SF	Basement Levels	Wall Damageable Drift
		2.32		1st Story above Gr.	
		1.77		Stories (above 1st)	
B1044.102	Slender Concrete Wall (y-dir.)	3.28	144 SF	Basement Levels	Wall Damageable Drift
		4.16		1st Story above Gr.	
		3.17		Stories (above 1st)	
B1049.012	RC Slab-Column Connection	12	Each	All Stories	Racking Drift
B2022.201_ud[3]	Curtain Walls (x-dir.)	68.17	30 SF	1st Story above Gr.	Story Drift
		52		Stories (above 1st)	
B2022.201_ud	Curtain Walls (y-dir.)	70.66	30 SF	1st Story above Gr.	Story Drift
		53.89		Stories (above 1st)	
C1011.001a	Wall Partition w/ Metal Studs (x- and y-dir.)	4.18	100 LF	Stories (TYP.)[4]	Racking Drift
C3011.001a	Wall Partition Finishes (x- and y-dir.)	1.33	100 LF	Stories (TYP.)	Racking Drift
C2011.001a	Prefabricated Steel Stair w/ Seismic Joint (x- and y-dir.)	2	Each	All Stories	Story Drift
D101411ridr[5]	Elevator Guide Rail System	4	Each	Ground Level	Residual Drift
D1014.011	Traction Elevator Cabin	4	Each	Ground Level	Acceleration
D3041.001c	HVAC Fan	0.35	10 Each	Stories (TYP.)	Acceleration
D3041.011c	HVAC Ducting	0.4	1000 LF	Stories (TYP.)	Acceleration
D5012.023b	Low Voltage Switchgear	1	225 Amp	Stories (TYP.)	Acceleration
D2022.023a	Heating Water Piping – Large Diameter	0.039	1000 LF	Stories (TYP.)	Acceleration
D2022.013a	Heating Water Piping – Small Diameter	1.05	1000 LF	Stories (TYP.)	Acceleration
D2022.023b	Heating Water Pipe Bracing – Large Diameter	0.039	1000 LF	Stories (TYP.)	Acceleration
D2022.013b	Heating Water Pipe Bracing – Small Diameter	1.05	1000 LF	Stories (TYP.)	Acceleration

Continued on next page

Table 6.1. continued from previous page

Fragility ID	Component	Quantity[1]	Unit	Location	EDP
D2021.023a	Potable Water Piping	0.052	1000 LF	Stories (TYP.)	Acceleration
D2021.023b	Potable Water Pipe Bracing	0.052	1000 LF	Stories (TYP.)	Acceleration
D3041.041b	Variable Air Volume Box	0.4	10 Each	Stories (TYP.)	Acceleration
D2031.023a	Sanitary Waste Piping – Piping Fragility	0.934	1000 LF	Stories (TYP.)	Acceleration
D2031.023b	Sanitary Waste Piping – Bracing Fragility	0.934	1000 LF	Stories (TYP.)	Acceleration
D4011.023a	Fire Sprinkler Water Piping	1.53	1000 LF	Stories (TYP.)	Acceleration
D4011.053a	Fire Sprinkler Drop	0.84	1000 LF	Stories (TYP.)	Acceleration
D3041.032c	HVAC Drops / Diffusers	5.6	10 Each	Stories (TYP.)	Acceleration
C3032.003a	Suspended Ceiling	27.88	250 SF	1st Story above Gr.	Acceleration
D3031.023i	Cooling Tower	2	Each	Roof Only	Acceleration
D3052.013i	Air Handling Unit	2	Each	Roof Only	Acceleration
D3031.013f	Chiller	1	Each	Roof Only	Acceleration

[1] These quantities are relative to the unit values.
[2] All stories include typical stories (above grade) as well as basement levels (below grade).
[3] User-defined fragility functions were defined for three damage states with the median story drift ratios of 0.02, 0.03, and 0.04, respectively. Dispersion was assumed to be equal to 0.3 for all damage states.
[4] Includes all stories above ground.
[5] User-defined fragility functions were defined for two damage states with the median elevator residual drift ratios of 0.002 and 0.005, respectively. Dispersion was assumed to be equal to 0.3 for both damage states.

The modeling uncertainty is obtained using Eq. 6.1 as per FEMA P-58 (FEMA, 2018) where β_m is the modeling uncertainty, β_c is the building definition and construction quality assurance and β_q is the quality and completeness of the analytical model.

$$\beta_m = \sqrt{\beta_c^{\ 2} + \beta_q^{\ 2}} \tag{6.1}$$

This study assumes the construction quality assurance and the quality of the analytical model is average and thus, according to Tables 5-1 and 5-2 of FEMA P-58-1 (FEMA, 2018), β_q and β_c are both equal to 0.25 and the resultant modeling uncertainty, β_m, is equal to 0.35. The record-to-record variability is explicitly captured in this study due the large number of ground motion pairs employed in the scenario- and intensity-based assessments.

Collapse happens as a result of simulated wall failure and non-simulated slab-to-column connection failure. As shown in Section 3.2.1.2, the walls of the building archetypes have a hardening response and therefore, wall failure happens due to the rupture of longitudinal bars. Per Vamvatsikos & Cornell (2002), the non-converged motions are considered as simulated collapse. Collapse probability is then obtained by dividing the number of collapse occurrences by the total number of simulations used at each location in the scenario-based assessment and each hazard level in the intensity-based assessment. While the collapse probabilities in the scenario-based assessments are 16.7, 6.7, and 3.3% in Delta, Richmond, and Burnaby, respectively, no collapse cases are observed in other locations considered in the scenario-based assessments or any hazard level considered in the intensity-based assessments. The number of simulated and non-simulated collapse cases and the collapse probability at different sites in the scenario-based assessments are provided in Table 6.2. These collapse probabilities are used by Pelicun to determine the number of collapse realizations in the Monte Carlo simulations. For example, the number of collapse realizations for the scenario-based assessment in Delta is 334 which corresponds to 16.7% of the 2000 Monte Carlo simulations.

As per FEMA P-58 (FEMA, 2018), reparability of the building in each realization is assessed by means of a repair fragility function with a median residual drift ratio of 1% and a dispersion of 0.3.

Table 6.2. Collapse probabilities at different sites in the scenario-based assessment.

Location	Number of simulated collapses	Number of non-simulated collapses	Collapse probability (%)
Delta	6	4	16.7
Richmond	4	0	6.7
Burnaby	2	0	3.3
Surrey	0	0	0
New Westminster	0	0	0
Vancouver	0	0	0
North Vancouver	0	0	0
West Vancouver	0	0	0

For each repairable realization, the total loss is equal to the sum of the repair costs of all structural and non-structural components included in the building performance model. The loss associated with irreparable and collapse realizations is equal to the building replacement cost. Finally, the mean loss ratio is obtained by calculating the average loss across all realizations normalized by the building replacement cost which is taken as \$2475 USD (~\$3350 CAD) per square meter (RSMeans, 2020), resulting in a total asset value of \$54,959,850 USD.

To ensure the structural responses of the 2000 Monte Carlo realizations are good representatives of the structural responses obtained from the nonlinear time-history analysis, the mean and median of Monte Carlo simulations are compared with the mean of time-history analysis for all EDPs. This comparison is shown in Figure 6.1 for 2475-year where the Monte Carlo simulations EDPs are in good agreement with the structural analysis results.

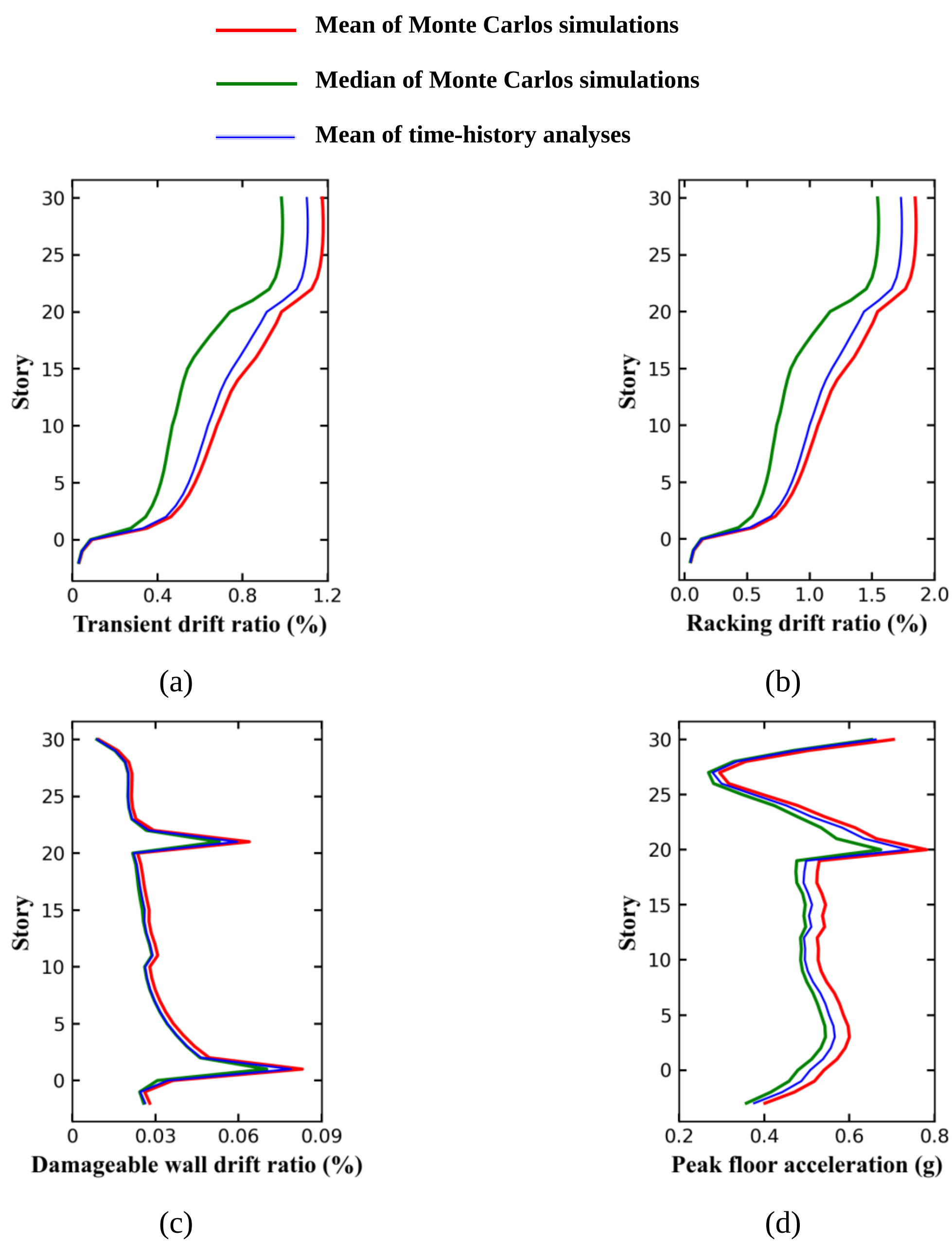

Figure 6.1. Comparison of the EDPs obtained from Monte Carlo simulation and time-history analysis for 2475-year motions: (a) transient drift ratio; (b) racking drift ratio; (c) damageable wall drift ratio; (d) peak floor acceleration.

The transient drift ratios obtained from time-history analysis are less than the maximum yield drift ratio of 0.5% suggested by FEMA (2018) in many of the ground motions. Therefore, according to Eq. 5.1, the residual drift ratios of many ground motions considered in this study are equal to zero. The loss assessment platform is not able to fit an appropriate lognormal curve to the residual drifts associated with these motions and as a result, unreasonably high residual drifts would appear in Monte Carlo realizations. The same problem exists if the residual drift ratios are very low. Therefore, wherever the residual drifts are equal to zero or are lower than 1e-3, their value is artificially changed to 1e-3 to obtain a better match between the mean or median of residual drifts obtained from Monte Carlo simulations and those obtained from the structural analysis results. For example, after adjusting the low residual drift ratios, the resultant mean and median of maximum residual drift ratios from Monte Carlo simulations are 0.18 and 0.23% which are close enough to the 0.2% mean of maximum residual drift ratio obtained from time-history analysis. Note that FEMA P-58 loss assessment methodology only requires the maximum residual drift ratio across all stories in the building. The distribution of residual drifts from Monte Carlo simulations and time-history analysis for 2475-year motions are compared in Figure 6.2. For both time-history analysis and Monte Carlo simulations the majority of cases have residual drift values close to 0.1% which is used to replace small residual drifts. While the median of the residual drift ratio distributions for time-history analysis and Monte Carlo simulations are close to each other, a few of the Monte Carlo realizations (30 out of 2000) have a residual drift ratio greater than 1% which are considered as irreparable realizations.

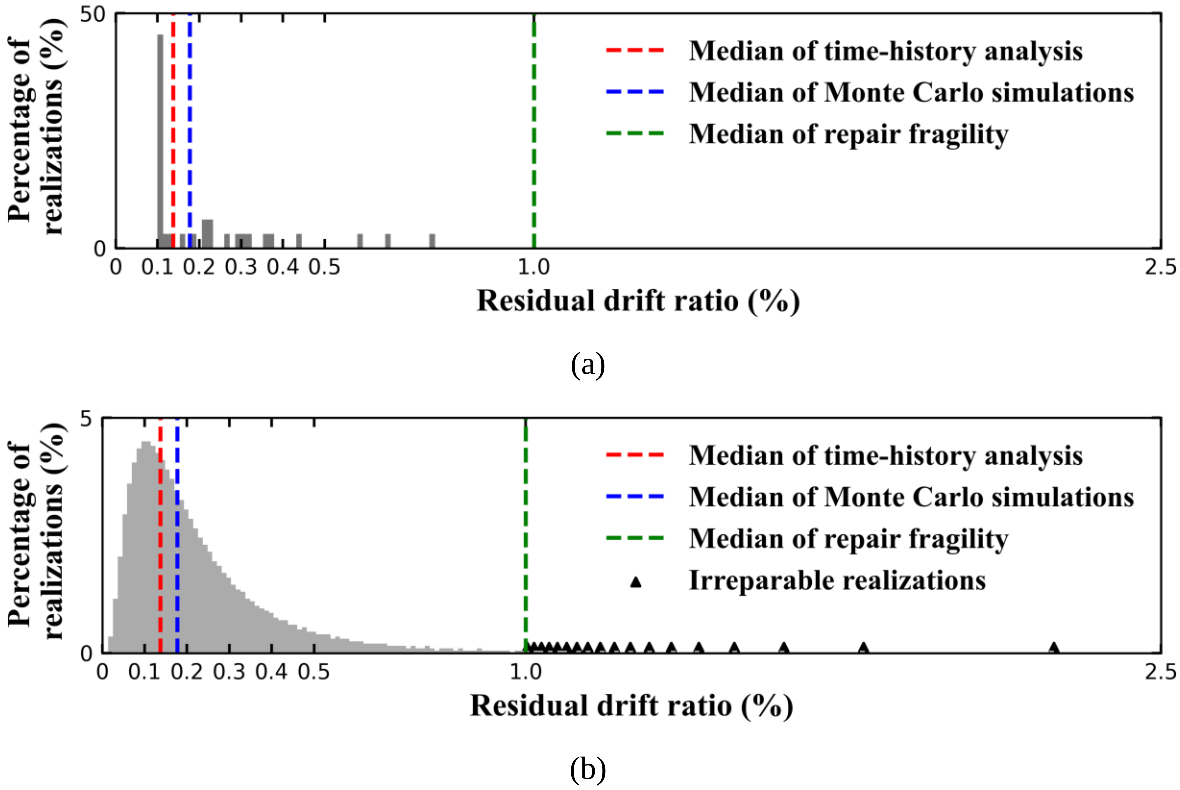

Figure 6.2. Residual drift ratio histograms for 2475-year motions obtained from: (a) time-history analysis; (b) Monte Carlo simulation.

6.2 Loss Assessment Results

Figure 6.3 presents the mean loss ratio of different hazard levels considered in the intensity-based assessment and different sites considered in the scenario-based assessment. As seen in Figure 6.3, the earthquake-induced economic loss associated with the M9 motions increases as the basin depth increases. West Vancouver, which is located outside the basin, has the lowest mean loss ratio (1.4%) while Delta, with the highest basin depth, has a mean loss ratio of 32%. The mean loss ratio of the 2015 NSHM motions vary from 0.7% to 14%, which are associated with the 100- and 2475-year hazard levels, respectively. Note that the mean loss ratio in Delta and Richmond exceed that of 2475-year motions and the mean loss ratios in Burnaby, New Westminster, and Surrey are greater than that of the 975-year motions. Among the different sites considered in the scenario-based assessment, only West Vancouver has a lower economic loss than the 475-year motions.

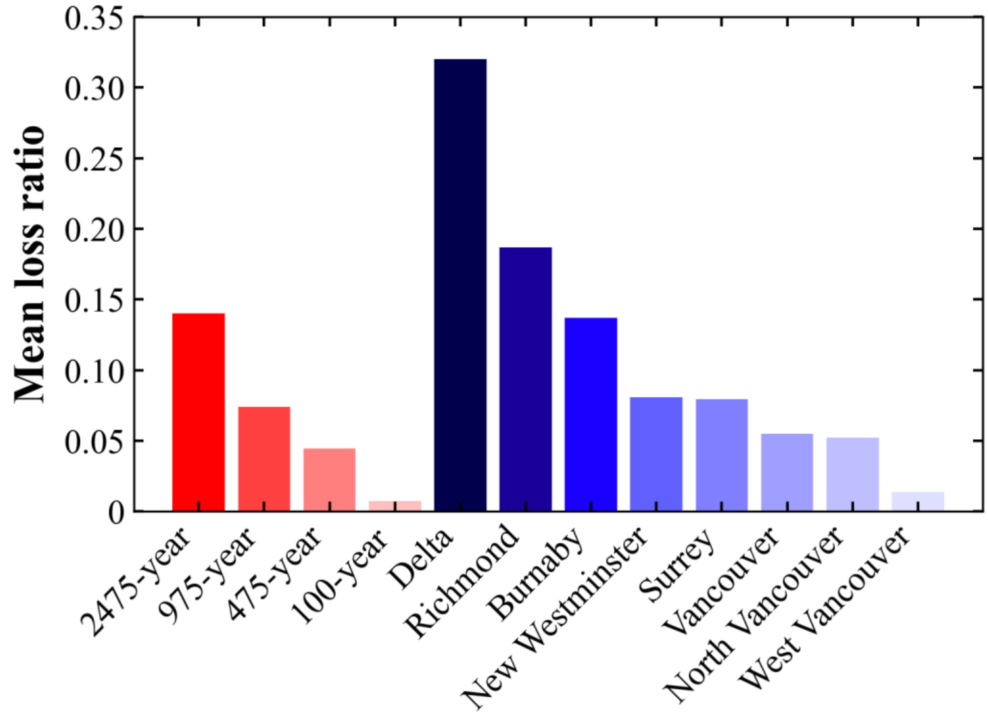

Figure 6.3. Mean loss ratio for the intensity- and scenario-based assessments.

A better representation of the loss distribution of Monte Carlo realizations for each location and hazard level is provided by means of histograms in Figure 6.4. The corresponding mean loss ratios are also plotted. As Figure 6.4 depicts, due to the presence of irreparable cases in 2475-year motions, the mean loss ratio is higher than the median loss ratio. The discrepancies between the median and the mean loss ratios are more significant in Delta, Richmond, and Burnaby where the number of irreparable and collapse cases are higher than in other locations.

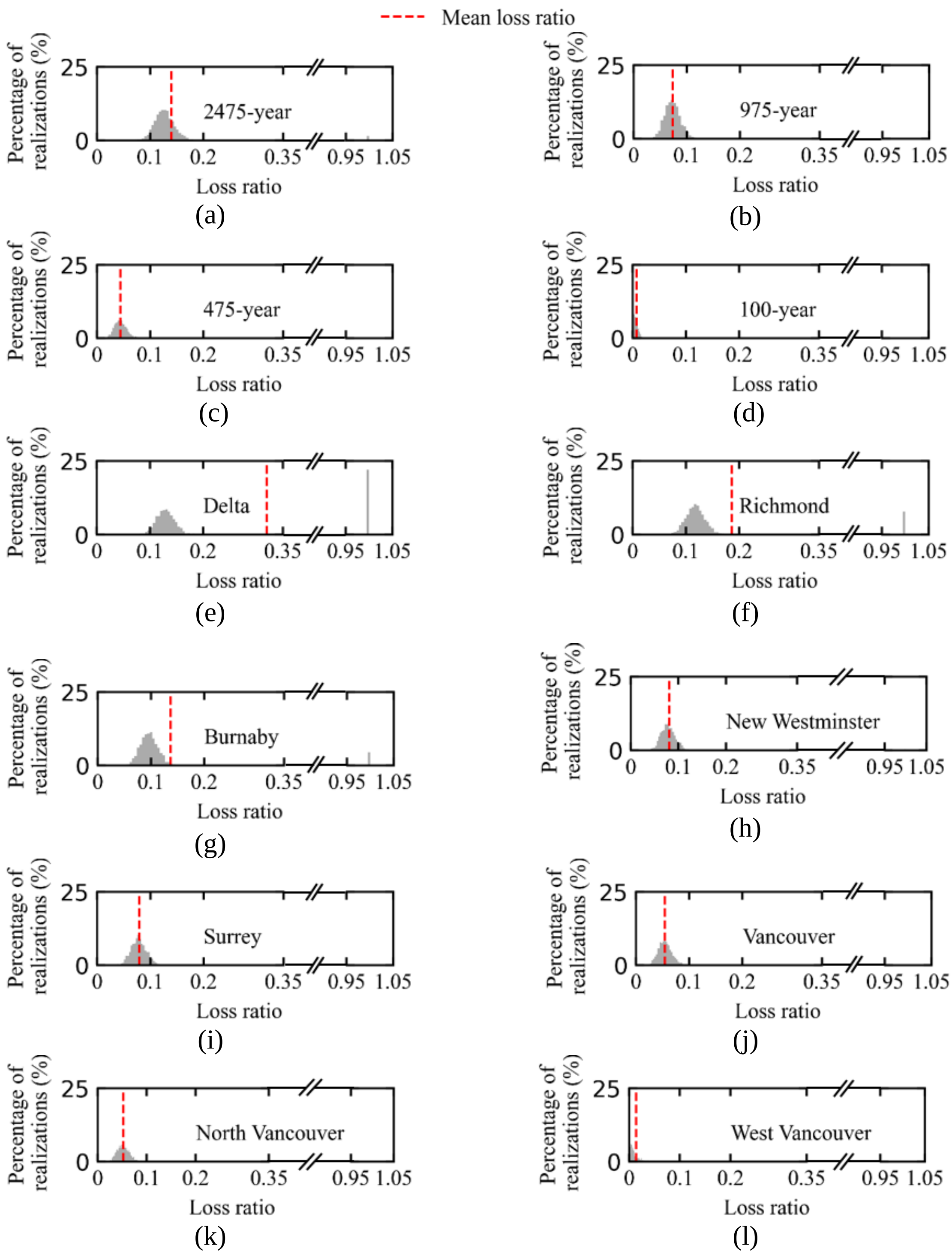

Figure 6.4. Variation of loss ratio for intensity-based assessments with (a) 2475-year; (b) 975-year; (c) 475-year; (d) 100-year return periods and scenario-based assessments at (e) Delta; (f) Richmond; (g) Burnaby; (h) Surrey; (i) New Westminster; (j) Vancouver; (k) North Vancouver; (l) West Vancouver.

Figure 6.5 represent the percentage of collapse, irreparable, and repairable realizations for all sites included in the scenario-based assessments, as well as all hazard levels considered in the intensity-based assessments. The collapse occurrences are observed in Delta, Richmond, and Burnaby with percentage of realizations equal to the collapse probabilities obtained from the time-history analysis as outlined in Table 6.2.

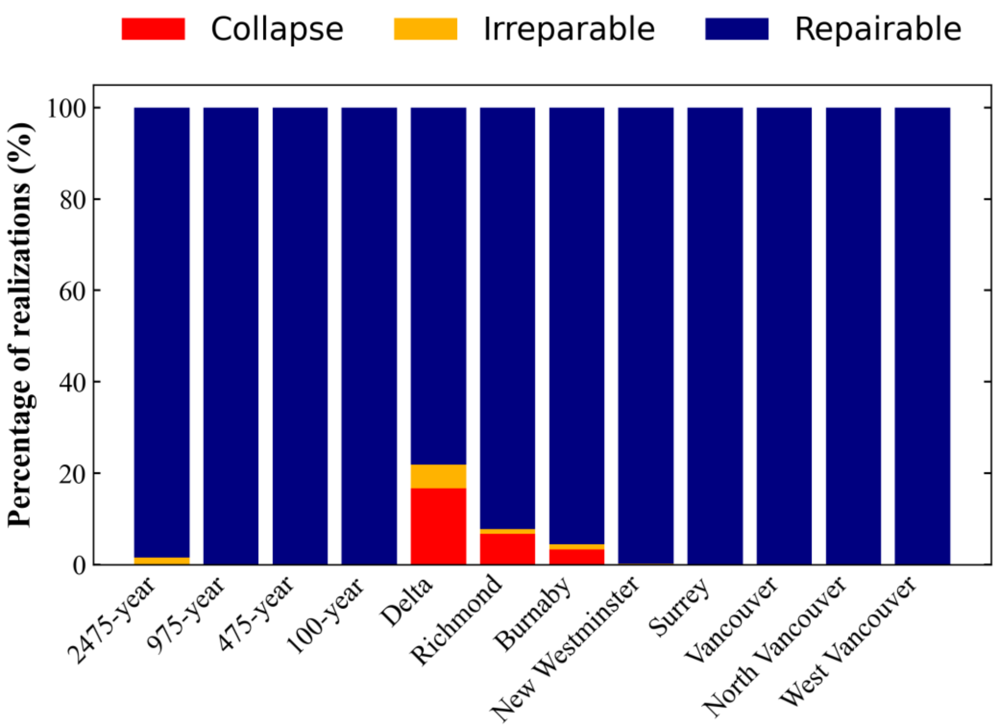

Figure 6.5. Percentage of collapse, irreparable, and repairable realizations for the intensity- and scenario-based assessments.

Figure 6.6 represents the breakdown of the mean loss ratios across all sites in Metro Vancouver for the scenario- and intensity-based assessments. As shown in Figure 6.6, four major contributors to the economic loss are collapse, irreparable damage, repairable structural damage, and repairable non-structural damage. The contribution of collapse to the mean loss ratio of the scenario-based assessments in Delta, Richmond, and Burnaby is significant. However, collapse does not contribute to the economic loss in other locations or in any of the hazard levels. Other than in the 2475-year hazard level, the irreparable structural damage has no contribution to the economic loss in the NSHM 2015 motions. Most of the irreparable damage contribution across the sites considered in the scenario-based assessment is found in Delta due to its higher residual drift ratios.

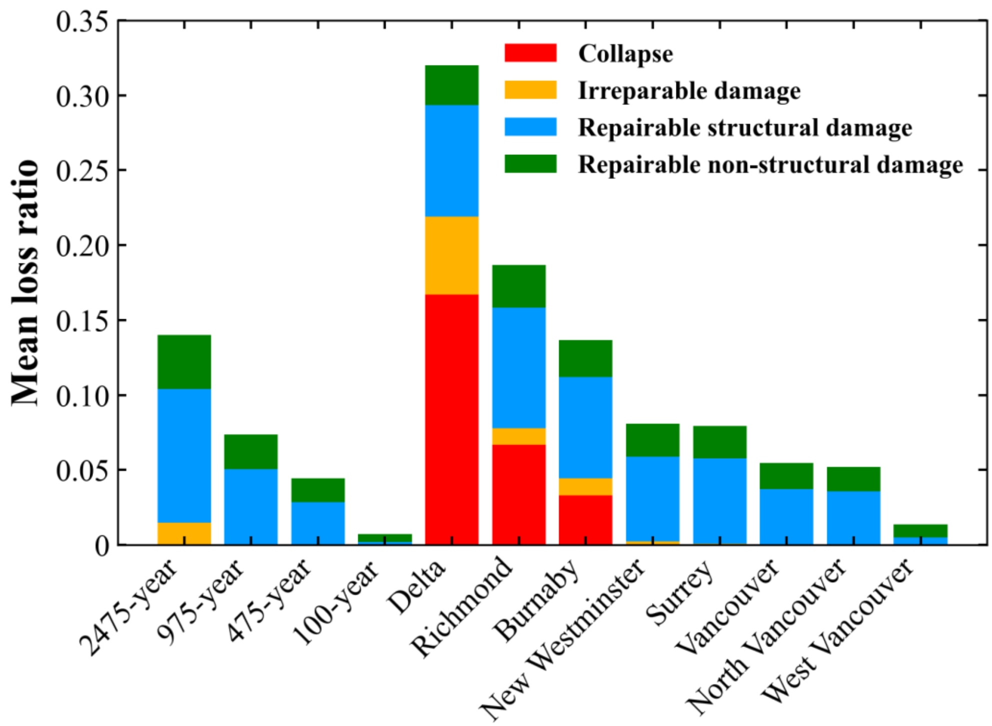

Figure 6.6. Loss deaggregation for the intensity- and scenario-based assessments.

The mean loss ratio is plotted as a function of the return period for intensity-based assessment and as a function of depth to shear wave velocity of 2.5 km/s, $Z_{2.5}$, for scenario-based assessment in Figure 6.7. The variation of each loss contributor is also determined in Figure 6.7. In the intensity-based assessments, collapse and irreparable damage contributions to loss tend to increase as the return period increases for the 2015 NSHM motions. In the scenario-based assessment, these losses increase with increasing $Z_{2.5}$ values. However, the contribution of structural and non-structural repairable damage to the total loss ratio (i.e., the ratio of the loss associated with the structural and non-structural components to the total loss) follows the opposite trend. The portion of repairable damage attributed to structural components decreases as the intensity levels and basin depths decrease due to lower structural responses in lower return periods and basin depths. Consequently, the contribution of non-structural components to the loss is higher in lower return periods and basin depths. The only exception to the mentioned trends is Burnaby, where the structural responses and loss values are higher than Surrey and New Westminster, despite its shallower basin depth. Note that the linear interpolation of data points in Figure 6.7 may not be accurate for return periods and values of depth to shear wave velocity of 2.5 km/s not considered in the assessment.

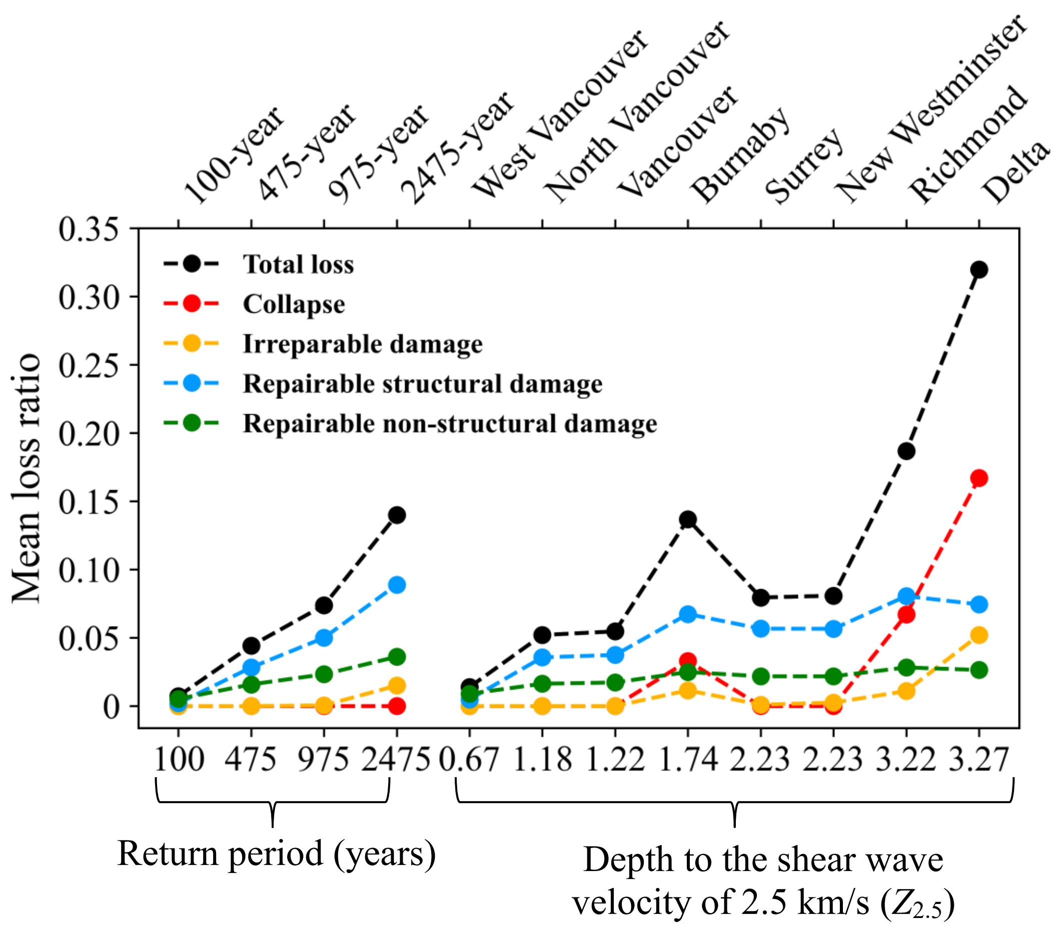

Figure 6.7. Loss vulnerability function for the intensity- and scenario-based assessments.

Figure 6.8 illustrates the repairable loss deaggregation to different structural and non-structural components. Among the scenario-based assessments, the repairable loss associated with structural components is higher than that of non-structural components except in West Vancouver. Similarly, except for the 100-year motions, the loss ratio associated with repairable structural components is greater than non-structural components in the intensity-based assessments.

Figure 6.8 shows that most of the repairable structural damage is associated with the slab-column connections. Slab-column connections have higher contribution to the economic loss ratio in sites with deeper basins in the scenario-based assessment, and in ground motions with higher return periods in the intensity-based assessment. This is due to higher racking drift ratios that the archetypes experience, and the resulting connection damage. The contribution of shear wall damage to the economic loss ratio is almost negligible even in locations with deep basins and at high intensity levels. This is because the use of damageable wall drift ratio to measure the damage to the shear walls results in drift ratios considerably lower than those indicated in the FEMA P-58 fragility functions for slender shear walls. For example, as shown in Figure 5.8, the maximum of the mean damageable wall drift ratios at Delta in the scenario-based assessment is less than 0.9%. This value is lower than the median values of the lognormal distributions that characterize the FEMA P-58 fragility functions for slender concrete walls (i.e., fragility ID “B1044.101”) which are 0.93%, 1.28%, and 1.86% for damage states 1, 2, and 3, respectively. Therefore, most of the shear walls have a damage state of 0 and the economic loss ratios associated with these elements is negligible. Note that the maximum of the mean of steel and concrete strains in Delta are 1.6% and 0.12%, respectively and spalling of the cover and yielding of the concentrated steel bars happen at these strain levels. These values are recorded at grade level where the highest damageable wall drift is observed (compare Figure 5.12 and Figure 5.14 with Figure 5.8).

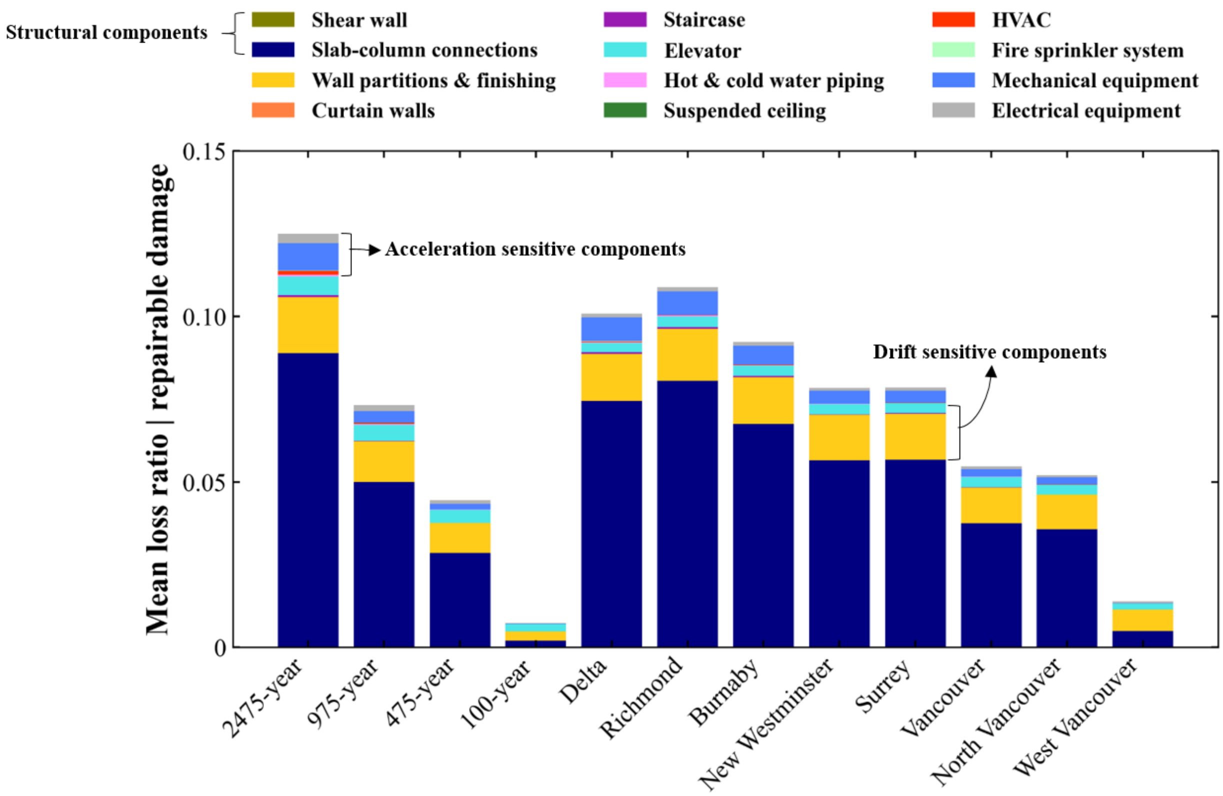

Figure 6.8. Repairable loss deaggregation for the intensity- and scenario-based assessments.

Additionally, Figure 6.8 demonstrates that most of the repairable non-structural damage is associated with the wall partitions. Similar to the slab-column connections, the damage to the wall partitions is measured by racking drift ratio and therefore, the trends of the loss associated with these components are similar to those of the slab-column connections for both types of assessment. The curtain walls and the stair cases are other drift sensitive components which do not significantly contribute to the economic loss of the archetypes. The damage to the elevators is measured using two EDPs: one is the residual drift ratio which is used to estimate the damage to the elevator guide rail system and the other is the peak floor acceleration which measures damage to the traction elevator cabin. In most of the assessments, the cost associated with the damage to the elevator guide rail system (which is measured by residual drift) is more significant than that of the traction elevator cabin and therefore, the elevator is considered a drift-sensitive component in Figure 6.8. Among the acceleration sensitive components, the damage to the mechanical equipment is the most significant. Overall, the drift sensitive components have higher contribution to repairable economic loss than acceleration sensitive components as shown in Figure 6.8.

The findings of this chapter can be summarized as follows:

- The variation of the economic loss at different locations across Metro Vancouver is significant under simulated ground motions of M9 CSZ earthquakes. For example, the loss ratios associated with Delta, Richmond, and West Vancouver are 1.4%, 18.7%, and 32%, respectively.

- In the scenario-based assessments, higher mean loss ratios are observed at deeper basins. Therefore, the highest and lowest mean loss ratios are associated with Delta and West Vancouver.

- The mean loss ratio of the scenario-based assessments at deep basins (i.e., Delta (i.e., 32%) and Richmond (i.e., 18.7%)) exceed those of the 2475-year return period intensity-based assessment (i.e., 14%). Also, the mean loss ratios of the M9 motions are higher than the 475-year motions (i.e., 4.4%) at all locations except West Vancouver, which is located outside the basin.

- Loss deaggregation indicates that collapse is the main contributor to the economic loss in Delta under M9 motions and repairable structural damage is the main contributor to loss at other locations except West Vancouver, where the repairable non-structural damage has the highest loss contribution. Similarly, repairable non-structural damage contributes more than other factors to the economic loss under the 100-year motions while for other return periods considered in the intensity-based assessments, the main contributor to the economic loss is repairable structural damage.

- Repairable loss deaggregation indicates that the majority of the repairable structural loss is attributed to the slab-column connections damage. Strengthening such components can reduce the economic loss significantly. Among the non-structural components, the contributions of wall partitions, mechanical equipment, and elevators to the economic loss are the most significant.

Chapter 7: Downtime Assessment

This chapter presents the details of downtime evaluation of the modern residential tall RCSW buildings located in Metro Vancouver. This study on downtime followed the framework developed by Molina Hutt et al. (2022). A detailed overview of the methodology is provided in Section 2.7.2. While this framework provides downtime to five recovery states (i.e., stability, shelter-in-place, reoccupancy, functional recovery, and full recovery), the focus of this study is on shelter-in-place, reoccupancy, and functional recovery. Other than the downtime to each recovery state, recovery trajectories are provided and the rapidity and robustness performance metrics are evaluated. In addition, a deaggregation of results is included to highlight the most important downtime contributors.

Consistent with Molina Hutt et al. (2022), the reconstruction time of the archetype buildings in this study are obtained assuming that construction of each story takes 14 days. This results in a total of 462 days reconstruction time for the 33-story building archetypes. In addition, the median building demolition time is 445 days (Molina Hutt et al., 2022) and therefore, the resultant total building replacement time is 907 days. Similar to Molina Hutt et al. (2022), the impeding factor delays associated with each repair path are categorized by contractor mobilization, stabilization, engineering and permitting, and financing. Note that this study assumes that the financing coefficients introduced by Molina Hutt et al. (2022) for Seattle are valid for Metro Vancouver and thus, the financing coefficients for insurance, private loans, and public loans are 0.16, 0.72, and 0.12, respectively.

7.1 Downtime to Different Recovery States

The median downtime to achieve Functional Recovery (FR), Reoccupancy (RO), and Shelter-in-Place (SiP) recovery states are shown in Figure 7.1 for the intensity- and scenario -based assessments. Figure 7.1 shows that the downtime to all three recovery states is higher in locations with deeper basins. For example, the median functional recovery time in Delta, the deepest basin site, is 543 days while the median functional recovery time in West Vancouver, which is located outside the basin, is 175 days. The downtime to all three recovery states is greater under higher hazard levels. For instance, the downtime to the shelter-in-place recovery state is 394 days for the 2475-year hazard level, and 6 days for the 100-year hazard level.

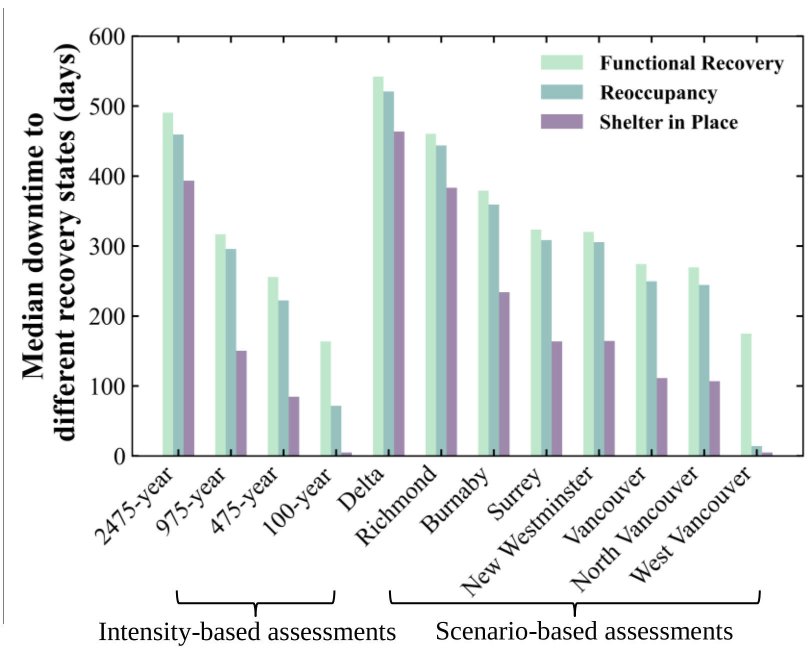

Figure 7.1. Downtime to different recovery states for the median realization of the intensity- and scenario-based assessments.

A comparison of the intensity- and scenario-based assessments highlight the impact of basin effects on downtime. As seen in Figure 7.1, the downtime to all recovery states is greater for the 2475-year hazard level than the scenario-based assessments in all locations except Delta with the highest basin depth. For example, the functional recovery time of the 2475-year and the scenario-based assessment in Delta are 491 and 543 days, respectively. The significance of basin effects is further highlighted by comparing the downtimes associated with the 475-year event with the scenario-based assessments. While the return periods of the M9 motions are close to 475 years, the functional recovery time under an M9 event in Delta (i.e., 543 days) is roughly twice of that under a 475-year hazard level. Similarly, due to basin amplifications, the downtime of the scenario-based assessments in all locations except West Vancouver (located outside the basin) is higher than that of the 475-year hazard level.

The additional downtime required to progress from one recovery state to the next is considerably less in deep basin sites (e.g., Delta and Richmond), and at high shaking intensities (e.g., 2475-year motions) compared to shallow basin sites (e.g., West Vancouver) and lower intensities (e.g., 100-year motions). For instance, in the scenario-based assessments, the building archetype in Richmond has a SiP downtime of 384 days and requires 77 additional days to achieve FR. By contrast, in West Vancouver, the SiP downtime is only 6 days and 169 more days are required to achieve FR. This effect can be explained by the governing repair path in each recovery state. In deep basins and under high intensity levels due to high damage to the structural components, repair path A governs the downtime to all three recovery states. In contrast, in shallow basins and under low intensity levels, different factors govern the downtime to different recovery states. For example, for the median realization of the scenario-based assessment in West Vancouver, while elevator repair governs the functional recovery time, it is not required for the SiP and RO recovery states. Due to low seismic damage, other components do not hinder achieving these two recovery states, hence, the building achieves SiP and RO immediately after inspection, while 169 additional days are needed for elevator repairs in order to achieve the functional recovery state. By contrast, in Delta, structural damage is significant to the point that it hinders all three recovery states and therefore, the additional downtime required to progress from one recovery state to the next is lower.

As described in Molina Hutt et al. (2022), the relationship between economic loss and downtime is not one-to-one. For example, for the 2475-year assessment, the downtime to all recovery states is greater than that of the scenario-based assessments in Burnaby and Richmond. The opposite trend is observed for loss assessment as shown in Figure 6.3 (i.e., the loss ratio of the 2475-year motion is lower than that of the scenario-based assessments in Burnaby and Richmond). One reason is that despite low loss levels, downtime estimates (in particular functional recovery time), are considerable (compared to the replacement time) for many of the realizations and this reduces the effect of collapse realizations on downtime.

For each intensity- and scenario-based assessment, the downtime to achieve each recovery state for the median realization is summarized in Table 7.1. The functional recovery times for the 2475- and 475-year hazard levels are 491 and 256 days, respectively. These numbers are comparable with other studies such as that conducted by Molina Hutt et al. (2021) on a 42-story residential RCSW building archetype located in San Francisco, CA (Site Class D), where the functional recovery times were 512 and 222 days under the 2475- and 475-year hazard levels, respectively.

Table 7.1. Median downtime realization to different recovery states (shelter-in-place, reoccupancy, and functional recovery) under the scenario and intensity-based assessments.

Type of assessment	Ground motion	Downtime to achieve each recovery state (days)*		
		Shelter-in-place	Reoccupancy	Functional recovery
Intensity-based	2475-year	394	460	491
	975-year	151	296	317
	475-year	85	223	256
	100-year	6	72	164
Scenario-based	Delta	464	521	543
	Richmond	384	444	461
	Burnaby	234	360	380
	New Westminster	165	306	321
	Surrey	164	309	324
	Vancouver	112	250	275
	North Vancouver	107	245	270
	West Vancouver	6	15	175

* Note that the building replacement time is equal to 907 days.

Table 7.1 shows that for the scenario-based assessments in Delta and Richmond, and for the 2475-year motions, the median downtime to functional recovery is greater than 50% of the median building replacement time (i.e., 907 days). Note that for the 2475-year shaking intensity, which is currently used to design buildings in Metro Vancouver, the mean loss ratio is less than 15% which is considered a moderate loss ratio (Molina Hutt et al., 2021). Therefore, while the building archetypes meet the requirements of current design provisions as shown in Chapter 5 of this study and the mean loss ratio is moderate (Molina Hutt et al., 2021), the functional recovery time is significant and may warrant explicit consideration in future design standards.

7.2 Downtime Trajectory

Downtime trajectories determine the changes in building usability (i.e., the ratio of number of repaired stories to total number of stories) after the earthquake. These plots visualize trajectories of all four repair paths and the governing repair path. In addition, they present the inspection time, impeding factor delays, and utility repair time. As mentioned earlier, for a non-collapse realization, the repair time for each repair path is sum of inspection, maximum of impeding factor delays (engineering and permitting, financing, contractor mobilization, and stabilization), and building components repair time. The governing repair path is the maximum repair time of the four repair paths.

A detailed functional recovery downtime trajectory of the median realization for the scenario-based assessment in New Westminster is illustrated in Figure 7.2. The horizontal bar plots on the left side of the figure show the inspection time, impeding factor delays, as well as utility repair time. The numbers in round brackets, ( ), indicate the durations of the impeding factors and the letters in square brackets, [ ], indicate the repair paths affected by each impeding factor delay. For example, the inspection time is 6 days and it affects all repair paths (A, B, C, and D). Note that the time required for inspection, financing, engineering and permitting, and stabilization is the same among all repair paths. However, the contractor mobilization time depends on the components which are repaired in the repair path considered and therefore, this impeding factor delay is different across each repair path. For each repair path, the governing impeding factor delay is the maximum of the time required for engineering and permitting, financing, contractor mobilization, , and stabilization. For example, based on Figure 7.2, the governing impeding factor delay for repair path C (Elevator repair) is 212 days and corresponds to a contractor mobilization delay. Note that the building usability increases only after the inspection time, impeding factor delays, and the repairs up to the first floor are complete as shown in Figure 7.2 for repair path C. As seen in the figure, the elevator repairs (repair path C) start 218 days after the earthquake due to the time required for inspection (6 days) and contractor mobilization (212 days) which is the governing impeding factor, and other repairs up to the first floor (0 days in this case).

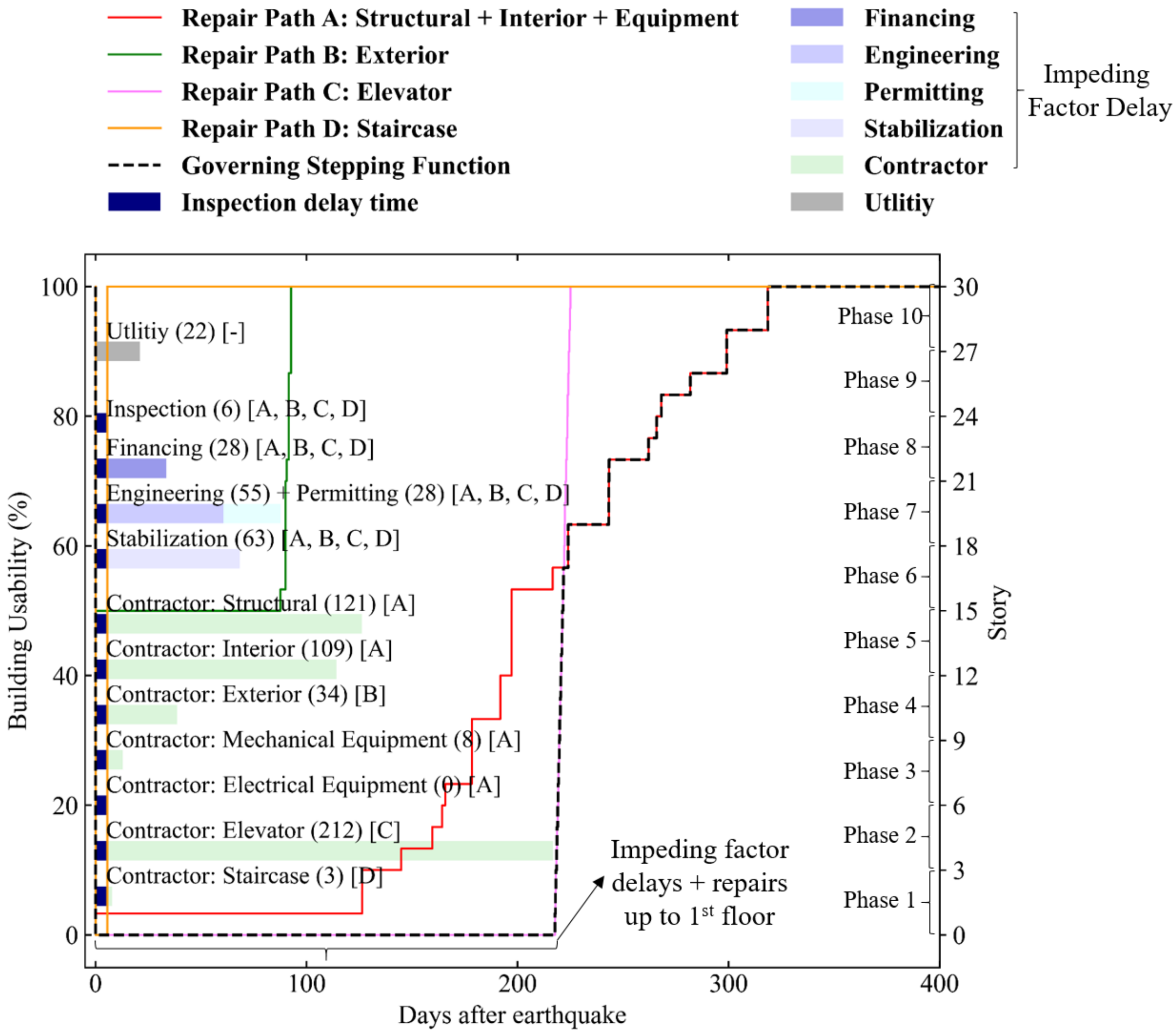

Figure 7.2. Recovery trajectories for each repair path to functional recovery of the median realization of the scenario-based assessment in New Westminster. Numbers in round brackets, ( ), indicate the duration of the impeding factor. The letter in square brackets, [ ], indicate the repair paths affected by each impeding factor delay.

In each repair path, after determining the impeding delays, the components repair time calculation starts and the building usability increases as repairs in each story are complete. As seen in Figure 7.2, the building usability for repair path D (staircase repairs) is 100% right after the inspection which indicates there is no staircase damage. As a result, after the inspection time (i.e., 6 days), the usability jumps to 100%. For repair path B (exterior repairs), no repair is required below level 16 and thus, building usability does not drop to zero after the earthquake. The impeding factor delays are 88 days and the components repair time is only 6 days. Therefore, after 94 days the repair path B achieves 100% usability. Repair path C (elevator repairs) has impeding delays and components repair time of 218 and 6 days, respectively. Consequently, the total time to achieve 100% usability for repair path C is 226 days. This repair path is the governing (longest) repair path up to a building usability of 56.67%. Note that the building usability in repair path C increases with equal steps (i.e., without any major jumps) from the first story up to story 30. Repair path A (structural, interior, and equipment repairs) is the governing repair path above a usability of 56.67%. For this repair path, the initial building usability after the earthquake is 3.33% as no repair is required in the first level. The impeding delays and component repair time are 127 and 194 days, respectively which results in a time of 321 days to achieve 100% usability. Note that within repair phase *j* in repair path *i*, whenever the repair time of the upper story *n* is less than that of the lower story *n*-1, then the repairs of story *n* would be completed by the time repairs of story *n*-1 are completed and therefore, the building usability jumps multiple stories. For example, in repair phase 10 (stories 28 to 30) of repair path A, as seen in Figure 7.2, the repair time of story 30 is greater than that of story 29. Hence, there are no intermediate steps in the repair path trajectory between these two stories.

The utility repair time which includes natural gas, water and electrical systems is also provided atop in Figure 7.2. While these services are necessary to achieve functional recovery; the utility restoration time is generally considerably lower than other delays/repairs and does not generally govern the downtime to functional recovery. For example, based on Figure 7.2, the utility repair time is only 22 days which is considerably lower than the impeding delay for repair path C (i.e., 218 days).

The trajectory of the downtime to functional recovery and shelter-in-place recovery states are plotted for the median realization of the intensity- and scenario-based assessments in Figure 7.3.

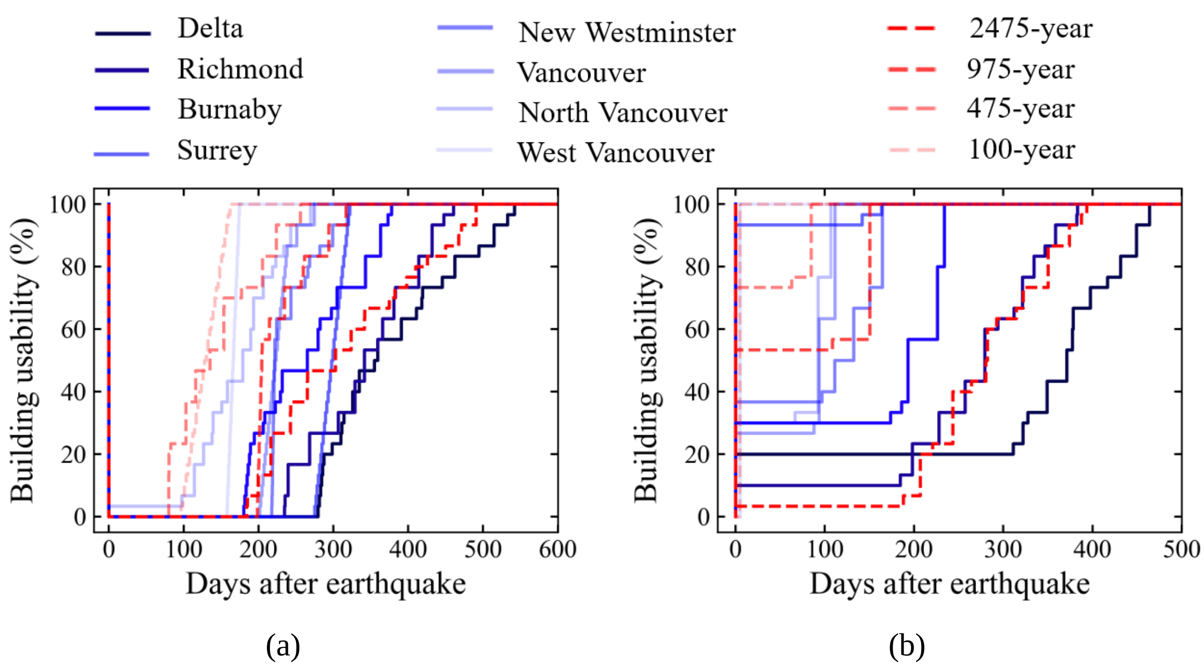

Figure 7.3. Recovery trajectories to (a) functional recovery; and (b) shelter-in-place recovery states for the median realization of the intensity- and scenario-based assessments.

Figure 7.3a demonstrates that the recovery time and trajectory vary depending on the target building usability, the location within the basin, and the shaking intensity. For instance, the functional recovery downtime to achieve a building usability of 70% is higher in the scenario-based assessment in Richmond than for the 2475-year motions. However, the downtime to achieve 100% building usability is higher for 2475-year motions than in Richmond.

Figure 7.3b shows that the building usability is usually greater than zero immediately after inspection for the SiP recovery state. The sheltering capacity is provided immediately after inspection for 100-year motions and the scenario-based assessment in West Vancouver as seen in Figure 7.3b.

The recovery trajectories to functional recovery are plotted for all realizations of the intensity- and scenario-based assessments in Figure 7.4 along with the median, 10^{th} and 90^{th} percentile realizations. The large uncertainty associated with downtime estimates is highlighted the figure. The median, 10^{th} and 90^{th} percentile realizations, are determined considering the time required to achieve 100% building usability; therefore, the time to achieve other values of building usability can be higher in the 10^{th} percentile realization than the median realization (e.g. Figure 7.4e).

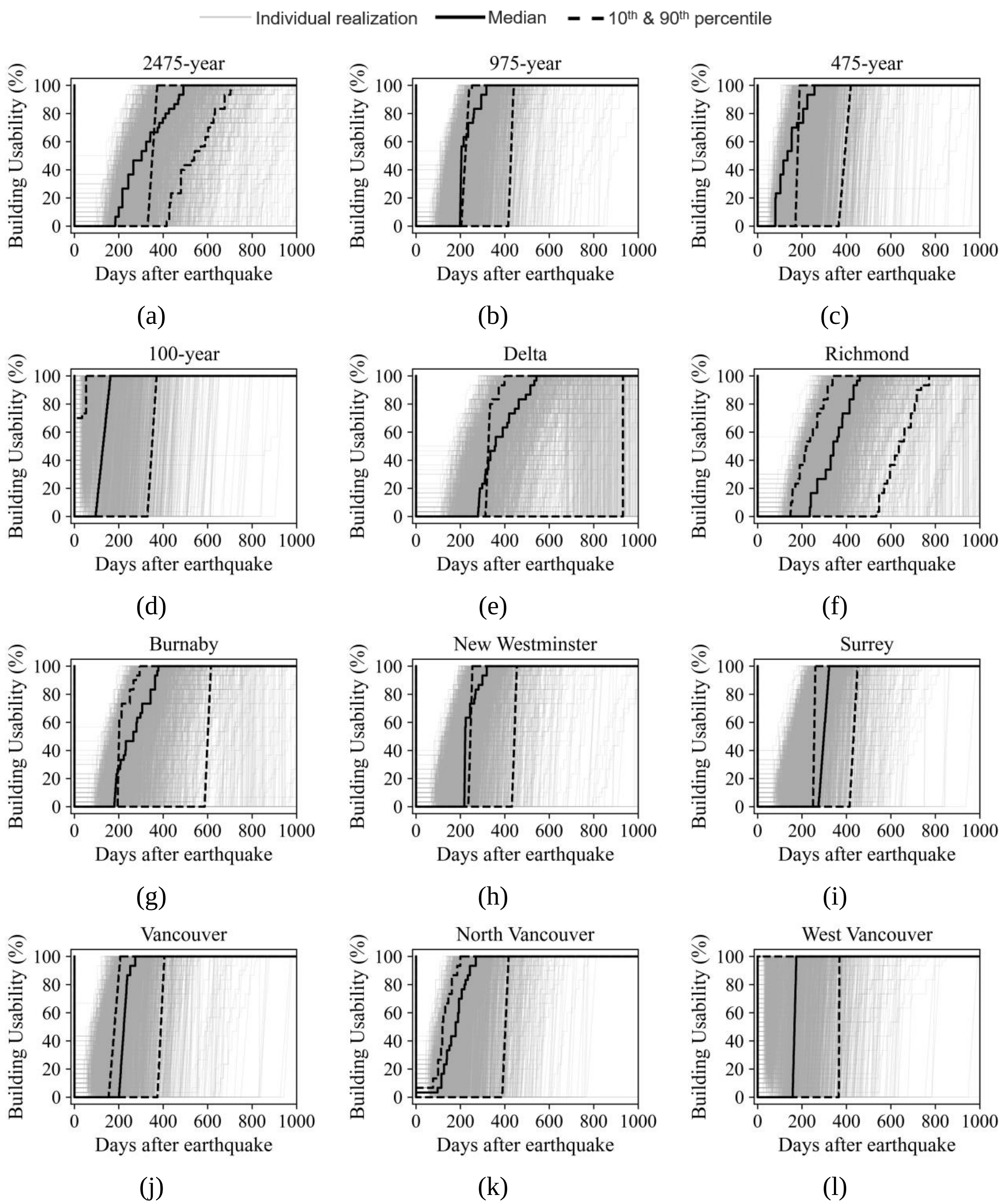

Figure 7.4. Recovery trajectories to functional recovery state for all realizations of the intensity-based assessments with (a) 100-year; (b) 475-year; (c) 975-year; (d) 2475-year return periods and scenario-based assessments in (e) Delta; (f) Richmond; (g) Burnaby; (h) Surrey; (i) New Westminster; (j) Vancouver; (k) North Vancouver; (l) West Vancouver.

The distribution of downtime to functional recovery can be captured better by means of histograms. Figure 7.5 provides histograms of downtime to functional recovery for all realizations of both intensity- and scenario-based assessments. Red numbers in Figure 7.5 are the median downtimes to functional recovery. Figure 7.5 demonstrates that the dispersion of downtime in Delta, Richmond, and West Vancouver in the scenario-based assessment and for the 100- and 2475-year motions is considerably higher than other locations and intensity levels. The tails of the downtime distribution in the scenario-based assessments in Delta and Richmond exceed the median building replacement time (i.e. 907 days) which indicates the number of collapse and irreparable damage realizations is larger in these locations compared to other locations in the scenario-based assessments and all hazard levels in the intensity-based assessments.

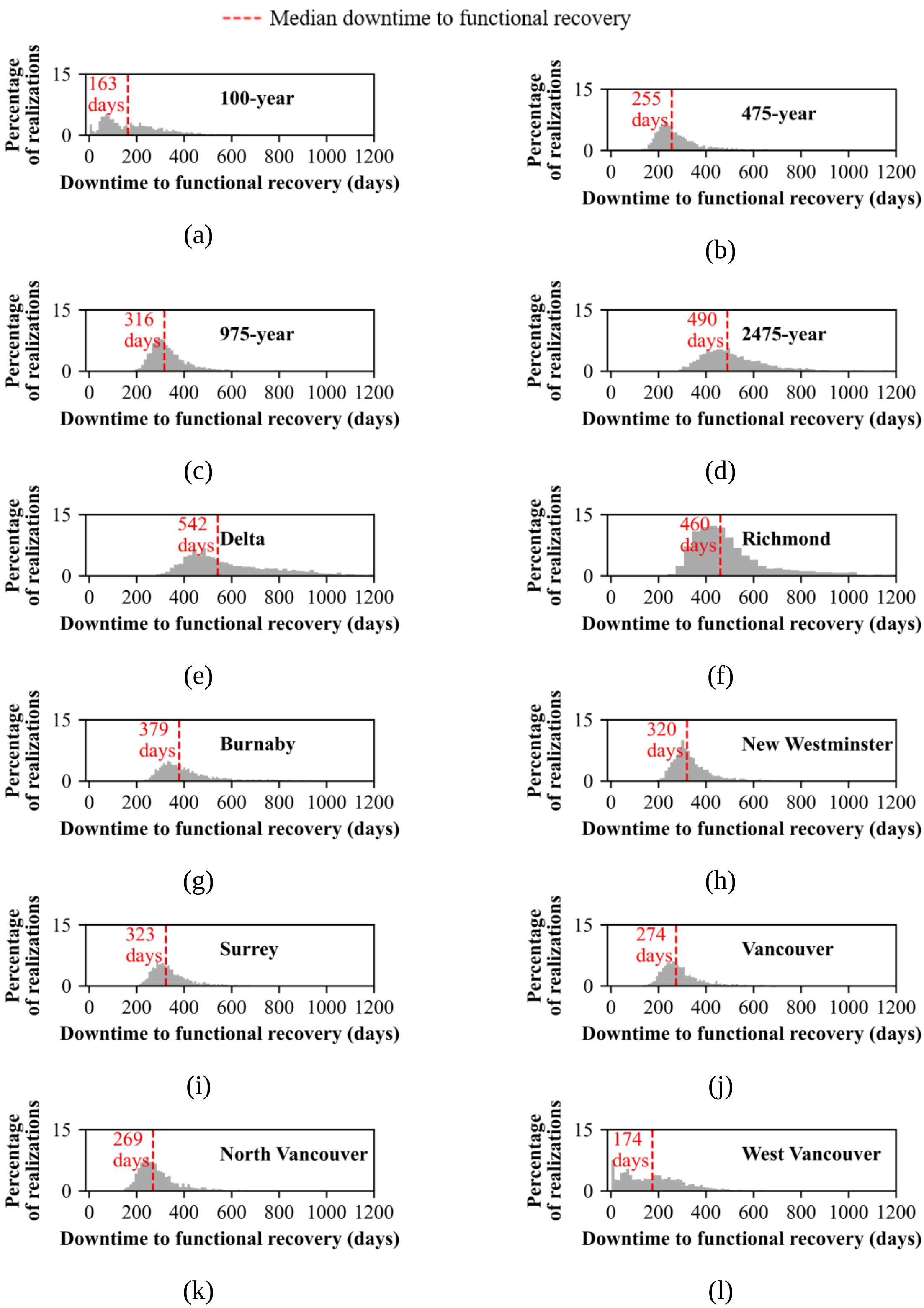

Figure 7.5. Variation of downtime to achieve the functional recovery state for the intensity-based assessments with (a) 2475-year; (b) 975-year; (c) 475-year; (d) 100-year hazard levels and the scenario-based assessments at (e) Delta; (f) Richmond; (g) Burnaby; (h) Surrey; (i) New Westminster; (j) Vancouver; (k) North Vancouver; (l) West Vancouver.

7.3 Robustness and Rapidity

Robustness determines the ability of the building to withstand seismic forces without loss of function (Molina Hutt et al., 2022). The robustness performance metric proposed by Molina Hutt et al. (2022) (Eq. 2.2) is leveraged to determine the post-earthquake usability of the buildings for each of the intensity- and scenario-based assessments.

For all the hazard levels considered in the intensity-based assessment and all the locations considered in the scenario-based assessments, the probabilities of achieving target recovery states of SiP, RO, and FR immediately after the earthquake are shown in Figure 7.6. As shown in Figure 7.6, for the functional-level earthquake, i.e., 475-year motions, the probability of not achieving the expected target recovery state of SiP far exceeds the recommended 10% threshold (Molina Hutt et al., 2022). Therefore, tall residential RCSW buildings designed per current standards in Metro Vancouver do not meet the robustness performance criteria recommended by Molina Hutt et al. (2022).

As shown in Figure 7.6a, the recommended 10% threshold for SiP is achieved only in the scenario-based assessment in West Vancouver and the 100-year event where SiP is hindered in 1% and 2% of the realizations, respectively. The reoccupancy and functional recovery states are hindered in all of the realizations for each location and intensity level except in West Vancouver and 100-year motions.

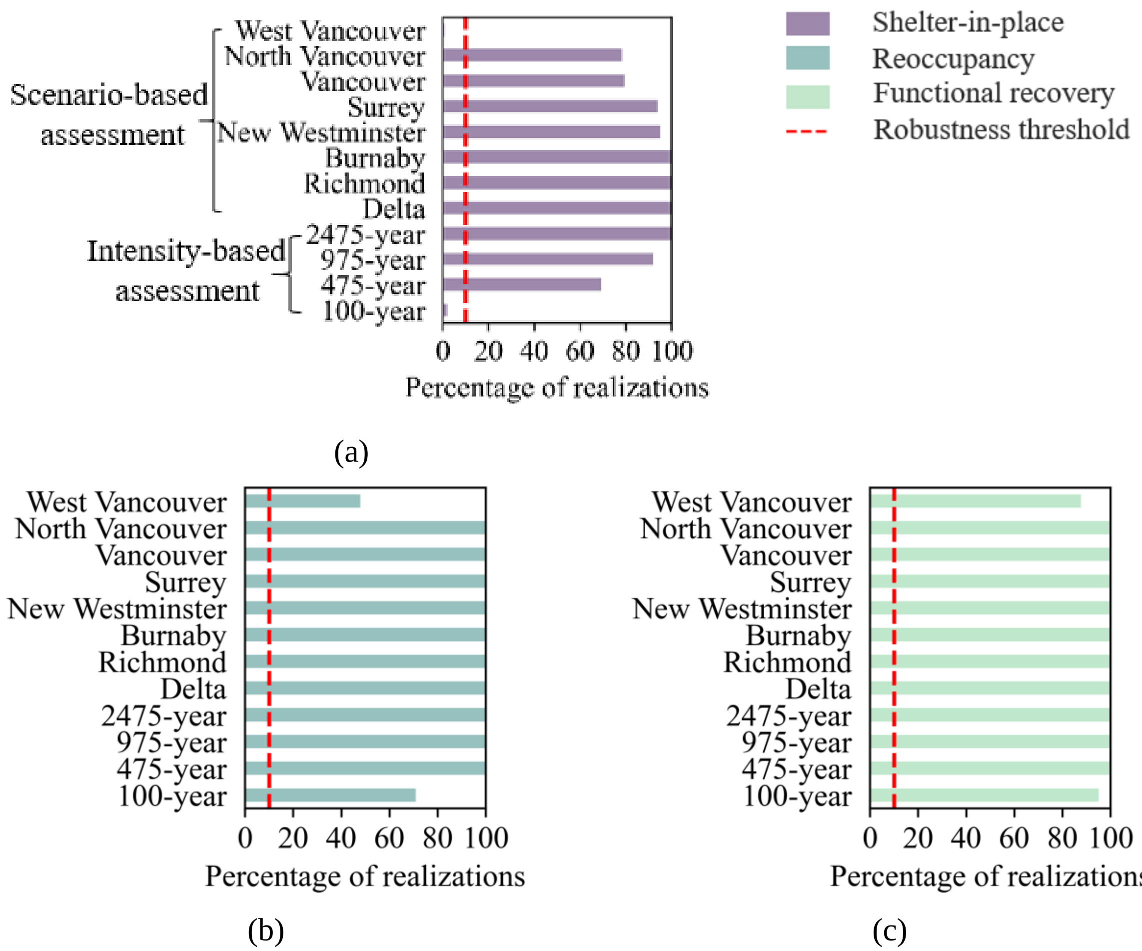

Figure 7.6. Percentage of realizations for where the criticality of the immediate post-earthquake recovery state is greater than that of target recovery state of: (a) shelter-in-place, (b) reoccupancy, and (c) functional recovery for the intensity and scenario-based assessments.

Rapidity determines the ability of the building to meet recovery goals in a timely manner (Molina Hutt et al., 2022). The method proposed by Molina Hutt et al. (2022) (Eq. 2.3) is used to determine how fast the building archetypes achieve different recovery states after the earthquake for each of the intensity- and scenario-based assessments. As recommended by Molina Hutt et al. (2022), the rapidity threshold and target recovery time are set to 10%, and four months, respectively, for the functional recovery state.

The downtime to achieve each recovery state as a percentage of realizations is shown in Figure 7.7 for all intensity- and scenario-based assessments. Note that the rapidity performance measure is not met for the 475-year motions as 100% of the realizations require more than four months to achieve functional recovery. Therefore, tall residential RCSW buildings designed per current standards in Metro Vancouver do not meet the rapidity performance criteria proposed by Molina Hutt et al. (2022).

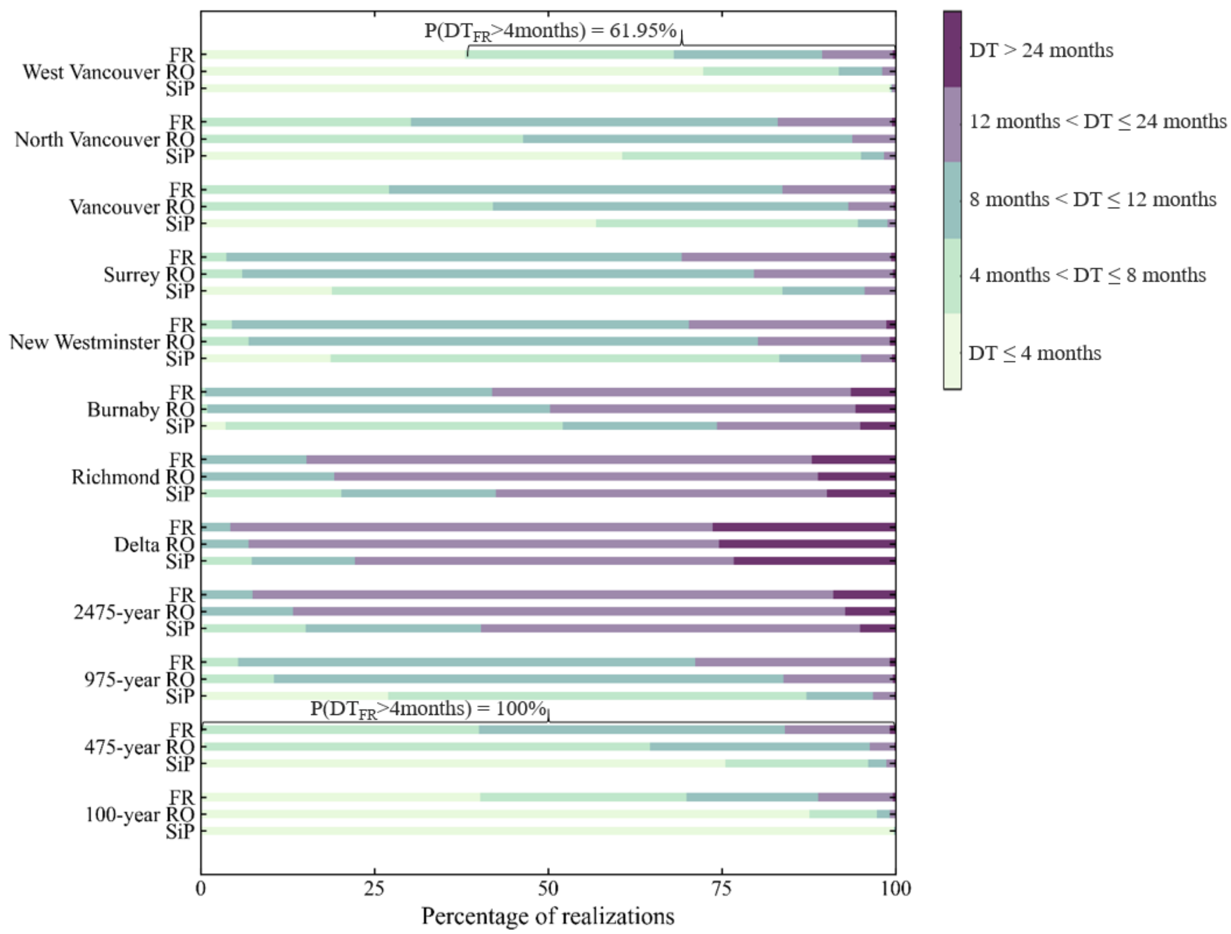

Figure 7.7. Downtime to achieve Functional Recovery (FR), Reoccupancy (RO), and Shelter-in-Place (SiP) recovery states for the intensity- and scenario-based assessments.

The probability of the functional recovery time exceeding four months for all intensities and basin sites is same as that of 475-year motions (i.e., 100%). The only exception are the 100-year motions and the scenario-based assessment in West Vancouver where the probability of the functional recovery time exceeding 4 months are 50.8% and 61.95%, respectively. This shows that even in 100-year and West Vancouver motions, the rapidity performance measure is not met (i.e., the 10% threshold for rapidity is exceeded).

7.4 Downtime Deaggregation

The goal of this section is to provide a deaggregation of downtime to determine the importance of different downtime contributors. Engineers can use the results to develop better design strategies and retrofit solutions.

The contribution of collapse, irreparable damage, and repairable damage to the total downtime to functional recovery for the intensity- and scenario-based assessments are highlighted in Figure 7.8 by means of downtime vulnerability functions where the mean downtime ratio is plotted against return period for intensity-based simulations and depth to soils with shear wave velocity of 2.5 km/s, $Z_{2.5}$, for scenario-based assessments. For all hazard levels and locations, repairable damage is the dominant downtime contributor. Building collapse contributes only to the downtime of the scenario-based assessments in Delta, Richmond, and Burnaby with collapse probabilities of 16.7%, 6.7%, and 3.3%, respectively. The irreparable damage has a negligible (less than 1%) contribution to functional recovery time in all scenario-based assessments except in Delta, Richmond, and Burnaby. Also, the irreparable damage does not contribute to functional recovery time in any of the intensity-based assessments except the 2475-year motions.

These results show that the significance of downtime and loss contributors are not necessarily the same. For instance, while collapse is a major contributor to economic loss in Delta in the scenario-based assessment (see Figure 6.6), its contribution to downtime is less significant. Note that the linear interpolation of data points in Figure 7.8 may not be accurate for return periods and $Z_{2.5}$ values not considered in the assessments.

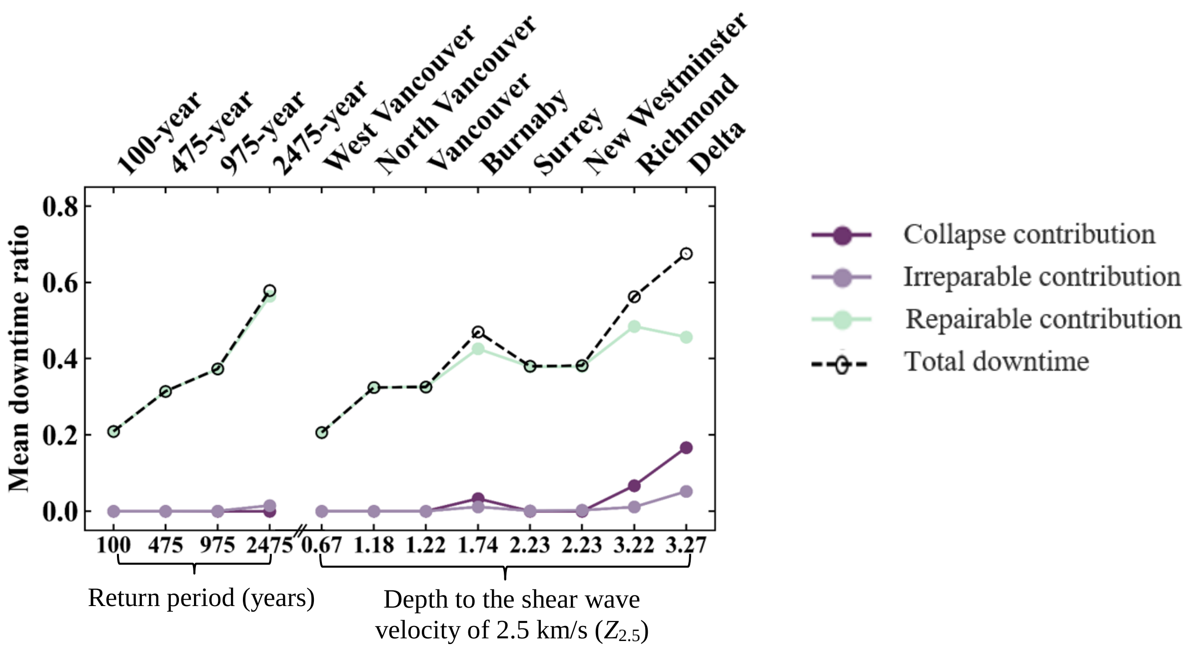

Figure 7.8. Mean downtime to achieve functional recovery state for the intensity- and scenario-based assessments including contributions from collapse, irreparable damage, and repairable damage.

The percentage of repairable realizations (realizations which do not render building collapse or irreparable damage) in which a component hinders achieving a recovery state immediately after an earthquake is shown in Figure 7.9 for Delta, Richmond, and Burnaby in the scenario-based assessments and for 475-, and 2475-year hazard levels in the intensity-based assessments. Using these plots, one can determine the components that require strengthening to help achieve the above mentioned "robustness" performance goal.

As seen in Figure 7.9, damage to the slab-column connections hinder achieving stability immediately after the earthquake in 100% of realizations in Delta, Richmond, and Burnaby, as well as the 2475-year motions. The slab-column connection component does not hinder the stability recovery state immediately after the earthquake in only 31% of the realizations of the 475-year assessment. Therefore, strengthening the slab-column connections is a key strategy to increase the robustness of the archetype buildings. As the damage to the shear walls are low (see Chapter 6), the contribution of shear wall damage to downtime is negligible.

Among non-structural components, staircase damage is the only contributor to the SiP recovery state for the locations and intensity levels provided in Figure 7.9. It hinders achieving the SiP recovery state in 11% of the realizations in the scenario-based assessment performed in Delta.

The most critical non-structural components which hinder reoccupancy are wall partitions and finishes as they hinder achieving this recovery state in almost all of the realizations. Other critical non-structural components are the mechanical equipment, hot and cold water piping, and HVAC ducts as seen in Figure 7.9 which also hinder reoccupancy in most of the realizations.

Damages to the staircases and fire sprinkler system also hinder achieving reoccupancy in most of the realizations. This is more critical in the scenario-based assessment in Delta and the intensity-based assessment using 2475-year motions. Elevator and Electrical equipment damages hinder functional recovery in more than 50% of the realizations for the locations and intensity levels provided in Figure 7.9. By contrast, the contribution of curtain walls and suspended ceiling damage is not significant except that curtain walls can hinder the functional recovery state in 49% of realizations in the intensity-based assessment under the 2475-year motions.

Note that while the economic losses associated with wall partitions and mechanical equipment are considerable (see Figure 6.8), the economic loss associated with hot and cold water piping and HVAC ducts is not significant in all hazard levels and locations. It can be concluded that although hot and cold water piping and HVAC ducts are not critical components in terms of their contribution to economic loss, they are important in terms of hindering the building functionality immediately after the earthquake.

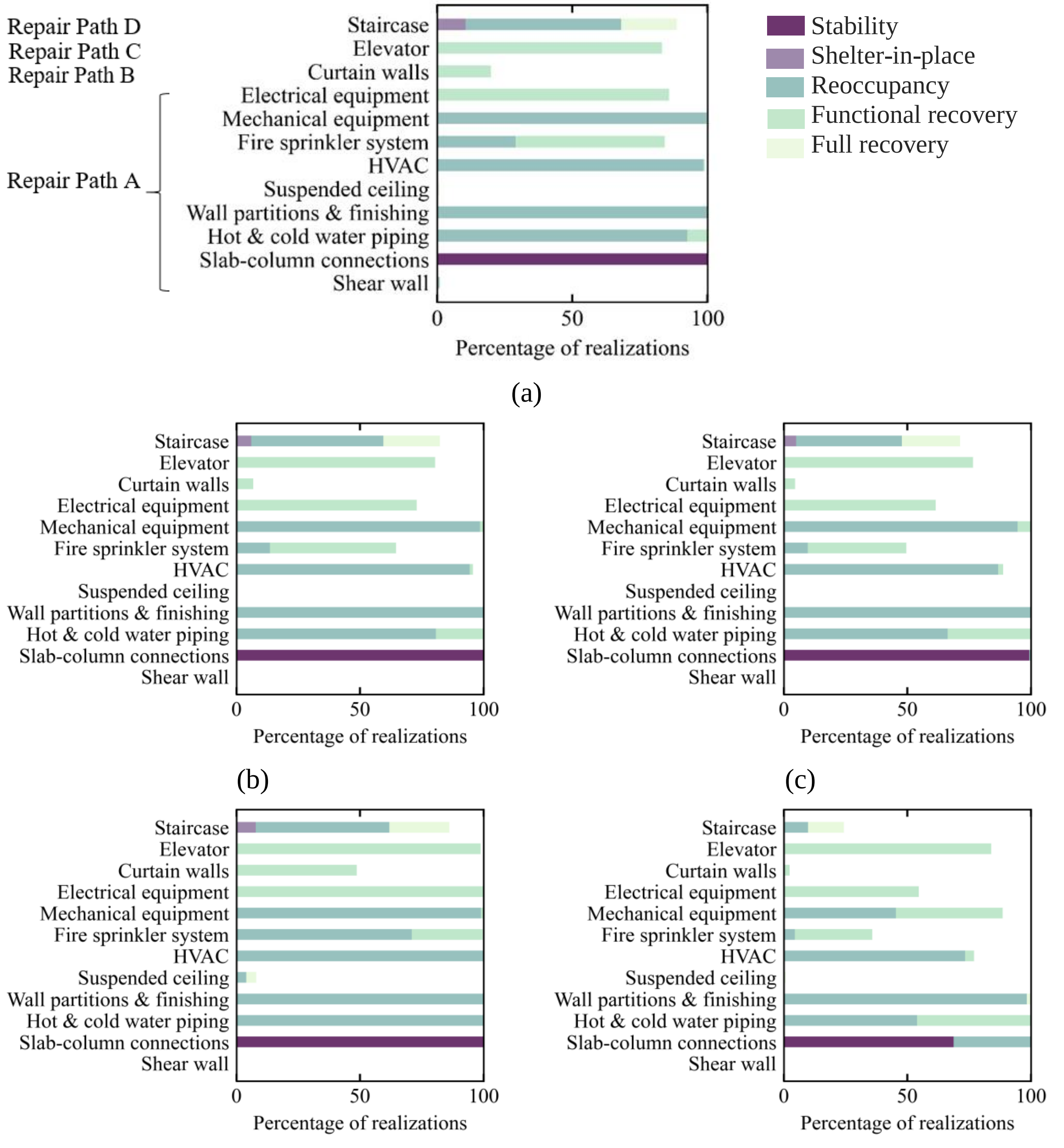

Figure 7.9. Percentage of repairable realizations in which a component incurs damage that hinders either of recovery states for the scenario-based assessments in (a) Delta; (b) Richmond; (c) Burnaby; and for the intensity-based assessments with (d) 2475-year; and (e) 475-year hazard levels.

The deaggregation of repairable downtime to functional recovery is shown in Figure 7.10 and is developed by determining the average contribution of each repair path across all realizations for

Delta, Richmond, and Burnaby in the scenario-based assessment and for the 2475-, 975-, and 475-year hazard levels in the intensity-based assessment. Note that the inspection time and the impeding factors delays, other than contractor mobilization, are the same for all repair paths. Also, the repair time is the same within each repair path. The repair time is categorized as structural and non-structural repair time. Since all structural components repair is done in repair path A, the structural components repair time is zero in other repair paths. Based on the results in Figure 7.10, in sites with a deep basin (e.g. Delta) and under high intensity levels (e.g. 2475-year motions), repair path A governs the downtime, while repair paths C and D govern in shallow basins and under lower intensity levels (e.g. 475-year motions). Figure 7.10 shows that the downtime associated with repair paths C and D is mostly caused by the impeding factors, not the components repair time. The contractor mobilization delay is considerably higher in repair path C (elevators repair) than other repair paths and governs the downtime to the functional recovery state for 475-year motions despite the short time required to repair the elevators (Figure 7.10e). This is another indication that the relationship between seismic damage and downtime not being one-to-one. As inferred by the results in Figure 7.10, strengthening a component will reduce downtime only if that component belongs to the governing repair path (Molina Hutt et al., 2022) and the impeding factor delay corresponding to the repair of that component is not significant. Previous studies also showed that contractor mobilization impeding delays governs the downtime under a 475-year event (e.g. Molina Hutt et al., 2021; Tipler, 2014). The lowest contractor delay time among all repair paths is associated with the staircase repair, i.e., repair path D. Figure 7.10 also shows financing delays are significantly lower in 475-year motions compared to higher intensities or at deep basin sites. This is because the financing delay is determined as a function of the economic loss ratio and thus, the downtime associated with financing delays is lower in locations or intensities with lower earthquake-induced loss.

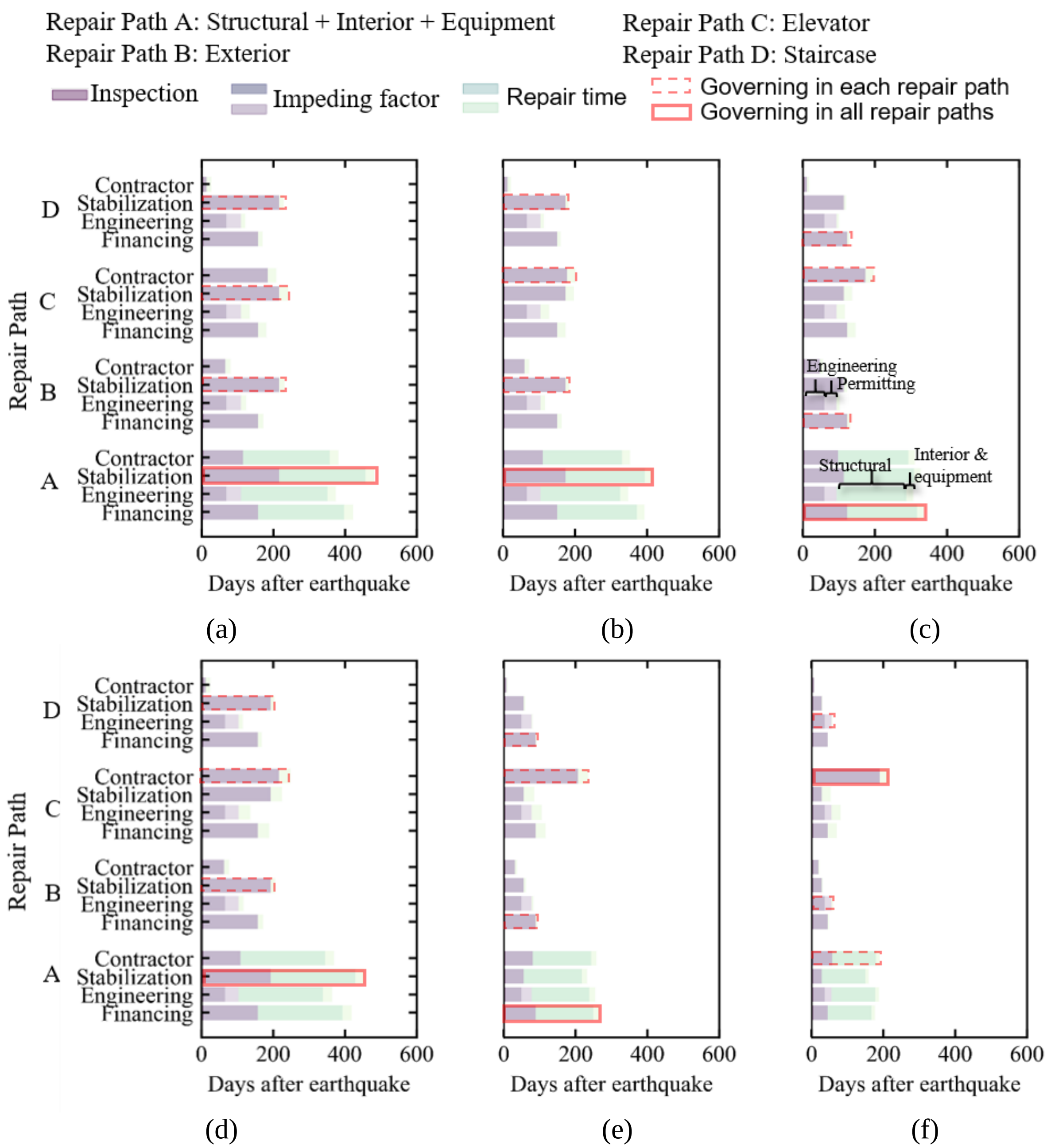

Figure 7.10. Deaggregation of mean downtime to functional recovery for repairable realizations for the scenario-based assessments in (a) Delta; (b) Richmond; (c) Burnaby; and for the intensity-based assessments with (d) 2475-year; (e) 975-year and (f) 475-year hazard levels.

7.5 Summary and Recommendations

The downtime estimation tool developed by Molina Hutt et al. (2022) is utilized to evaluate the downtime of the 30-story residential RCSW building archetypes for a range of intensity levels and basin depths across Metro Vancouver under simulated M9 motions. Three recovery states are considered in the assessment which are Functional Recovery (FR), Reoccupancy (RO), and Shelter-in-Place (SiP). The most significant findings are summarized below:

- The median functional recovery time for the scenario-based assessments varies between 175 and 543 days for West Vancouver (located outside the basin) and Delta with highest basin depth, respectively.

- The median functional recovery time for the intensity-based assessments varies between 164 days (for 100-year motions) and 491 days (for 2475-year motions).

- When subjected to an M9 CSZ earthquake scenario, the functional recovery time of the buildings located in all locations across Metro Vancouver except West Vancouver exceed that of a “functional level earthquake” (i.e., a 475-year ground motion) primarily due to basin amplification effects.

- The median functional recovery time of the buildings designed per current provisions in Metro Vancouver (i.e., for the 2475-year hazard level) is 491 days which is greater than 50% of the median building replacement time (i.e., 907 days) and therefore, future considerations are necessary.

- Building recovery trajectories highlight huge uncertainty in downtime estimates. Detailed recovery trajectory plots show that repair path A (structural, interior, and equipment repairs) governs downtime for locations with deep basins and under high shaking intensities while repair paths C (staircase repairs) and D (elevator repairs) are the governing repair path in shallow basins and under lower shaking intensities.

- 69% of the 475-year realizations hindered achieving the shelter-in-place recovery state after the earthquake and thus, the building archetypes does not meet the robustness performance criteria proposed by Molina Hutt et al. (2022).

- 100% of the 475-year realizations have functional recovery times greater than 4 months; therefore, the building archetypes does not meet the rapidity performance criteria proposed by Molina Hutt et al. (2022).

- Downtime deaggregation shows that the contribution from building collapse and irreparable damage to functional recovery time is considerably less than repairable damage contribution.

- Among the structural components, slab-column connections contribute the most to downtime of the building archetypes. Critical non-structural components are wall partitions and finishes, mechanical equipment, hot and cold water piping, and HVAC ducts.

Chapter 8: Conclusions

8.1 Summary of Findings

As part of this thesis, nonlinear structural analysis models of tall residential RCSW archetype buildings, representative of modern construction practice in Canada, are generated. These models are employed to perform nonlinear time-history analyses as part of a series of intensity-based seismic performance assessments using ground motions with return periods of 2475, 975, 475, and 100 years (referred to as 2015 NSHM motions). In addition, nonlinear time-history analyses is performed as part of scenario-based assessments using simulated ground motions of M9 CSZ earthquakes at eight locations across Metro Vancouver. The simulated ground motions account for the effects of the Georgia sedimentary basin, which can amplify ground motion shaking, particularly at long periods. The nonlinear analysis results are used to estimate the economic loss and downtime to different recovery states of the building archetypes. The following sections provide a summary of observations under the following key categories: nonlinear analysis results (Section 8.1.1), loss assessment results (Section 8.1.2), and downtime assessment results (Section 8.1.3).

8.1.1 Summary of Nonlinear Analysis Results

The building archetypes are designed for the same site class in eight locations across Metro Vancouver (Delta, Richmond, Burnaby, New Westminster, Surrey, Vancouver, North Vancouver, and West Vancouver) and subjected to the same ground motions in the intensity-based assessments. Under such conditions, the resultant structural responses are the same for the eight locations considered in this study. By contrast, high variations in structural responses are observed in the scenario-based assessments. Structural response parameters in the scenario-based assessments are higher at sites where the Georgia sedimentary basin is deeper (i.e., higher $Z_{2.5}$ values), which results in higher basin amplification. The highest structural demands are observed at Delta with a $Z_{2.5}$ value of 3.27 km, and the lowest structural demands are observed at West Vancouver with a $Z_{2.5}$ value of 0.67 km. For example, the maximum transient drift ratio in Delta, the deepest basin site, is more than five times the maximum transient drift ratio in West Vancouver, which is located immediately outside the basin. This sharp variation in seismic demands is not captured in the 2015 NSHM (Adams et al., 2015), which does not explicitly consider deep sedimentary basin effects. Consistent with past studies (Eksir Monfared et al., 2021), the structural responses of the scenario-based assessments at deep basins are higher than those associated with the 2475-year ground motions, the hazard level employed by NBC 2015 (NRC, 2015) for modern building design.

Aligned with the intent of NBC 2015, the collapse probability is zero under any of the hazard levels considered in the intensity-based assessments. However, in the scenario-based assessments, collapse probabilities of 16.7%, 6.7%, and 3.3% are observed in Delta, Richmond, and Burnaby, respectively which demonstrates that life safety is not necessarily achieved when basin effects are considered.

8.1.2 Summary of Loss Assessment Results

The loss assessment results demonstrate a one-to-one relationship between the structural demands and earthquake-induced economic losses. For scenario-based assessments, the mean loss ratios vary from 1.4% in West Vancouver which is located outside the basin to 32% in Delta, the deepest basin site. For the intensity-based assessments, the mean loss ratios vary from 0.7% for 100-year motions to 14% for 2475-year motions. Due to basin effects, the mean loss ratios associated with scenario-based assessments in Delta, Richmond, and Burnaby exceed those of the 2475-year motions. The mean loss ratio associated with 475-year motions is 4.4%, which is lower than that of the scenario-based assessments in all locations except West Vancouver despite the fact that the return period of the M9 CSZ earthquake scenarios is 500 years (Atwater & Hemphill-Haley, 1997) which is close to that of the 475-year motions.

Loss deaggregation results indicate that collapse has a considerable contribution to the total loss of building archetypes in the scenario-based assessments in Delta, Richmond, and Burnaby where 52.2%, 35.9%, and 24.1% of the estimated mean loss ratio is associated with collapse. In the scenario-based assessments, irreparable damage has a negligible contribution (less than 3%) to the mean loss in all locations except Delta, Richmond, and Burnaby with 16.3%, 5.9%, and 8.4% irreparable damage contribution. In the intensity-based assessments, irreparable damage contribution is only considerable for the 2475-year intensity level with a 10.7% contribution to the mean loss ratio. For the scenario-based assessments, other than in Delta and West Vancouver, structural damage is the main loss driver in all locations with contributions ranging from 43% (in Richmond) to 70% (in Surrey) of the mean loss ratio. Similarly, structural damage is the main contributor to mean loss ratio in the intensity-based assessments with moderate (475-year and 975-year) to high (2475-year) hazard levels with an average contribution of 65%. In shallow basins and for low hazard levels, non-structural damage is the main contributor to economic loss with 64.8% and 71.8% contributions for the scenario-based assessment in West Vancouver and under the 100-year motions, respectively.

Among structural components, slab-column connections are the main contributor to the mean loss ratio of repairable realizations with contributions ranging from 37% (in West Vancouver) to 75% (in Delta) for the scenario-based assessments and 29% (for 100-year motions) to 73% (for 2475-year motions) in the intensity-based assessments. Among non-structural components, wall partitions contribute the most to the mean loss ratio with contributions ranging from 14% (in Delta) to 49% (in West Vancouver) for the scenario-based assessments and 14% (for 2475-year motions) to 38% (for 100-year motions) in the intensity-based assessments. Therefore, strengthening the wall partitions and slab-column connections or developing strategies to minimize the seismic drift demands (which causes damage to these components) can reduce the earthquake-induced economic losses.

8.1.3 Summary of Downtime Assessment Results

The median functional recovery time for scenario-based assessments varies from 175 days in West Vancouver which is located outside the basin to 543 days in Delta, the deepest basin site. The median functional recovery time for the intensity-based assessments ranges from 164 days to 491 days for the 100- and 2475-year hazard levels, respectively. Due to basin amplifications, when subjected to M9 CSZ earthquake scenarios, the functional recovery time of the buildings located in all locations across Metro Vancouver except for West Vancouver (which is located outside the basin) exceed that of a "functional level earthquake" (i.e., a 475-year ground motion). The median functional recovery time of the buildings designed per current provisions in Metro Vancouver (i.e., for the 2475-year return period) is 491 days which is greater than 50% of the median building replacement time (i.e., 907 days) which may warrant future considerations in design codes and guidelines.

The robustness performance criteria proposed by Molina Hutt et al. (2022) is not met as the shelter-in-place recovery state is hindered in 69% of the 475-year realizations. Similarly, the rapidity performance criteria proposed by Molina Hutt et al. (2022) is not satisfied as the functional recovery time of all 475-year realizations is greater than 4 months.

Downtime deaggregation results demonstrate that most of the FR downtime (i.e., 63 to 100%) is associated with repairable realizations. Collapse contribution is zero for all hazard levels in the intensity-based assessment and for all locations in the scenario-based assessment except Delta, Richmond, and Burnaby with 28%, 14.4%, and 10% contribution in total downtime. The irreparable contribution varies from 0 to 8.7% among all locations and intensity levels.

The deaggregation of repairable components demonstrate that the main contributor to downtime of the building archetypes is the damage to the slab-column connections and therefore, strengthening the slab-column connections is a good strategy to reduce the downtime to achieve any of the recovery states. Among non-structural components, wall partitions and finishing, mechanical equipment, hot and cold water piping, and HVAC ducts contribute the most to downtime.

In sites with deep basins and for high hazard levels, repair path A (structural, interior, and equipment repair) governs the functional recovery downtime mostly due to the high repair time of the slab-column connections. However, for low hazard levels and shallow basins, repair path C (elevator repair) governs the functional recovery downtime mostly due to the high contractor mobilization delays required for elevator repairs.

8.2 Future Studies

The presented thesis provides comprehensive estimations of the structural responses, economic loss and downtime of modern residential tall RCSW buildings in Metro Vancouver under different earthquake scenarios and earthquake ground motion shaking intensities. Some of the simplifying assumptions and limitations associated with this study which warrant further research are listed below.

- Nonlinear modeling and time-history analysis of the archetype buildings are performed only in the cantilevered direction and the resultant engineering demand parameters are used in both cantilevered and coupled directions for the purpose of loss and downtime assessment. Future studies can explicitly model and analyze the buildings in both directions and provide more accurate predictions of structural responses as well as loss and downtime.

- Due to the limitations of the 2D model, the gravity system is modeled as a single column with high axial stiffness and low bending stiffness to account for the P-Delta effects (see Chapter 3). Therefore, the contribution of the gravity system to the seismic response of the structure is not fully captured and any possible nonlinear response of the gravity system is not considered. Future studies can address this limitation.

- The interaction of the basement levels retaining walls with the surrounding soil is not considered in the finite element model, and fixed connections are used at the base of the core and retaining walls. Soil structure interaction can be included in future research to better capture the effects of soil response on the response of the structure.

- The basement diaphragms and retaining walls are modeled using linear elastic springs and Timoshenko beam elements, respectively. Future studies can improve the basement model and provide more accurate estimates of structural response.

- The main focus of this study is on estimating the functional recovery downtime of tall residential RCSW buildings across Metro Vancouver due to their predominance. Only one seismic force resisting system, building plan, and occupancy type is considered in this study. Future research can include more variations of tall buildings for functional recovery time assessment. Also, in addition to tall buildings, functional recovery downtime of mid- and low-rise buildings can be the focus of future studies. In particular, a regional assessment in terms of functional recovery downtime can provide useful information for policy makers and insurance companies.

- Median values of FEMA P-58 (FEMA, 2018) fragility functions for slender shear walls fragility group (fragility id “B1044.101”) are considerably higher than the damageable wall drift ratios obtained from structural analysis and therefore, most of the RCSWs have negligible damage. The author believes FEMA P-58 fragility functions for slender shear walls should be based on the stress-strain of concrete or steel materials as opposed to effective drift to better capture the damage to RCSWs by leveraging results from nonlinear dynamic analysis. Further studies are required to improve FEMA P-58 fragility functions for slender shear walls.

References

42 U.S.C. § 7705(b). (2018). *“Seismic Standards.”* United States Code.

Abrahamson, N., Gregor, N., & Addo, K. (2016). BC hydro ground motion prediction equations for subduction earthquakes. *Earthquake Spectra*, *32*(1), 23–44. https://doi.org/10.1193/051712EQS188MR

ACI 318. (2014). *Building code requirements for structural concrete and commentary*. American Concrete Institute, Detroit, MI.

Adams, J., Halchuk, S., Allen, T., & Rogers, G. (2015). Canada’s 5th Generation Seismic Hazard Model, As Prepared For the 2015 National Building Code of Canada. *The 11th Canadian Conference on Earthquake Engineering*, 21–24.

Ahdi, S. K., Ancheta, T. D., Contreras, V., Kishida, T., Kwak, D. Y., Kwok, A. O., Parker, G. A., Bozorgnia, Y., & Stewart, J. P. (2017). Nga-Subduction Site Database. *16th World Conference on Earthquake Engineering*.

Almufti, I, Molina Hutt, C., Mieler, M., Paul, N. A., & Fusco, C. R. (2018). *The HayWired Earthquake Scenario - Engineering Implications: Case Studies of Tall-Building Structural Analyses and Downtime and Loss Assessment for the HayWired Scenario Mainshock*. United States Geological Survey Scientific Investigations Report 2017-5013-I-Q, Menlo Park, CA.

Almufti, Ibrahim, & Willford, M. (2013). The resilience-based earthquake design initiative (REDi™) rating system. *Arup Co.*

Ancheta, T. D., Darragh, R. B., Stewart, J. P., Seyhan, E., Silva, W. J., Chiou, B. S. J., Wooddell, K. E., Graves, R. W., Kottke, A. R., Boore, D. M., Kishida, T., & Donahue, J. L. (2014). NGA-West2 database. *Earthquake Spectra*, *30*(3), 989–1005.

https://doi.org/10.1193/070913EQS197M

Aoi, S., Kunugi, T., & Fujiwara, H. (2004). Strong-motion seismograph network operated by NIED: K-NET and KiK-net. *Journal of Japan Association for Earthquake Engineering*, *4*(3), 65–74. https://doi.org/10.5610/jaee.4.3_65

Arima, E. Y., St. Claire, E., Clamhouse, L., Edgar, J., Jones, C., & Thomas, J. (1991). *Between Ports Alberni and Renfrew : Notes on West Coast Peoples*. University of Ottawa Press.

ASCE. Minimum Design Loads for Buildings and Other Structures, ASCE/SEI 7-16. (2016). Reston, VA: American Society of Civil Engineers.

Aswegan, K. P. (2013). *Rational Procedure for Damage Based Serviceability Design of Steel Buildings Under Wind Loads and a Simple Linear Response History Procedure for Building Codes*. (Doctoral dissertation, Virginia Tech).

ATC-40. (1996). *Methodology for Evaluation and Upgrade of Reinforced Concrete Buildings*.

ATC-72-1. (2010). *Modeling and acceptance criteria for seismic design and analysis of tall buildings*. Redwood City, CA.

ATC. (2006). *ATC-40*. https://doi.org/10.1061/40889(201)5

ATC. (2018). *San Francisco tall buildings study*. Redwood City, CA.

Atwater, B F, & Hemphill-Haley, E. (1997). *Recurrence Intervals for Great Earthquakes of the Past 3,500 Years at Northeastern Willapa Bay, Washington*. United States Geological Survey, Reston, VA.

Atwater, Brian F., Nelson, A. R., Clague, J. J., Carver, G. A., Yamaguchi, D. K., Bobrowsky, P. T., Bourgeois, J., Darienzo, M. E., Grant, W. C., Hemphill-Haley, E., Kelsey, H. M., Jacoby, G. C., Nishenko, S. P., Palmer, S. P., Peterson, C. D., & Reinhart, M. A. (1995). Summary of Coastal Geologic Evidence for past Great Earthquakes at the Cascadia Subduction Zone.

Earthquake Spectra, *11*(1), 1–18. https://doi.org/10.1193/1.1585800

Bebamzadeh, A., Ventura, C. E., & Fairhurst, M. (2015). *S2GM: Ground motion selection and scaling database*. Annual Los Angeles Tall Buildings Design Council Meeting, Los Angeles, CA.

Bilau, A., Witt, E., & Lill, I. (2015). A Framework for Managing Post-disaster Housing Reconstruction. *Procedia Economics and Finance*, *21*(15), 313–320.

Birely, A. C. (2012). *Seismic Performance of Slender Reinforced Concrete Structural Walls*. Ph.D. dissertation, Dept. of Civil and Environmental Engineering, University of Washington, Seattle, WA.

Bohl, A., & Adebar, P. (2011). Plastic hinge lengths in high-rise concrete shear walls. *Structural Journal*, *108*(2), 148–157.

Bruneau, M., Chang, S. E., Eguchi, R. T., Lee, G. C., O'Rourke, T. D., Reinhorn, A. M., Shinozuka, M., Tierney, K., Wallace, W. A., & Von Winterfeldt, D. (2003). A Framework to Quantitatively Assess and Enhance the Seismic Resilience of Communities. *Earthquake Spectra*, *19*(4), 733–752.

Building Seismic Safety Council. (1997). *NEHRP Guidelines for the Seismic Rehabilitation of Buildings, FEMA-273*. Federal Emergency Management Agency: Washington, DC.

Campbell, K. W., & Bozorgnia, Y. (2014). NGA-West2 ground motion model for the average horizontal components of PGA, PGV, and 5% damped linear acceleration response spectra. *Earthquake Spectra*, *30*(3), 1087–1114. https://doi.org/10.1193/062913EQS175M

Canadian Commission on Building and Fire Codes. (2017). *User's Guide – NBC 2015: Part 4 Division B Structural Commentaries*. Ottawa, Canada.

Charney, F. A. (1990). Wind drift serviceability limit state design of multistory buildings. *Journal* *of Wind Engineering and Industrial Aerodynamics*, *36*, 203–212.

Choi, Y., Stewart, J. P., & Graves, R. W. (2005). Empirical model for basin effects accounts for basin depth and source location. In *Bulletin of the Seismological Society of America* (Vol. 95, Issue 4, pp. 1412–1427). https://doi.org/10.1785/0120040208

City of Vancouver. (2021). *Understanding Earthquakes*. https://vancouver.ca/home-property-development/understanding-earthquakes.aspx

Comerio, M. C. (2006). Estimating downtime in loss modeling. *Earthquake Spectra*, *22*(2), 349–365.

Cornell, A., & Krawinkler, H. (2000). *Progress and Challenges in Seismic Performance Assessment*. https://apps.peer.berkeley.edu/news/2000spring/performance.html

Correia, A. A., Almeida, J. P., & Pinho, R. (2008). Force-Based Versus Displacement-Based Formulations In The Cyclic Nonlinear Analysis of RC Frames. *14th World Conference on Earthquake Engineering, Beijing*.

CSA (Canadian Standard Association). (2014). *Design of concrete structures*. CSA A23.3-14. Toronto, ON: CSA.

Dash, R. K., Spence, G. D., Riedel, M., Hyndman, R. D., & Brocher, T. M. (2007). Upper-crustal structure beneath the strait of Georgia, Southwest British Columbia. *Geophysical Journal International*, *170*(2), 800–812.

Day, S. M., Graves, R., Bielak, J., Dreger, D., Larsen, S., Olsen, K. B., Pitarka, A., & Ramirez-Guzman, L. (2008). Model for basin effects on long-period response spectra in southern California. *Earthquake Spectra*, *24*(1), 257–277. https://doi.org/10.1193/1.2857545

Dilger, W., & Cao, H. (1991). Behaviour of Slab-Column Connections under Reversed Cyclic Loading. *2nd Int. Conf. High-Rise Build*.

Dilger, W. H., & Brown, S. J. (1995). Earthquake resistance of slab-column connections. *Festschrift Prof. Dr. Hugo Bachmann Zum*, *60*, 22–27.

Earthquake Engineering Research Institute. (2019). *Functional Recovery: A Conceptual Framework with Policy Options*.

Earthquakes Canada. (2021). *Earthquakes Canada, GSC, Earthquake Search (On-line Bulletin)*. https://earthquakescanada.nrcan.gc.ca/zones/westcan-en.php

Eksir Monfared, A. (2020). *Georgia sedimentary basin effects on the response of modern tall RC shear wall buildings to M9 Cascadia subduction zone earthquakes*. University of British Columbia.

Eksir Monfared, A., Molina Hutt, C., Kakoty, P., Kourehpaz, P., & Centeno, J. (2021). Effects of the Georgia Sedimentary Basin on the Response of Modern Tall RC Shear-Wall Buildings to M9 Cascadia Subduction Zone Earthquakes. *Journal of Structural Engineering*, *147*(8), 05021003. https://doi.org/10.1061/(asce)st.1943-541x.0003067

Emporis. (2020). *The Global Provider of Building Data*. https://www.emporis.com/

England, T. D. J., & Bustin, R. M. (1998). Architecture of the Georgia Basin, southwestern British Columbia. *Bulletin of Canadian Petroleum Geology*, *46*(2), 288–320.

Environmental Reporting BC. (2018). *Trends in B.C.'s Population Size & Distribution*. https://www.env.gov.bc.ca/soe/indicators/sustainability/bc-population.html

ETABS Software. (2016). Version 16, Computer and structures, Inc. Berkeley, California, USA.

FEMA. (2018). *Seismic performance assessment of buildings FEMA P-58*. Federal Emergency Management Agency, Washington, DC.

FEMA. (2020). *NEHRP recommended seismic provisions for new buildings and other structures FEMA P-2082*. Federal Emergency Management Agency, Washington, DC.

FEMA P-2055. (2019). *Post-disaster Building Safety Evaluation Guidance FEMA P-2055*. Federal Emergency Management Agency. Washington, DC.

Filippou, F. C., Popov, E. P., & Bertero, V. V. (1983). *Effects of Bond Deterioration on Hysteretic Behaviour of Reinforced Concrete Joints*. Report EERC 83-19, Earthquake Engineering Research Center, University of California, Berkeley.

Frankel, A. (2017). Modeling strong-motion recordings of the 2010 Mw 8.8 Maule, Chile, earthquake with high stress-drop subevents and background slip. *Bulletin of the Seismological Society of America*, *107*(1), 372–386. https://doi.org/10.1785/0120160127

Frankel, A., Wirth, E., Marafi, N., Vidale, J., & Stephenson, W. (2018). Broadband synthetic seismograms for magnitude 9 earthquakes on the cascadia megathrust based on 3D simulations and stochastic synthetics, Part 1: Methodology and overall results. *Bulletin of the Seismological Society of America*, *108*(5), 2347–2369. https://doi.org/https://doi.org/10.1785/0120180034

Geschwindner, L. F. (2002). A practical look at frame analysis, stability and leaning columns. *Engineering Journal*, *39*(4), 167–181.

Goretti, A., Molina Hutt, C., & Hedelund, L. (2017). Post-earthquake safety evaluation of buildings in Portoviejo, Manabí province, following the Mw7.8 Ecuador earthquake of April 16, 2016. *International Journal of Disaster Risk Reduction*, *24*(March), 271–283. https://doi.org/10.1016/j.ijdrr.2017.06.011

Hognestad, E. (1951). *E. A study of combined bending and axial load in reinforced concrete members.* University of Illinois at Urbana Champaign, College of Engineering. Engineering Experiment Station.

Ji, X., Liu, D., Sun, Y., & Molina Hutt, C. (2017). Measuring bias in structural response caused by ground motion scaling. *EARTHQUAKE ENGINEERING & STRUCTURAL DYNAMICS*, *46*(4), 517–535.

Kakoty, P., Dyaga, S. M., & Molina Hutt, C. (2020). Impacts of simulated M9 Cascadia Subduction Zone earthquakes considering amplifications due to the Georgia sedimentary basin on reinforced concrete shear wall buildings. *Earthquake Engineering and Structural Dynamics*, *50*(1), 237–256.

Kourehpaz, P., Molina Hutt, C., Marafi, N. A., Berman, J. W., & Eberhard, M. O. (2020). Estimating economic losses of midrise reinforced concrete shear wall buildings in sedimentary basins by combining empirical and simulated seismic hazard characterizations. *Earthquake Engineering and Structural Dynamics*, *50*(1), 26–42. https://doi.org/10.1002/eqe.3325

Lang, A., Mayes, R., Gumpertz, S., Wade, K., Baker, H., & Group, R. (2018). FORWARD : Second Generation B2B / BORP and Resilient Planning for Existing Buildings. *2018 SEAOC Conference Proceedings, Palm Springs, CA, September*, 1–17.

Marafi, N. A., Makdisi, A. J., Eberhard, M. O., & Berman, J. W. (2020). Impacts of an M9 Cascadia Subduction Zone Earthquake and Seattle Basin on Performance of RC Core Wall Buildings. *Journal of Structural Engineering*, *146*(2), 04019201.

Marafi, Nasser A., Ahmed, K. A., Lehman, D. E., & Lowes, L. N. (2019b). Variability in Seismic Collapse Probabilities of Solid- and Coupled-Wall Buildings. *Journal of Structural Engineering*, *145*(6), 04019047. https://doi.org/10.1061/(asce)st.1943-541x.0002311

Marafi, Nasser A., Eberhard, M. O., Berman, J. W., Wirth, E. A., & Frankel, A. D. (2017). Effects of deep basins on structural collapse during large subduction earthquakes. *Earthquake Spectra*, *33*(3), 963–997.

Marafi, Nasser A., Eberhard, M. O., Berman, J. W., Wirth, E. A., & Frankel, A. D. (2019a). Impacts of simulated M9 cascadia subduction zone motions on idealized systems. *Earthquake Spectra*, *35*(3), 1261–1287. https://doi.org/10.1193/052418EQS123M

Marquis, F. (2015). *A framework fot understanding post-earthquake decisions on multi-storey concrete buildings in Christchurch, New Zealand*. Masters thesis, University of British Columbia, Canada.

Massicotte, B., Elwi, A. E., & MacGregor, J. G. (1990). Tension-stiffening model for planar reinforced concrete members. *Journal of Structural Engineering*, *116*(11), 3039–3058.

McKenna, F. (2011). OpenSees: A framework for earthquake engineering simulation. *Computing in Science and Engineering*, *13*(4), 58–66. https://doi.org/10.1109/MCSE.2011.66

Megally, S., & Ghali, A. (2000). Punching shear design of earthquake-resistant slab-column connections. *ACI Structural Journal*, *97*(5), 720–730. https://doi.org/10.14359/8807

Menegotto, M., & Pinto, P. E. (1973). *Method of analysis for cyclically loaded reinforced concrete plane frames including changes in geometry and non-elastic behavior of elements under combined normal force and bending*. IABSE symposium on resistance and ultimate deformability of structures acted on by well-defined repeated loads. Final report; 1973.

Moehle, J. (2015). *Seismic Design of Reinforced Concrete Buildings*. McGraw-Hill Education.

Moehle, J., & Deierlein, G. G. (2004). A FRAMEWORK METHODOLOGY FOR PERFORMANCE-BASED EARTHQUAKE ENGINEERING. *13th World Conference on Earthquake Engineering*.

Moehle, J. P., Hooper, J. D., Fields, D. C., & Gedhada, R. (2011). *Seismic Design of Cast-in-Place Concrete Special Structural Walls and Coupling Beams: A Guide for Practicing Engineers*. NEHRP Seismic Design Technical Brief No. 6.

Mohd Yassin, M. H. (1994). *Nonlinear analysis of prestressed concrete structures under monotonic and cyclic loads*. University of California, Berkeley.

Molina Hutt, C., Vahanvaty, T., & Kourehpaz, P. (2022). *An analytical framework to assess earthquake-induced downtime and model recovery of buildings*. https://doi.org/10.1177/87552930211060856

Molina Hutt, C., Almufti, I., Willford, M., & Deierlein, G. (2016). Seismic Loss and Downtime Assessment of Existing Tall Steel-Framed Buildings and Strategies for Increased Resilience. *Journal of Structural Engineering*, *142*(8), C4015005. https://doi.org/10.1061/(asce)st.1943-541x.0001314

Molina Hutt, C., Hulsey, A. M., Kakoty, P., Deierlein, G. G., Eksir Monfared, A., Wen-Yi, Y., & Hooper, J. D. (2021). Toward functional recovery performance in the seismic design of modern tall buildings. *Earthquake Spectra*. https://doi.org/10.1177/87552930211033620

Molina Hutt, C., Rossetto, T., & Deierlein, G. G. (2019). Comparative risk-based seismic assessment of 1970s vs modern tall steel moment frames. *Journal of Constructional Steel Research*, *159*, 598–610. https://doi.org/10.1016/j.jcsr.2019.05.012

Molnar, S., Cassidy, J. F., Olsen, K. B., Dosso, S. E., & He, J. (2014a). Earthquake ground motion and 3D Georgia basin amplification in Southwest British Columbia: Deep Juan de Fuca Plate scenario earthquakes. *Bulletin of the Seismological Society of America*, *104*(1), 301–320. https://doi.org/10.1785/0120110277

Molnar, S., Cassidy, J. F., Olsen, K. B., Dosso, S. E., & He, J. (2014b). Earthquake ground motion and 3D Georgia basin amplification in Southwest British Columbia: Shallow blind-thrust scenario earthquakes. *Bulletin of the Seismological Society of America, 104*(1), 321–335. https://doi.org/10.1785/0120130116

Monahan, P. A. (2005). Soil hazard map of Greater Victoria for assessing the earthquake hazard due to lateral ground shaking. *Monahan Petroleum Consulting.*

Morikawa, N., & Fujiwara, H. (2013). A new ground motion prediction equation for Japan applicable up to M9 mega-earthquake. In *Journal of Disaster Research* (Vol. 8, Issue 5, pp. 878–888). https://doi.org/10.20965/jdr.2013.p0878

NEHRP. (2003). *2003 Edition NEHRP RECOMMENDED PROVISIONS FOR SEISMIC REGULATIONS FOR NEW BUILDINGS AND OTHER STRUCTURES (FEMA 450)*. NEHRP Consultants joint venture for the National Institute of Building Science, Washington, DC.

NEHRP. (2015). *NEHRP Recommended Seismic Provisions for New Buildings and Other Structures. II: Part 3*.

NIST. (2017a). *Guidelines for Nonlinear Structural Analysis for Design of Buildings, Part I–General*. NIST GCR 17-917-46v1; prepared by the Applied Technology Council for the National Institute of Standards and Technology; Gaithersburg; Maryland.

NIST. (2017b). *Recommended Modeling Parameters and Acceptance Criteria for Nonlinear Analysis in Support of Seismic Evaluation, Retrofit, and Design*. NIST GCR 17-917-45, prepared by the Applied Technology Council for the National Institute of Standards and Technology, Gaithersburg, Maryland.

NRC. (2015). *National Building Code of Canada: 2015*. National Research Council of Canada. https://doi.org/10.4224/40002005

OpenSeesWiki. (2016). *Analysis Commands*. https://doi.org/https://opensees.berkeley.edu/wiki/index.php/Analysis_Commands

Oyen, P. E. (2006). *Evaluation of Analytical Tools for Determining the Seismic Response of*

Reinforced Concrete Shear Walls. MS thesis, Dept. of Civil and Environmental Engineering, University of Washington, Seattle, WA.

Paul, N., Lee, J. S., Mieler, M., & Almufti, I. (2018). Improving Estimates of Earthquake-Induced Downtime in Individual Buildings Using the REDi Methodology. In *Structures Conference 2018* (pp. 447–456).

Petersen, M.D., Moschetti, M. P., Powers, P. M., Mueller, C. S., Haller, K. M., Frankel, A. D., Zeng, Y., Rezaeian, S., Harmsen, S. C., Boyd, O. S., Field, N., Chen, R., Rukstales, K. S., Luco, N., Wheeler, R. L., Williams, R. A., & Olsen, A. H. (2014). *Documentation for the 2014 Update of the United States National Seismic Hazard Maps.pdf*. Reston, VA: U.S. Geological Survey.

Petersen, Mark D, Shumway, A. M., Powers, P. M., Mueller, C. S., Moschetti, M. P., Frankel, A. D., Rezaeian, S., Mcnamara, D. E., Luco, N., Jaiswal, K. S., Thompson, E. M., Field, E. H., & Zeng, Y. (2020). *The 2018 update of the US National Seismic Hazard Model : Overview of model and implications*. https://doi.org/10.1177/8755293019878199

Petrini, L., Maggi, C., Priestley, M. J. N., & Calvi, G. M. (2008). Experimental verification of viscous damping modeling for inelastic time history analyzes. *Journal of Earthquake Engineering*, *12*(S1), 125–145. https://doi.org/10.1080/13632460801925822

Poland, C. (2009). *Defining Resilience: What San Francisco needs from its seismic mitigation policies*. Report, San Francisco Planning + Urban Research association.

Pugh, J. S. (2012). *Numerical Simulation of Walls and Seismic Design Recommendations for Walled Buildings*. University of Washington.

Pugh, J. S., Lowes, L. N., & Lehman, D. E. (2015). Nonlinear line-element modeling of flexural reinforced concrete walls. *Engineering Structures*, *104*, 174–192.

https://doi.org/10.1016/j.engstruct.2015.08.037

Ramirez, C. M., Liel, A. B., Mitrani-Reiser, J., Haselton, C. B., Spear, A. D., Steiner, J., Deierlein, G. G., & Miranda, E. (2012). Expected earthquake damage and repair costs in reinforced concrete frame buildings. *Earthquake Engineering & Structural Dynamics*, *41*(11), 1455–1475.

Rogers, G., Halchuk, S., Adams, J., & Allen, T. (2015). 5th Generation (2015) Seismic Hazard Model for Southwest British Columbia. *The 11th Canadian Conference on Earthquake Engineering*, 21–24.

RSMeans. (2020). *Building construction cost database*. RSMeans data from Gordian, Rockland, MA.

Ruiz-García, J., & Miranda, E. (2006). Residual displacement ratios for assessment of existing structures. *Earthquake Engineering & Structural Dynamics*, *35*(3), 315–336.

Saatcioglu, M., & Razvi, S. R. (1992). Strength and Ductility of Confined Concrete. *Journal of Structural Engineering*, *118*(6), 1590–1607.

Scott, M. H. (2011). Numerical integration options for force-based beam-column element in OpenSees. *Force-Based Element Integration Options in OpenSees*, 1–7.

Scott, M. H. (2019). *Non-Convergence Does Not Mean OpenSees Crashed*. https://portwooddigital.com/2019/10/23/non-convergence-does-not-mean-opensees-crashed/

Scott, M. H. (2020). *Handle Your Constraints with Care*. https://portwooddigital.com/2020/06/05/handle-your-constraints-with-care/

Senate Bill 1768. (2018). *"National Earthquake Hazards Reduction Program Reauthorization Act of 2018." 115th Congress*.

Slotboom, C. (2020). *Numerical Analysis of Self-centering Cross-laminated Timber Walls*. University of British Columbia.

SPUR. (2012). *Safe Enough to Stay*. Report, San Francisco Planning + Urban Research association.

Stephenson, W. J., Reitman, N. G., & Angster, S. J. (2017). *P- and S-wave velocity models incorporating the Cascadia subduction zone for 3D earthquake ground motion simulations—Update for Open-File Report 2007-1348*. https://doi.org/http://pubs.er.usgs.gov/publication/ofr20171152

Terzic, V., & Yoo, D. (2016). Repair Time Model for Buildings Considering the Earthquake Hazard. *SEAOC Convention Proceedings*, 562–571.

Thompson, M., Wirth, E. A., Frankel, A. D., Hartog, J. R., & Vidale, J. E. (2020). Basin amplification effects in the Puget Lowland, Washington, from strong-motion recordings and 3D simulations. *Bulletin of the Seismological Society of America*, *110*(2), 534–555. https://doi.org/10.1785/0120190211

Tipler, J. (2014). *Seismic Resilience of Tall Buildings—Benchmarking Performance and Quantifying Improvements.* Stanford, CA: Stanford University.

Tran, T. A., & Wallace, J. W. (2015). Cyclic Testing of Moderate-Aspect-Ratio Reinforced Concrete Structural Walls. *ACI Structural Journal*, *112*(6).

Vamvatsikos, D., & Allin Cornell, C. (2002). The incremental dynamic analysis and its application to performance-based earthquake engineering. *Proceedings of the 12th European Conference on Earthquake Engineering*, *40*.

Wagstaffe, J. (2016). *The 'Big One'near Vancouver you may not know about*. https://www.cbc.ca/news/canada/british-columbia/fault-lines-big-one-1.3795416

Wang, Y. (2020). *Earthquakes in and around Vancouver,CA*. https://storymaps.arcgis.com/stories/5b8c7650f85541c0870bedf3d8850650

Wirth, E. A., Chang, S. W., & Frankel, A. D. (2018). *2018 report on incorporating sedimentary basin response into the design of tall buildings in Seattle, Washington:* United States Geological Survey, Reston, VA.

Wirth, E. A., Frankel, A. D., & Vidale, J. E. (2017). Evaluating a kinematic method for generating broadband ground motions for great subduction zone earthquakes: Application to the 2003 Mw 8.3 Tokachi-Oki earthquake. *Bulletin of the Seismological Society of America*, *107*(4), 1737–1753. https://doi.org/10.1785/0120170065

Wirth, E. A., Vidale, J. E., Frankel, A. D., Pratt, T. L., Marafi, N. A., Thompson, M., & Stephenson, W. J. (2019). Source-Dependent Amplification of Earthquake Ground Motions in Deep Sedimentary Basins. In *Geophysical Research Letters* (Vol. 46, Issue 12). https://doi.org/10.1029/2019GL082474

Wong, P. S., Vecchio, F. J., & Trommels, H. (2013). VecTor2 & FormWorks User's Manual (2nd edn). *University of Toronto: Toronto, ON, Canada*, Available from: http://www.civ.utoronto.ca/vector/.

Yura, J. A. (1971). The Effective Length of Columns in Unbraced Frames. *Engineering Journal*, *8*(2), 37–42.

Zhong, K., Lin, T., Deierlein, G. G., Graves, R. W., Silva, F., & Luco, N. (2021). Tall building performance-based seismic design using SCEC broadband platform site-specific ground motion simulations. *Earthquake Engineering and Structural Dynamics*, *50*(1), 81–98. https://doi.org/10.1002/eqe.3364

Zhu, M., McKenna, F., & Scott, M. H. (2018). OpenSeesPy: Python library for the OpenSees finite element framework. *SoftwareX*, *7*, 6–11. https://doi.org/10.1016/j.softx.2017.10.009

Zou, J., Welch, D. P., Zsarnoczay, A., Taflanidis, A., & Deierlein, G. G. (2020). Surrogate Modeling for the Seismic Response Estimation of Residential Wood Frame Structures. *Proceedings of the 17th World Conference on Earthquake Engineering, Japan.*

Zsarnoczay, A., & Kourehpaz, P. (2021). *NHERI-SimCenter/pelicun: pelicun v2.5* (2.5). Zenodo. https://doi.org/10.5281/zenodo.4408588